

Detection and Characterisation of Unknown Spacecraft Maneuvers

Shaziana Kaderali

Department of Mechanical Engineering

McGill University, Montreal, QC

March 2021



A thesis submitted to McGill University in partial fulfillment of the
requirements of the degree of

Master of Mechanical Engineering (Thesis)

© Shaziana Kaderali, 2021

ABSTRACT

Space Situational Awareness (SSA) is an important and pressing field, as the amount of space debris is growing due to the increase in spacecraft launches. Space agencies like NASA and ESA keep track of over 5,000 spacecraft and 20,000 spacecraft-related debris objects currently orbiting the Earth. These spacecraft may undergo trajectory changes through artificial impulsive maneuvers without warning, posing a risk to other spacecraft in the vicinity. Additionally, measurement data often consists of uncertainties, where usual spacecraft maneuver detection and characterisation methods are often computationally expensive. The goal of this work is to develop a quick, reliable, computationally inexpensive method for spacecraft maneuver detection and characterisation, which would be used to assist satellite operators in collision avoidance measures. This dissertation utilises such a technique, which is applied to simulated measurement data of an orbiting spacecraft taken from one ground site. With these objectives, a method using a modified Extended Kalman Filter (EKF) with covariance inflation from previous research was explored and simplified. Through building on this set of research, a new parameter definition is presented for maneuver detection and characterisation, named K , with focus on transverse apogee and perigee maneuvers. A relationship was then found between the detection parameter (both the original parameter, Ψ , and the new parameter, K) and the magnitude of the impulsive artificial maneuver. The detection and characterisation method was tested in several different scenarios, varying Δv magnitude and scale, Δv direction, maneuver orbital location, orbit geometry, noise covariance, detection parameter threshold, state covariance inflation threshold, and maneuver duration. In general, it was found that as the Δv magnitude increases, so does the magnitude of the detection parameter. This relationship was found to be nonlinear, of either a quadratic (Ψ) or logarithmic (K) relation through best fit curve testing. Possible future work includes: testing multi-maneuver scenarios, multi-sensor data collection and fusion, break-up or berthing events, rendezvous or mating events, and MATLAB EKF protocol implementation.

ABRÉGÉ

La connaissance de la situation spatiale est un domaine important et pressant, à cause de la quantité de débris spatiaux qui s'accumulent avec l'augmentation des lancements d'engins spatiaux. Les agences spatiales comme la NASA et l'ESA tracent de plus de 5000 satellites et 20000 débris liés aux satellites en orbite autour de la Terre. Ces satellites peuvent effectuer des changements de trajectoire par des manœuvres artificielles et impulsives sans avertissement, ce qui peut représenter un risque pour d'autres satellites à proximité. En plus, les données de mesure sont souvent constituées d'incertitudes, ce qui fait que les méthodes habituelles de détection et de caractérisation des manœuvres spatiales sont souvent coûteuses en calcul. Le but de ce travail est de développer une méthode rapide, fiable et peu coûteuse en calcul pour la détection et la caractérisation des manœuvres des satellites, qui serait utilisée pour aider les opérateurs de satellites dans les mesures d'évitement des collisions. Cette thèse utilise une technique, qui est appliquée à des données de mesure simulées d'un satellite artificiel en orbite, prises à partir d'un site au sol sur la Terre. Avec ces objectifs, une méthode utilisant un "Extended Kalman Filter (EKF)" modifié avec inflation de covariance à partir de recherches antérieures a été explorée et simplifiée. En s'appuyant sur cet ensemble de recherches, une nouvelle définition de paramètre est présentée pour la détection et la caractérisation des manœuvres, nommé K , avec comme but les manœuvres d'apogée et de périégée transversales. Une relation a ensuite été trouvée entre le paramètre de détection (le paramètre d'origine, du Ψ et le nouveau paramètre, K) et l'amplitude de la manœuvre artificielle et impulsive. La méthode de détection et de caractérisation a été examinée aux plusieurs scénarios différents, par variant de la magnitude et l'échelle de Δv , la direction de Δv , la position orbitale de la manœuvre, la géométrie de l'orbite, la covariance du bruit de la mesure, la valeur seuil du paramètre de détection, la valeur seuil de l'inflation de la covariance d'état et la durée de la manœuvre. En général, il a été constaté que lorsque l'amplitude de Δv augmente, l'amplitude du paramètre de détection augmente aussi. Cette relation s'est avérée non-linéaire, soit quadratique (Ψ) ou logarithmique (K), grâce à des techniques d'ajustement de courbe. Les travaux futurs possibles incluent: le test de scénarios multi-manœuvres, la collecte et la fusion de données multi-capteurs, les événements de rupture ou d'accostage, les événements de rendez-vous ou d'amarrage, et l'implémentation du protocole EKF en MATLAB.

ACKNOWLEDGEMENTS

First, I would like to give my greatest thanks to my Professor, Dr. Arun Misra, for his continuous support and encouragements throughout my degree program. Without Prof. Misra, completion of this thesis would not have been possible. Thank you for believing in me since day one, always giving me your time and patience, for all of your advising including career advice, and for supporting me in taking part in attending many conferences, including reaching my goal of attending the summer program at the International Space University. Thanks to Prof. John Hayes from Carleton University who was always willing to advise me in my undergraduate studies and urged me to take on this degree under Prof. Misra's supervision. Thank you to Dr. Alfred Ng, who was supportive, patient and flexible with my scheduling needs in marking for his course.

Thank you to Anne-Marie Pierre from the Mechanical Engineering department for her bubbly and encouraging personality. Thank you for always taking my calls and giving me the support and advice I needed to make sure I could smoothly accomplish the logistics necessary to complete my degree, especially when things got tougher during the pandemic.

Thank you to Isabelle Jean for all her support as well during the program. Thank you for being my lab neighbour who I could always talk to and share Frosty's ice cream with when needing a study break. Thank you as well for always being willing to advise and share stories of experience, and for assisting with French translations.

Thank you to other previous and current students of Prof. Misra and fellow labmates who also helped advise throughout studies, or were around to enjoy lunchtimes or late working evenings.

Thank you to several close friends and family. Thanks to my parents for not only the financial support, but also the continued encouragements to persevere when I needed it the most. Thank you to my sister for being there for me, the words of wisdom, and being a role model. Thank you to my best friends for being the shoulders to lean on whenever I needed, the endless encouragements and moral support, and the fun adventures when needing some relaxation. Thank you to all others in my network, near and far, for all and any encouragements, especially for supporting my space-related passions in all our interactions.

Thank you for the funding from the NSERC Discovery grant program for supporting this research.

TABLE OF CONTENTS

ABSTRACT	ii
ABRÉGÉ	iii
ACKNOWLEDGEMENTS	iv
LIST OF FIGURES	ix
LIST OF TABLES	x
NOMENCLATURE	xi
ACRONYMS	xiii
1 Introduction	1
1.1 Motivation and Background	1
1.1.1 The Space Environment and Debris Problem	1
1.1.2 Astrodynamics Standards for Space Debris	2
1.1.3 Space Situational Awareness (SSA) Definition	4
1.1.4 Observation-to-Object Tracking Association Demand	5
1.1.5 Event Definitions and Detection Needs	6
1.2 Event Detection Methods in Literature	7
1.2.1 Object Track Association and Event Detection	7
1.2.2 Single Event Detection and Characterisation	8
1.2.3 Other Event Detection Methods	10
1.2.4 Multi-Object Tracking and Event Detection	11
1.3 Thesis Objectives	14
1.4 Thesis Outline	14
2 Orbital Propagation	15
2.1 Orbital Mechanics and Orbital Propagator	15
2.1.1 Vectors, Reference Frames, and Frame Rotations	15
2.1.2 Spacecraft Dynamics Equations of Motion	18
2.1.3 Classical Orbital Elements (COEs)	19

2.2	Orbital Propagator Tests and Validation	23
3	Filtering and Detection	25
3.1	Filtering Methods	25
3.1.1	Kalman Filtering Overview	25
3.1.2	Extended Kalman Filter	26
3.2	Reference Frames and Observation Conversions	29
3.3	Detection Parameter Amendments, Improvements, and Preliminary Results	34
3.3.1	Detection Parameter Improvements	35
3.3.2	Preliminary Maneuver Detection Results	36
4	Maneuver Detection Results and Discussion	40
4.1	Simulation Setup	40
4.2	Detection Parameter Trends	41
4.2.1	Variation of K with Δv Magnitude and Direction	42
4.2.2	Variation of K with Orbital Location	51
4.2.3	Variation of K with Different Orbits	56
4.2.4	Variation of K with Measurement Noise Covariance, \mathbf{R}	59
4.2.5	Variation of K with Ψ Threshold and State Covariance Inflation Threshold, η	61
4.2.6	Variation of K with Maneuver Duration	64
4.2.7	Variation of K with Small-Scale Δv 's	66
5	Conclusions and Future Work	70
5.1	Conclusions and Final Key Points	70
5.2	Possibilities for Future Work	71
Appendix A Full Filtering Process Steps		73
Appendix B No Maneuver Base Result		75
Appendix C Qualitative Summaries		76
Appendix D Further Test Case Results		77
D.1	Variation in Measurement Noise Covariance	77
D.2	Variation in Ψ and η Thresholds	79
D.3	Variation in Maneuvering Duration	82

Appendix E Further Ψ Results	84
E.1 Variance in Orbital Location	84
E.2 Variation in Orbital Geometry and Orientation	88
E.3 Variation of Measurement Noise Covariance	91
E.4 Variance in Ψ and η Thresholds	93
E.5 Variance in Maneuver Duration	96
E.6 Small-Scale Δv 's	98
 Appendix F Maneuver Detection Time	 99
 REFERENCES	 106

LIST OF FIGURES

Figure 1.1:	NASA’s monthly summary of catalogued objects by the U.S. SSN.	3
Figure 1.2:	ESA’s yearly summary of objects orbiting Earth.	4
Figure 2.1:	Diagram of Propagator Reference Frames.	16
Figure 2.2:	Diagram of Classical Orbital Elements.	20
Figure 2.3:	Example spacecraft maneuver affect on 2D orbital geometry.	23
Figure 2.4:	Orbital energy plot for propagator validation.	24
Figure 3.1:	Diagram of Reference Frames for Observations.	30
Figure 3.2:	Example Ψ maneuver detection results for $\Delta v = 5$ m/s.	38
Figure 3.3:	Example Ψ maneuver detection results for $\Delta v = 25$ m/s.	38
Figure 3.4:	Example \mathcal{K} maneuver detection results for $\Delta v = 5$ and 25 m/s.	39
Figure 4.1:	Trend of \mathcal{K} with varied apogee radial maneuvering Δv	46
Figure 4.2:	Trend of \mathcal{K} with varied apogee transverse maneuvering Δv	47
Figure 4.3:	Trend of \mathcal{K} with varied apogee normal maneuvering Δv	47
Figure 4.4:	Trend of Ψ with varied apogee radial maneuvering Δv	49
Figure 4.5:	Trend of Ψ with varied apogee transverse maneuvering Δv	50
Figure 4.6:	Trend of Ψ with varied apogee normal maneuvering Δv	50
Figure 4.7:	Trend of \mathcal{K} with varied perigee transverse maneuvering Δv	54
Figure 4.8:	Trend of \mathcal{K} with varied Δv at a quarter of an orbit after perigee.	55
Figure 4.9:	Trend of \mathcal{K} with varied Δv at a quarter of an orbit after apogee.	55
Figure 4.10:	Trend of \mathcal{K} with varied Δv at perigee for orbital Case 2.	57
Figure 4.11:	Trend of \mathcal{K} with varied Δv at apogee for orbital Case 2.	58
Figure 4.12:	Trend of \mathcal{K} with varied Δv at apogee and $\mathbf{R} = 10\mathbf{R}$	60
Figure 4.13:	Trend of \mathcal{K} with varied Δv at apogee and $\mathbf{R} = \mathbf{R}/10$	60
Figure 4.14:	Trend of \mathcal{K} with varied Δv at apogee for $\Psi_{th} = 10$	62
Figure 4.15:	Trend of \mathcal{K} with varied Δv at apogee for $\Psi_{th} = 100$	62
Figure 4.16:	Trend of \mathcal{K} with varied Δv at apogee for $\eta_{th} = 0.1$	63
Figure 4.17:	Trend of \mathcal{K} with varied Δv at apogee and $t_{man} = 10$ seconds.	65
Figure 4.18:	Trend of \mathcal{K} with varied Δv at apogee and $t_{man} = 1000$ seconds.	65
Figure 4.19:	Trend of \mathcal{K} with varied Δv in the cm/s range at apogee.	68
Figure 4.20:	Trend of \mathcal{K} with varied Δv in the cm/s range at perigee.	68

Figure 4.21:	Transverse apogee K vs. time results for $\Delta v = 5$ cm/s.	69
Figure 4.22:	Transverse perigee K vs. time results for $\Delta v = 5$ cm/s.	69
Figure B.1:	Base filtering results of K and Ψ for no applied maneuvers.	75
Figure D.1:	Trend of K with varied Δv at perigee and $\mathbf{R} = 10\mathbf{R}$	78
Figure D.2:	Trend of K with varied Δv at perigee and $\mathbf{R} = \mathbf{R}/10$	78
Figure D.3:	Trend of K with varied Δv at perigee for $\Psi_{th} = 10$	80
Figure D.4:	Trend of K with varied Δv at perigee for $\Psi_{th} = 100$	81
Figure D.5:	Trend of K with varied Δv at perigee for $\eta_{th} = 0.1$	81
Figure D.6:	Trend of K with varied Δv at perigee and $t_{man} = 10$ seconds. . . .	83
Figure D.7:	Trend of K with varied Δv at perigee and $t_{man} = 1000$ seconds. . .	83
Figure E.1:	Trend of Ψ with varied perigee transverse maneuvering Δv	86
Figure E.2:	Trend of Ψ with varied Δv at a quarter of an orbit after perigee. . .	87
Figure E.3:	Trend of Ψ with varied Δv at a quarter of an orbit after apogee. . .	87
Figure E.4:	Trend of Ψ with varied Δv at perigee for orbital Case 2.	90
Figure E.5:	Trend of Ψ with varied Δv at apogee for orbital Case 2.	90
Figure E.6:	Trend of Ψ with varied Δv at perigee and $\mathbf{R} = \mathbf{R}/10$	91
Figure E.7:	Trend of Ψ with varied Δv at apogee and $\mathbf{R} = \mathbf{R}/10$	91
Figure E.8:	Trend of Ψ with varied Δv at perigee and $\mathbf{R} = 10\mathbf{R}$	92
Figure E.9:	Trend of Ψ with varied Δv at apogee and $\mathbf{R} = 10\mathbf{R}$	92
Figure E.10:	Trend of Ψ with varied Δv at apogee for $\Psi_{th} = 10$	93
Figure E.11:	Trend of Ψ with varied Δv at perigee for $\Psi_{th} = 10$	93
Figure E.12:	Trend of Ψ with varied Δv at apogee for $\Psi_{th} = 100$	94
Figure E.13:	Trend of Ψ with varied Δv at perigee for $\Psi_{th} = 100$	94
Figure E.14:	Trend of Ψ with varied Δv at apogee for $\eta_{th} = 0.1$	95
Figure E.15:	Trend of Ψ with varied Δv at perigee for $\eta_{th} = 0.1$	95
Figure E.16:	Trend of Ψ with varied Δv at apogee and $t_{man} = 10$ seconds. . . .	96
Figure E.17:	Trend of Ψ with varied Δv at perigee and $t_{man} = 10$ seconds. . . .	96
Figure E.18:	Trend of Ψ with varied Δv at apogee and $t_{man} = 1000$ seconds. . .	97
Figure E.19:	Trend of Ψ with varied Δv at perigee and $t_{man} = 1000$ seconds. . .	97
Figure E.20:	Trend of Ψ with varied Δv at apogee and $t_{man} = 1000$ seconds. . .	98
Figure E.21:	Trend of Ψ with varied Δv at perigee and $t_{man} = 1000$ seconds. . .	98
Figure F.1:	Detection timing of K for apogee maneuvers.	100
Figure F.2:	Detection timing of K for perigee maneuvers.	100

LIST OF TABLES

Table 2.1:	Initial and Final COEs for Validation Cases.	24
Table 3.1:	Values for Process Noise Covariance Inflation	35
Table 4.1:	Earth’s Constants Used in All Simulations	41
Table 4.2:	Apogee Coefficients for Curve Fit Lines of the $K-\Delta v$ Relationship .	46
Table 4.3:	Apogee R^2 Numbers for Curve Fit Lines of the $K-\Delta v$ Relationship .	46
Table 4.4:	Apogee Coefficients for Curve Fit Lines of the $\Psi-\Delta v$ Relationship .	49
Table 4.5:	Apogee R^2 Numbers for Curve Fit Lines of the $\Psi-\Delta v$ Relationship .	49
Table 4.6:	Perigee Coefficients for Curve Fit Lines of the $K-\Delta v$ Relationship . .	53
Table 4.7:	Perigee R^2 Numbers for Curve Fit Lines of the $K-\Delta v$ Relationship .	53
Table 4.8:	Coefficients for $K-\Delta v$ at a Quarter of an Orbit after Perigee	54
Table 4.9:	Coefficients for $K-\Delta v$ at a Quarter of an Orbit after Apogee	54
Table 4.10:	Initial Orbital Elements of Tested Orbital Cases	56
Table 4.11:	Coefficients for the $K-\Delta v$ Relationship in Orbital Case 2	57
Table 4.12:	Initial and Final COEs for Δv in the cm/s Range	67
Table 4.13:	Coefficients for the $K-\Delta v$ Relationship in the cm/s Range	67
Table C.1:	Summary of $K-\Delta v$ Relationship for Most Pertinent Tests	76
Table D.1:	Coefficients for the $K-\Delta v$ Relationship with $\mathbf{R} = 10\mathbf{R}$	77
Table D.2:	Coefficients for the $K-\Delta v$ Relationship with $\mathbf{R} = \mathbf{R}/10$	77
Table D.3:	Coefficients for the $K-\Delta v$ Relationship with $\Psi_{th} = 10$	79
Table D.4:	Coefficients for the $K-\Delta v$ Relationship with $\Psi_{th} = 1000$	79
Table D.5:	Coefficients for the $K-\Delta v$ Relationship with $\eta_{th} = 0.1$	80
Table D.6:	Coefficients for the $K-\Delta v$ Relationship with $t_{man} = 10$ s	82
Table D.7:	Coefficients for the $K-\Delta v$ Relationship with $t_{man} = 1000$ s	82
Table E.1:	Perigee Coefficients for Curve Fit Lines of the $\Psi-\Delta v$ Relationship . .	85
Table E.2:	Coefficients for $\Psi-\Delta v$ at a Quarter of the Orbit after Perigee	85
Table E.3:	Coefficients for $\Psi-\Delta v$ at a Quarter of the Orbit after Apogee	86
Table E.4:	Perigee R^2 Numbers of the $\Psi-\Delta v$ Relationship at Perigee	86
Table E.5:	Coefficients for the $\Psi-\Delta v$ Relationship in Orbital Case 2	89
Table E.6:	R^2 Numbers for the $\Psi-\Delta v$ Relationship in Orbital Case 2	89

NOMENCLATURE

a	=	Semi-major axis
\mathbf{a}_p	=	Perturbation vector matrix
\mathbf{B}	=	Input matrix to project perturbations onto the state equations
C_E, S_E	=	Auxiliary quantities for Earth
$\mathbf{C}(\cdot), \dot{\mathbf{C}}(\cdot)$	=	Direction Cosine Matrix (DCM), and DCM Differential
\mathbf{e}, e	=	Orbital Eccentricity matrix and magnitude
$\vec{F}(\cdot), \mathbf{F}(\cdot)$	=	State vector and matrix function
$\vec{\mathcal{F}}(\cdot)$	=	Reference frame vectrix
$\mathbf{G}(\cdot)$	=	Mapping matrix function
h_{ellp}	=	Height above ellipsoid reference
\vec{h}, \mathbf{h}, h	=	Orbital Angular Momentum vector, matrix and magnitude
\mathbf{H}	=	Observation Partial or Measurement Sensitivity Matrix
i	=	Orbital Inclination
J_2	=	Geopotential perturbations representation due to the oblateness of the Earth
$\mathbf{K}, \mathbf{K}_{th}, \mathbf{K}_{max}$	=	New Kaderali Detection Parameter, Threshold and Maximum
\mathbf{K}	=	Kalman Gain Matrix
p	=	Semi-latus rectum
$\mathbf{P}, \hat{\mathbf{P}}, \bar{\mathbf{P}}$	=	State Covariance Matrix, Estimate, and Prediction
\mathbf{Q}	=	Process Noise Covariance Matrix
r_a, r_p	=	Apogee and Perigee Radii, respectively
\vec{r}, \mathbf{r}, r	=	Position vector, matrix, magnitude
$\ddot{\mathbf{r}}$	=	Two-body orbital acceleration matrix
\mathbf{R}	=	Measurement Noise Covariance Matrix
\mathbf{S}	=	Observation Noise Covariance Matrix
t, t_0	=	Time variable, initial time
$\vec{U}, \mathbf{U}_{3x1}$	=	Thrust motion vector and matrix
\vec{v}, \mathbf{v}, v	=	Velocity vector, matrix and magnitude
$\dot{\mathbf{X}}$	=	State vector differential
$\mathbf{X}, \hat{\mathbf{X}}, \bar{\mathbf{X}}$	=	State Vector, Estimate, and Prediction
$\mathbf{y}, \hat{\mathbf{y}}$	=	Observation set and calculated observation estimate set

β	=	Azimuth angle
$\Delta \mathbf{v}, \Delta v$	=	Applied velocity change matrix and magnitude (due to maneuver thrust)
ε	=	Total Orbital Energy
el	=	Elevation angle
η, η_{th}	=	State covariance inflation trace parameter and threshold
θ_{GMT}	=	Greenwich Mean Time argument angle
$\theta_{(\cdot)}$	=	Euler Angle argument with respect to an axis for DCMs
κ, κ_{\max}	=	Equivalent to the New Kaderali Parameter, and Parameter Maximum
λ	=	Longitude
μ	=	Gravitational Parameter of the Earth
ν	=	True Anomaly
ν_e	=	Calculated filter residuals
$\nu, \text{ or } \theta$	=	True anomaly
ρ	=	observation range vector
Φ	=	State Transition Matrix
ϕ_{gd}	=	Geodetic latitude
Ψ, Ψ_{th}	=	Original Detection Parameter and Threshold
ω	=	Argument of perigee
Ω	=	Right Ascension of the Ascending Node (RAAN)
$(\cdot)_{ECF}$	=	Earth-Centred-Earth-Fixed Reference Frame subscript
$(\cdot)_{ECI}$	=	Earth-Centred Inertial Reference Frame subscript
$(\cdot)_{PQW}$	=	Perifocal or Orbital Reference Frame subscript
$(\cdot)_{RSW}$	=	Spacecraft Reference Frame subscript
$(\cdot)_{SEZ}$	=	Topocentric Horizon Reference Frame subscript
$(\cdot)_i$	=	Time-dependant variable subscript indicator
$\mathbf{0}_{3 \times 3}$	=	3×3 Zero Matrix
$\mathbf{I}_{3 \times 3}$	=	3×3 Identity Matrix

ACRONYMS

AFSPC	Air Force Space Command
ASA	Australian Space Agency
BLS	Batch Least Squares
CAR-MHF	Constrained Admissible Region Multiple Hypothesis Filter
CBTA	Covariance–Base Track Association
CKF	Cubature Kalman Filter
CSA	Canadian Space Agency
COE	Classical Orbital Elements
Cub-ICF	Cubature Rule Information Consensus Filter
DCM	Direction Cosine Matrix
DISP	Distinguishable and Independent Stochastic Populations
DRAMA	Debris Risk Assessment and Mitigation Analysis
ECI	Earth-Centred Inertial Frame
ECEF	Earth-Centred-Earth-Fixed Frame
EKF	Extended Kalman Filter
ESA	European Space Agency
FST	Finite–Set Statistics
GEO	Geosynchronous Orbit
GLMB	Generalized Labelled Multi-Bernoulli
GMT	Greenwich Mean Time
HELO	Highly Elliptical Orbit
ICF	Information Consensus Filter
IC	Initial Condition
IMM	Interacting Multiple Model
IMM-CKF	Interacting Multiple Model Cubature Kalman Filter
IOD	Initial Orbit Determination
ISS	International Space Station
JAXA	Japan Aerospace Exploration Agency
KF	Kalman Filter
LEO	Low Earth Orbit
LQP	Linear Quadratic Problem

LST	Local Sidereal Time
MEO	Medium Earth Orbit
MSL	Mean Sea Level
MH-JPDA	Multiple Hypothesis Joint Probabilistic Data Association
MHT	Multiple Hypothesis Tracking
MRBVP	Measurement Residual Boundary Value Problem
NASA	National Aeronautics and Space Administration
NLS	Nonlinear Least Squares
OCBE	Optimal Control Based Estimator
PDF	Probability Density Function
PQW	Perifocal or Orbital Reference Frame
RAAN	Right Ascension of the Ascending Node
RHR	Right-Hand-Rule
RMSE	Root Mean Square Error
ROKF	Reduced order Kalman Filters
RSW	Spacecraft Body Reference Frame
RTS	Rauch–Tung–Striebel
SBO	Space–Based Optical
SEZ	Topocentric Horizon or South-East-Zenith Frame
SIOD	Stastitical Initial Orbit Determination
SOC	Space Object Catalogue
SRP	Solar Radiation Pressure
SSA	Space Situational Awareness
SSN	Space Surveillance Network
STM	State Transition Matrix
TLE	Two-Line Element
TCC	TLE Consistency Check
TFC	Thrust-Fourier-Coefficient
TTSA	TLE Time Series Analysis
UCO	Uncorrelated Optical Observations
UCT	Uncorrelated Tracks
UKF	Unscented Kalman Filter
USE	Unknown Space Event
UT	Unscented Transform

CHAPTER 1

Introduction

1.1 Motivation and Background

1.1.1 The Space Environment and Debris Problem

The start of the Space Race in the 1950's, sparked interest in space all over the globe. Since the first artificial satellite, Sputnik 1, was successfully launched in 1957 [1], interests in Earth orbiting satellites have been continuously growing. With increasing appeal comes the increase of launches and satellites placed in orbit. Now, with more than 60 countries having access to space, and owning orbiting spacecraft [2], space is becoming competitive, contested, and congested [3–5]. The increase in space congestion poses great risks to current and future orbiting spacecraft. For example, in April and July 2020, the International Space Station (ISS) had to conduct collision avoidance maneuvers for break-up debris fragments tracked by the U.S. Space Command (USSPACECOM) Space Surveillance Network (SSN), which were produced by the Fengyun-1C (FY-1C) anti-satellite test by China in 2007, and the SOZ (Sistema Obespecheniya Zapuska, “Launch Support System”) auxiliary motor explosion in 2003, respectively [6].

Space technology is heavily relied upon in the daily lives of people everywhere for uses such as: GPS, navigation, location, tracking and mapping; food and agriculture monitoring; disaster management, prediction, and relief; Search-and-Rescue and emergency response efforts; climate and weather monitoring and prediction; environment and ecosystems monitoring; internet, television, communications and surveillance networks; education, sciences and medical research; and, military and defense [7,8]. What originally started as only a minimal issue with only few satellites per year placed into orbit, has become a pressing issue with more than 800 satellites placed in orbit per decade [9]. There are now more than 5,000 satellites, and over 20,000 objects larger than 10 cm orbiting the Earth [10,11]. MIT reports that there could be over 1000 satellites launching to orbit per year by 2025, especially with recent developments in mega-constellations [12]. As reliance on space technology increases, satellite insertion

rates will grow, increasing space debris and contributions to the space congestion problem.

Space debris can range from artificial objects of spacecraft parts to full satellites, and naturally occurring bodies of dust or rock, which all pose a risk to current and future spacecraft missions [13–17]. Artificial debris can also include defunct spacecraft, spacecraft paint chips, spacecraft pieces from break-up events, or used rocket bodies [11]. According to the Space Debris Office at the European Space Agency (ESA), as of 2018, artificial spacecraft contribute to 22,000 [11, 18] space objects larger than 10 cm orbiting the Earth, tracked by the SSN, which include active and inactive spacecraft [6]. ESA estimates, through statistical modelling, that over 128,000,000 objects as small as 1 mm up to greater than 10 cm are currently orbiting the Earth [18]. These debris objects include both artificial and natural objects. NASA and ESA illustrate the breakdowns and trends of the increasing orbiting objects about the Earth in Figures 1.1 and 1.2, respectively. Figure 1.1 is taken from NASA’s February 2020 edition of the Orbital Debris Quarterly News. Fragmentation debris include objects from satellite break-up and anomalous events [10]. Mission-related debris include objects placed, separated, or released from planned mission events [10]. Figure 1.2 is taken from ESA’s 2019 Annual Space Environment Report [11]. In both images the rapid growth of orbiting objects is prevalent and concerning.

Space collisions due to space objects can instigate a domino-effect of continually increasing collisions and debris [19]. As the increase in debris and space launches continue, space will become hazardous for safe satellite operations. An increase in orbiting bodies means an increase in collision probability, an increase in collisions, and an increase in debris. Kessler [16] proposes that there will be a limit of time that space travel or launches will still be safe due to the increasing congestion of objects in space. This concept of limitation is known as the *Kessler Syndrome* [13–16]. Thus, even the spacecraft important for everyday uses — e.g. positioning and navigation, communications, weather data and prediction, pandemic planning, surveillance — will be greatly and negatively impacted [20]. Hence, it is crucial for space debris to be detected, tracked, and catalogued both accurately and efficiently [3,21].

1.1.2 Astrodynamics Standards for Space Debris

In 2012, a study on the astrodynamics algorithms and associated computer systems was reported by the Committee for the Assessment of the U.S. Air Force’s Astrodynamics Standards [22]. The goals of the study were to assess the Air Force Space Command (AFSPC) astrodynamics standards established, and the effectiveness of the standards in

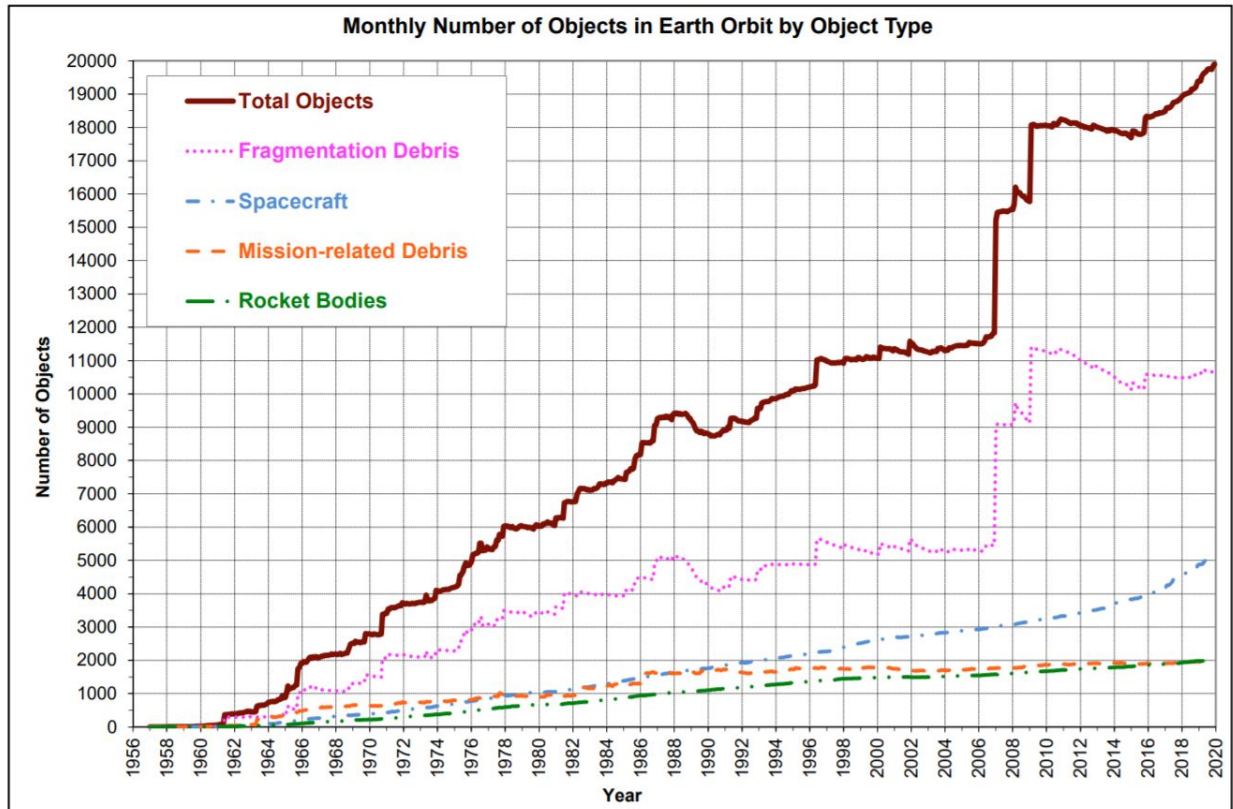


Figure 1.1: Monthly summary of all catalogued objects by the U.S. SSN from NASA’s February 2020 edition of the Orbital Debris Quarterly News [10]. Fragmentation debris include objects from satellite break-up and anomalous events. Mission-related debris include objects placed, separated, or released from planned mission events.

meeting mission performance requirements, plus possible alternatives [22]. The study was motivated by the 2009 Iridium 33 and Cosmos 2251 collision, which created over 2000 large fragments of debris (greater than 10 cm) [20], highlighting the necessity in accurately detecting and monitoring space objects in orbit. It was decided that the overall goal would be to have the capability of determining the collision probability of two space orbiting objects. It was found that the standards and algorithms being used are sufficient, and that the main limitations were sensor-based in relation to quantity and quality of data-tracking sensors [22]. Since the Cosmos–Iridium collision, there have been other notable collisions and collision risks, as highlighted in studies by Baird [20] and Ackerman [19].

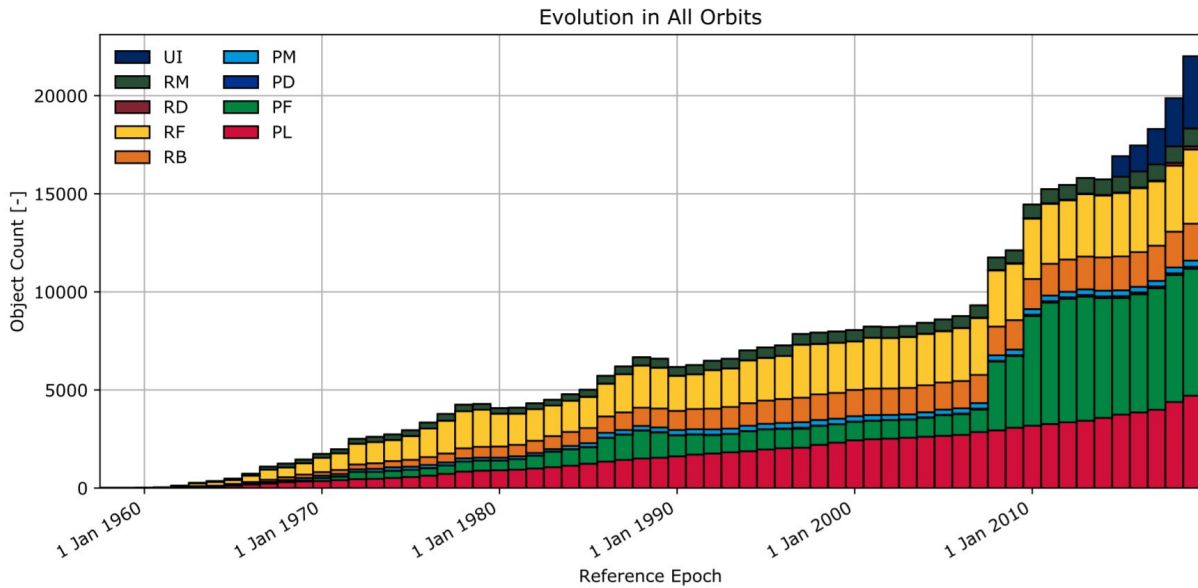


Figure 1.2: Yearly summary of objects orbiting Earth derived from the USSTRATCOM TLE set reported in ESA’s Annual Space Environment Report [11]. PL = Payload; PF = Payload Fragmentation Debris; PD = Payload Debris; PM = Payload Mission Related Object; RB = Rocket Body; RF = Rocket Fragmentation Debris; RD = Rocket Debris; RM = Rocket Mission Related Object; UI = Unidentified.

1.1.3 Space Situational Awareness (SSA) Definition

Within the field of space debris is Space Situational Awareness (SSA), which has many definitions and is important to the maintenance of the spacecraft environment as mentioned above. Kennewell and Vo [1] give a broad definition, stating that SSA is a reference to the near-space environment knowledge, both naturally occurring and human-made. In more detail, a report affiliated with the European Space Agency (ESA), defines SSA as [23]:

“... the comprehensive knowledge, understanding, and maintained awareness as far as the population of space objects in orbits, space environment, and existing threats/risks are concerned.”

ESA’s definition of SSA means that it is desirable to understand the past path of an object, its present position in space, and its future trajectory. These pieces of information are useful to determine and predict future trajectories of spacecraft, as well as any need for corrective maneuvers for collision avoidance decision-making and procedures [1].

SSA is a growing field and appeals to a range of areas including civil, military and commercial interests [3,23–25]. It is also of interest all over the world, including in many space agencies; e.g. CSA (Canadian Space Agency), [24–26], NASA (National Aeronautics and Space Administration) [3, 25, 27], JAXA (Japan Aerospace Exploration Agency) [28], ESA (European Space Agency) [23, 25, 29], ASA (Australian Space Agency) [1,25], Roscosmos (Space Agency for Russia) [25].

SSA is already a necessity for safe launches into outer space, with safely determined orbits including mitigation instruments or tools (such as thrusters) for any necessary on-orbit maneuvers, and to ensure collision risks due to space debris can be mitigated for and reduced to protect spacecraft [26, 28, 29]. In addition, SSA is useful for minimising space debris as produced by collisions, and for safe operations throughout missions [1, 23]. Thus, as stated by Holzinger et al. [30]:

“SSA [also] encompasses the detection, tracking, and characterisation of space objects.”

where space objects are updated and stored in a Space Object Catalogue (SOC).

In summary, many papers agree that SSA is related to the knowledge of the near-space environment in relation to space debris, with the ability to detect, track, and characterise the orbiting debris for uses including: orbit prediction, collision probability, risk assessment, cataloguing, and sustainability [1, 14, 17, 23, 30, 31].

1.1.4 Observation-to-Object Tracking Association Demand

Object-to-track association and propagation are important aspects of SSA and event detection. Various goals of observation association exist, which include orbital determination and spacecraft maneuver detection. Track association involves factors influencing the spacecraft orbit, such as natural perturbations (e.g. Earth’s oblateness (J_2), gravity gradient, aerodynamic drag, magnetic torque, Solar Radiation Pressure (SRP)) and artificial events (e.g. impulsive maneuvers, continuous maneuvers, break-up or berthing events). An extended goal of the process is for determining any potential for collision avoidance maneuvers to be applied based on the potential threat of an object, through orbit prediction and determination [30].

Currently, the main issue with maintenance of the SOC is sensor limitations for space object detection and characterisation of the many objects already in orbit, and the new objects planned to orbit the Earth [30]. Additionally, space object observations often occur over short time periods, providing potentially sparse data, and thus, providing minimal information for Initial Orbit Determination (IOD) algorithms [30]. Object

tracking association answers the “What” and “Where” questions of the spacecraft in observation; it sheds light on the relative positioning of the observed spacecraft to other spacecraft, the prediction of the direction the observed spacecraft is travelling, and any risks associated that would call for mitigating action. Therefore, SSA and object-to-track association are key in maneuvering spacecraft detection, characterisation, and trajectory prediction, as well as collision risk, collision avoidance maneuver necessity, and overall defense concerns [1,23,25,26], hence the growing interest in the field.

1.1.5 Event Definitions and Detection Needs

The term “Event” can be defined in several ways. In general, it describes when a spacecraft or Earth-orbiting piece of space debris has changed its trajectory. Such events can range from artificial to naturally occurring (orbital perturbations). Though naturally occurring continuous perturbations can be a factor, for the purposes of this thesis, the focus is on artificial events due to impulsive maneuvers.

To achieve full SSA, having well-rounded knowledge and determination of events occurring in space objects both catalogued and not catalogued in the SOC is necessary [21]. As discussed in Section 1.1.1, space debris and space debris due to collision events can pose great risks. With the increase in the number of orbiting spacecraft, there is increased risks of collision, and less ease of mitigation for risks as more and more partners or operators launch and operate spacecraft in space [15, 21]. Thus, if a spacecraft changes its trajectory unbeknownst to other spacecraft in its vicinity or orbital regime, it can pose a greater risk to the spacecraft. This situation highlights the need for detection methods of unknown events in spacecraft [21]. Further to this need is the need for characterisation of the event [21]. Characterisation can range from determination of the nature of the event to the intent, the direction, or the magnitude, or combination thereof. Through both detection and characterisation, it is then possible to reconstruct and predict the maneuvering spacecraft’s orbital trajectory, making it possible for operators to determine the potential risks of the spacecraft in question and determine any collision avoidance needs or alerts for potential malicious intent [21].

1.2 Event Detection Methods in Literature

There are many pieces of literature that explore the expansive aspects of SSA and space debris. Since this dissertation focuses on the detection and characterisation of unknown maneuvers in spacecraft due to artificial events orbiting about the Earth, this section presents a detailed overview of explored methods for event detection, including: filtering, thrust representation, optimisation, and Two-Line Element (TLE) methods.

In all methods, object-to-track association and propagation are important aspects, as well as the use of filters or algorithms to deduce the occurrence of an event, and the potential for real-time detection or characterisation. Three main topics are explored: single event detection and characterisation; filtering approaches; and, other scenarios including event detection with either multi-sensor tracking or multi-object tracking.

1.2.1 Object Track Association and Event Detection

With object-to-track association, uncorrelated tracks (UCTs) may occur in the observation and object association process, where space object tracks may not correlate to known objects in the SOC [32,33]. In this process, a minimum of 3 tracks must be correlated for the object to be catalogued. Additionally, all space objects start as UCTs, proving to be one of the most challenging components of SSA [33]. Sabol et al. [33] explain that at large time differences between tracks, orbital errors can grow quite large, becoming non-Gaussian, and producing negative effects on the UCT correlation [33]. They explore the nonlinear effects of this result on the accuracy and covariance to be used in UCT correlation. They also analyse the best coordinate system for use in an unscented Kalman filter (UKF), and assess how their approaches could assist in correlating tracks further separated in time [33]. Sabol et al. [33] found that covariance-base track association (CBTA) is effective if the measurement error statistics are accurately modelled, and thus, it becomes easier to associate UCTs [33]. It was also concluded that the Monte Carlo approach in their analysis presented the best performance with the UKF which was concluded as promising for track-to-track varying biases, e.g. through radar measurements [33].

As described in an updated report originally published in 1997 by Alfriend [32], common UCT sources include break-up events, maneuvered operational spacecraft, or occasionally tracked small objects — which are only observed and tracked dependant on radar capabilities, as well as object orientation. These objects are not able to be included in the SOC. Alfriend [32] explains that the determination of UCT-to-Space-Object association for cataloguing has been a time-consuming manual process, and it is desired to be efficiently automated, as new objects continuously appear, becoming too intensive

for the manual process. By considering the changing uncertainty of state variables and observing the probability density functions (PDFs) of numerical experiments and simulations, Alfriend [32] was able to propose a covariance-based algorithm for processing UCTs. However, the experiment returned many large values of the scaled standard deviation of the semi-axes length of an n-dimensional ellipsoid [32]. This indicated that sensor errors, noise sigmas, and noise biases were modelled incorrectly [32]. Both Alfriend [32] and Sabol et al. [33] make use of the Mahalanobis Distance — where the statistical distance between two tracks at a common time are used for association [33,34] — to assist in the UCT determination process.

1.2.2 Single Event Detection and Characterisation

In the work by Scheeres et al. [35], a study was performed for maneuver detection using two methods that included non-Gaussian elements, non-linearity in the equations of motion, and an observability analysis [35]. The first approach provided estimates for filtering approaches and development of new algorithms for event detection relative to an assumed level of background noise and orbit determination uncertainty. The second approach used a linearised filtering method, using process noise and artificially enhancing sensor sensitivity to improve current filtering methods. This method was capable of producing an acceleration profile of the spacecraft representing several possible maneuvers and unmodelled forces acting on the spacecraft with respect to a background noise threshold [35]. The two approaches were found successful in tracking the maneuvering satellite through its changed state, including cases in which the satellite or maneuvers were not tracked, as well as in reconstructing the past spacecraft trajectory and predicting its future trajectory [35].

In the thesis by Ko [36], Fourier series based Thrust-Fourier-Coefficients (TFCs) are used as an event representation method for maneuver detection. This method used the known pre-event orbit solution to determine the post-orbit solution. The TFCs are then used to represent the unknown trajectory change, and connect the original and new spacecraft states [36]. The work by Ko [36] was an extension of the work by Hudson and Scheeres [37, 38], where a control law finds a solution to present the apparent secular behaviour due to the USE, as opposed to characterising the maneuvering event. The method presented by Ko was tested in LEO simulations using either a modified Batch filter or a modified Extended Kalman Filter (EKF) for impulsive burns, continuous low-thrust maneuvers, and a structural deployment. It was found that the implemented method was able to estimate the maneuver onset and termination times from the

observational data in the two filtering systems as a knowledge-free detection scheme, and proves the tracking of the spacecraft can be maintained [36].

In a study by Jia et al. [39], an Interacting Multiple Model (IMM) filter concept is used and applied to a Cubature Kalman Filter (CKF). The multiple models of the IMM have different process noise levels to distinguish the maneuvering effects. The IMM-CKF then simultaneously tracks space objects and detects maneuver events from Space-Based Optical (SBO) sensor data, by considering the geometry relations between the SO, the SBO sensor, and the Sun. It was found that the relational geometry of these 3 components affect the quality of observations [39]. For testing the performance of the filtering processes, a simulation of a space object with 4 SBOs was completed, and the performance was compared to the ordinary CKF [39]. It was found that the IMM-CKF provided higher robustness than the CKF in a maneuver event with an SO, and that the maneuver detection can be concurrently obtained [39]. Jia et al. [39] explain in their study that tracking a space object and detecting a maneuver event simultaneously are necessary, as often the two are obtained separately and are affected by the light-time of the observation. Different scenarios and tracking methods are still to be studied and compared by Jia et al. [39].

In another study by Jia et al. [40] cooperative tracking is performed through a consensus-based algorithm, where the information consensus filter (ICF) is used for tracking space objects from multiple SBOs, and is improved on by using the Cubature rule embedded ICF (Cub-ICF). It is found that their solution is more robust than the ICF alone, solving the large errors problem, and can reach similar performance to consensus based centralised filters [40]. It is explained that this method can lead to robustness in space object tracking against sensor failures, computations, and complex network protocols [40]. To test the algorithm, a similar process to [22] is completed, in a scenario of one space object observed by four SBO sensors.

In a study by Goff et al. [41] the tracking problem is described as separable into two considerations: 1) Data association; 2) Real-time tracking. Another approach for object tracking and maneuver detection is presented, through EKF modification and IMM process implementation with covariance inflation, which is to be executed after the detection of an impulsive maneuver, removing the necessity of reconstruction through post-processing [41]. A weighted maneuver detection parameter was used to determine the impulsive maneuver, based on the residuals in the filter. Filter efficacy was measured through comparison of the known original orbit and the filter predicted maneuvered trajectory. Goff et al. [41] were able to successfully determine the time at which a maneuver occurred in real-time — unlike other approaches such as IOD or BLS. It was

also concluded that a relationship between the weighted maneuver detection parameter and the impulsive maneuver exists, where larger maneuvers resulted in larger magnitudes of the weighted detection parameter [41].

Lee and Hwang [42] also use an IMM approach for maneuver detection and characterisation. They make the assumption that maneuvered spacecraft result in changed orbital elements due to finite maneuvers, which allows for a jump Markov nonlinear system model with multiple modes [42]. The method is proved effective through tested simulations.

1.2.3 Other Event Detection Methods

Holzinger and Scheeres [43], utilised a control cost function method as a distance metric for object-track correlation and maneuver detection. This method used a Measurement Residual Boundary Value Problem (MRBVP) approach [43]. Expected measurements were calculated using a sensor measurement model. The method was used for the first new measurement after an observation gap in the data to provide a maneuver detection characterisation immediately upon track acquisition [43]. It was found that as the measurement residuals would tend to zero, the observation occurred exactly as expected [43]. As the random variables parameter tended to zero, the system became completely deterministic, becoming a function purely of measurement residuals [43]. It was concluded that the MRBVP method was an optimal control method for minimising the control distance metric, utilising a calculus of variations approach.

Lubey and Scheeres [44] proposed an adaptive controls technique for a nonlinear solution using an Optimal Control Based Estimator (OCBE), which produced optimal control policies for representing mismodelled state dynamics due to data-sparse measurements. The mismodelling was evaluated for statistical significance to determine a maneuver event. Lubey and Scheeres [44] built upon Holzinger et al.'s [45] single statistical measurement metric, expanding to three OCBE distance measure metrics, forming the cost function. The estimator was automated and applied to a GEO tracking problem of a spacecraft making periodic stationkeeping maneuvers unbeknownst to the estimator. It was concluded that this method was able to continue tracking the maneuvering object while also detecting and reconstructing the mismodelled dynamical system, and characterise the maneuvers by order of magnitude and direction [44].

Lemmens and Krag [46] developed two methods for space event detection based on Two-Line Element (TLE) history analysis: 1) Non-natural anomalous LEO event detection through TLE Consistency Checks (TCCs), where published data is compared to propagated data; 2) TLE Time Series Analysis (TTSA), for harmonic and statistical

analysis of the time series in the orbital elements, extrapolating series behavioural information to make measurements [46]. This work was to be used in assessing spacecraft operator compliance with the Integration Space Debris Coordination Committee guidelines with respect to the LEO safe region, and on impulsive velocity changes [46].

Patera [47], proposed a method for objects tracked by the Cheyenne Mountain Operations Centre. Events studied included both artificial and natural causes. The method involved a window-moving curve fit technique; filtering noise and processing the time-varied data. A detection was determined when a parameter exceeded the allowable deviation from the predetermined respective threshold defined by standard deviations. TLEs were utilised in the object association portion, and energy dispersion computations updated the statistical maneuver detection determination [47]. The process was completed for all available space objects until an event was declared, moving the process to event analysis. It was found that the technique was able to accommodate secular orbital variations and only detect the abrupt or impulsive orbital changes for event declaration. Patera [47] concluded that the method was effective, taking minimal time for processing the SOC (within minutes for a one year catalogue), and could be implemented in either batch or recursive filtering.

Sanchez and Krag [48] utilised a method of comparison between object miss-distances and a defined distance threshold or the computed associated risk of collisions and level of collision probability. The study focussed on the accuracy required for differing regimes of orbit — in keeping the number of false alarms low — and the associated current risks, using ESA's Debris Risk Assessment and Mitigation Analysis (DRAMA) tool [48]. This work was mainly geared towards collision risk and avoidance as opposed to maneuver detection and characterisation.

1.2.4 Multi-Object Tracking and Event Detection

Jones et al. [17], as previously mentioned, described the unique challenges associated with multi-object tracking of space objects, stating that standard models fail in producing results. They stated, simple traditional models that are linear and in discrete-time are not accurate for the case of space objects, due to the nonlinear motion, and thus, current Monte Carlo filters are restricted by high computational costs [17]. System requirements for SSA were outlined and the method of tracking performance with a δ -Generalised Labelled Multi-Bernoulli (δ -GLMB) filter was described. The method was compared to traditional filtering models. Jones et al. [17] pointed out that a common conclusion in the astrodynamics community is that improved methods are

needed for tracking space objects, reducing UCTs, and improving orbit estimates. However, the caveat is, each technique must be customised for each astrodynamics application [17].

Stauch et al. [31] applied a Multiple Hypothesis Joint Probabilistic Data Association (MH-JPDA) algorithm with a fixed-interval smoother for simultaneous multi-object tracking. The goal was to gain better estimations with newly discovered objects having large initial uncertainties due to close spacing between objects. Additional goals included: avoiding ambiguous data associations, poor state estimations, and filter divergence. The MH-JPDA enabled immediate track formation with real-time state estimates and was applied to the Constrained Admissible Region Multiple Hypothesis Filter (CAR-MHF) for a geosynchronous break-up event [31]. The CAR was to constrain the ambiguity of a short track-let [31]. Stauch et al. [31] found that using a Rauch-Tung-Striebel (RTS) UKF with the MH-JPDA method significantly reduced track errors, and allowed for the strategy of establishing track promotion, resulting in the convergence of a better accuracy for prediction and object association.

DeMars et al. [49] explored the use of a Bayesian framework with a finite-set statistics (FST) basis, as it can handle multi-object estimation problems and allow for estimations of object characteristics. The goal was to integrate the approach to common problems associated with space objects — detection, tracking, characterisation, data association [49] — so as to maintain information that would otherwise be lost. Desired tasks included: new object detection, detected object tracking, and tracked object characterisation [49]. Considered issues with space object detection included: data with high noise levels, misdetections, and clutter sources resulting in false alarms [49]. The main disadvantage found was the high computational demand for real-time processing, as is commonly found with SSA and space object tracking problems [49]. However, DeMars et al. [49] found that the method was successful in tracking 25 objects in orbit that were randomly generated in GEO. Overall, the method was concluded as successful in tracking for all tested cases [49].

Delande et al. [50] explored a filtering method called the Distinguishable and Independent Stochastic Populations (DISP) filter designed for handling multi-target problems on detection and tracking in challenging environments [50]. Delande et al. [50] simulated 5 objects on different orbits without prior information that were observed by 2 sensors. Simulations included: missed detections, measurement noise, and false-alarm issues [50]. It was found that the filter was responsive and robust in creating tracks after the first detection and maintaining object-to-track association. For the future, Delande et

al. [50] want to utilise the orbital elements to encapsulate a wider sensor model range applicable to SSA and incorporate large-scale scenarios.

Singh et al. [51] used the MHT method in multiple space regimes for multi-sensor multi-object tracking scenarios. The method was automated for SOC maintenance with expandable uses — i.e. object identification, break-up processing, and UCT/UCO (uncorrelated optical observations) resolution [51]. It was found that the MHT method was able to process a high amount of UCTs/UCOs (on the order of tens of thousands), emanating from hundreds of closely-spaced objects, and tens of thousands of widely-spaced objects, in real-time with lower computational power requirements than other methods [51]. In the LEO test, the MHT method was able to address challenges proposed by breakup events. In MEO, it was able to deal with angles-only optical observations with a unified multi-frame framework [51]. Additionally, it was able to detect which UCOs were from GEO when tested in MEO, GEO, and HELO [51].

Olivier et al. [52] modelled the breakup event caused by the Cosmos-Iridium Collision that occurred in 2009 and sparked the need for SSA to be seriously and efficiently improved. To obtain the physical and orbital characteristics of the resulting debris from the collision, a hydrodynamic simulation of the impact was performed. It was found that the remaining 65 active satellites in the Iridium constellation had a 50% increased risk of debris collisions following the event [52].

1.3 Thesis Objectives

As discussed in the beginning of this chapter, SSA is an important and pressing subject, necessitating in the track-based knowledge of spacecraft in the environment, where space objects that may change from their expected trajectories can cause issues — i.e. collisions — to neighbouring spacecraft. Artificially caused changes in spacecraft trajectories are defined as the events of interest for this research. Several methods were studied that can evaluate and determine the spatial and temporal states of a spacecraft, determining the maneuvering properties of the spacecraft. However, these methods are often complex, involving multiple layers of processes and high computational demands. Thus, the main objective of this dissertation is to establish a simple and less computationally demanding method for detecting and characterising unknown maneuvers in spacecraft.

Additional goals were desired including: implementation of the method to existing EKF/CKF procedures in MATLAB; application to multiple maneuver events over a period of time; application to break-up events; and, application with multiple sensor scenarios. However, due to complexity of the problems and time constraints, these objectives have become goals for future work.

1.4 Thesis Outline

In the next chapter, Chapter 2, a brief overview of orbital dynamics involved for spacecraft and for attaining simulated data is presented. The orbital propagation method is exemplified and validated. In Chapter 3, a walk-through of the theories and mathematics behind the processes of the chosen event detection and characterisation methods are explained, and the algorithm processes are detailed. Filtering options are discussed and preliminary results for validating the chosen method are presented. Chapter 4 contains the results obtained by the chosen method, and presents a discussion on the findings, with implications for application. The thesis is wrapped up in Chapter 5 with final conclusions and a look ahead to possible future work in relation to the findings and the additional thesis goals mentioned above.

CHAPTER 2

Orbital Propagation

2.1 Orbital Mechanics and Orbital Propagator

In order to simulate orbital data for maneuver detection and analysis, an Orbital Integrator is needed to propagate the spacecraft orbital states from an original orbit, through a maneuver, to a final orbit. The propagator must be able to include thrust effects, while illustrating the original and final orbits. It is assumed that all cases will be considered as 2-body problems to simplify the setup process. This section will walk through the process, setup, and verification of the simulated data.

2.1.1 Vectors, Reference Frames, and Frame Rotations

The propagator uses position and velocity vector components (\mathbf{r} , \mathbf{v} , respectively; where, the boldface font denotes a physical vector or column matrix, depending on the context) to describe the dynamics of the spacecraft. These vector components can be represented in any reference frame with appropriate frame rotations applied. Three reference frames are used in this propagator: Earth-Centered Inertial (ECI; $\vec{\mathcal{F}}_{ECI}$); Perifocal (PQW; $\vec{\mathcal{F}}_{PQW}$); Spacecraft Body (RSW; $\vec{\mathcal{F}}_{RSW}$). These frames are illustrated in Figure 2.1.

The ECI frame ($\vec{\mathcal{F}}_{IJK}$) is a commonly used frame for orbital mechanics [53]. Its origin is based at the centre of the Earth. The I -axis points to the vernal equinox, the K -axis, extends through the North Pole (the polar rotational axis of the Earth), and the J -axis completes the triad by the Right-Hand-Rule (RHR). Thus, the I - and J - axes are aligned with the ecliptic plane of the Earth. The ECI frame is not fixed to the Earth, and does not rotate with the Earth. Though the ECI frame is not truly inertial, as explained in [53], it can be considered as such for this context.

The PQW frame ($\vec{\mathcal{F}}_{PQW}$) is commonly used for satellite observation processing and is useful for understanding orbital motion with respect to the inertial mass [53]. This system is a satellite-based reference frame and uses the spacecraft orbit for definition. The origin is still placed at the centre of the Earth, however, the system is based on the orbital plane of the satellite. The P -axis points to the orbital perigee, the W -axis is normal to the orbital plane, and the Q -axis completes the RHR triad. Satellite motion is in the P - Q plane, and

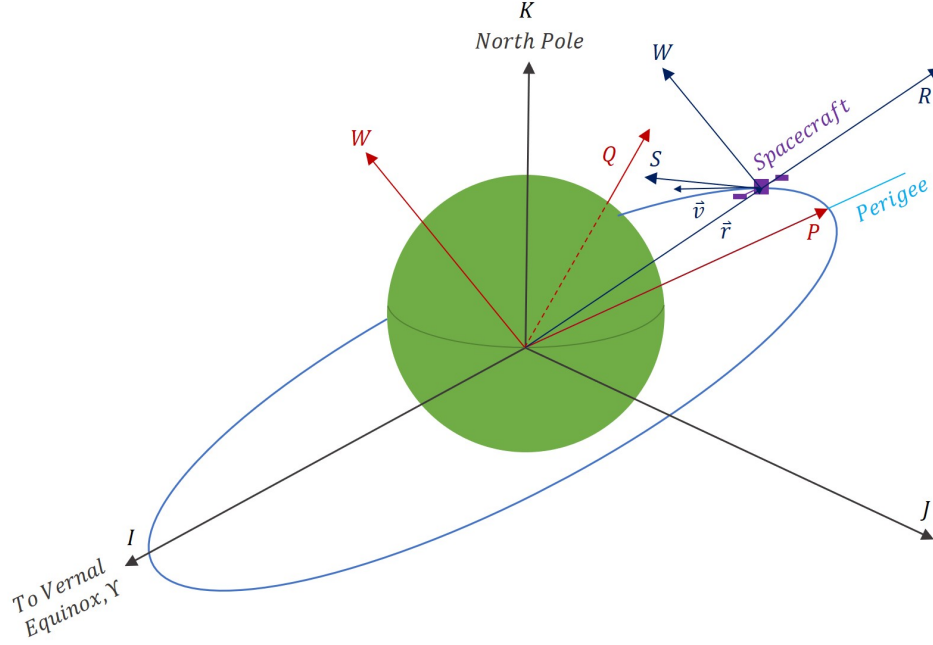


Figure 2.1: Diagram of Reference Frames to be used in propagator process based on [53]; Earth-Centred Inertial (ECI; $\vec{\mathcal{F}}_{IJK}$), Orbital/Perifocal ($\vec{\mathcal{F}}_{PQW}$), Spacecraft/Body ($\vec{\mathcal{F}}_{RSW}$).

thus, the P - and Q - axes are inclined and aligned with the spacecraft orbital plane. This frame is best used for orbits with a nonzero eccentricity [53].

Lastly, the RSW frame ($\vec{\mathcal{F}}_{RSW}$) is another satellite-based system — also known as the Spacecraft Body Frame. It is often used for understanding relative motion of a spacecraft, for example with attitude, and moves with the satellite [53]. Thrust is often defined in this frame as a vector acting on the spacecraft body. The system origin is at the spacecraft (which is modelled as a particle), and the frame moves with the spacecraft. The R -axis (*radial* direction) points along the position vector from the Earth to the spacecraft. The W -axis (*cross-track* direction) is normal to the orbital plane. The S -axis (*along-track* or *transverse* direction) is perpendicular to the R -axis, within the orbital plane, completing the RHR triad. This axis is only aligned with the spacecraft velocity vector for circular orbits ($e = 0$). This system can be used for all orbit types [53].

Components defined in each reference frame can be transformed to any other frame through what are known as Direction Cosine Matrices (DCMs, denoted \mathbf{C}). In general terms, the notation \mathbf{C}_{ba} denotes the DCM needed to rotate Frame- a ($\vec{\mathcal{F}}_a$) to Frame- b ($\vec{\mathcal{F}}_b$), completely describing the orientation of $\vec{\mathcal{F}}_b$ with respect to $\vec{\mathcal{F}}_a$. DCMs can then be

applied to position and velocity vector components, in general, as follows:

$$\mathbf{r}_a = \mathbf{C}_{ab}\mathbf{r}_b \quad \text{and} \quad \mathbf{r}_b = \mathbf{C}_{ba}\mathbf{r}_a \quad \text{where} \quad \mathbf{C}_{ba} = \mathbf{C}_{ab}^T$$

Often, DCMs are expressed in terms of principal rotations, where the subscript denotes the axis (e.g. 1 = x -axis, 2 = y -axis, 3 = z -axis), the Euler angle (or angle of rotation, $\theta_{(\cdot)}$) is defined and acts as the argument [53,54]:

$$\mathbf{C}_1(\theta_1) = \begin{bmatrix} 1 & 0 & 0 \\ 0 & \cos \theta_1 & \sin \theta_1 \\ 0 & -\sin \theta_1 & \cos \theta_1 \end{bmatrix}, \quad \mathbf{C}_2(\theta_2) = \begin{bmatrix} \cos \theta_2 & 0 & -\sin \theta_2 \\ 0 & 1 & 0 \\ \sin \theta_2 & 0 & \cos \theta_2 \end{bmatrix}, \quad (2.1)$$

$$\mathbf{C}_3(\theta_3) = \begin{bmatrix} \cos \theta_3 & \sin \theta_3 & 0 \\ -\sin \theta_3 & \cos \theta_3 & 0 \\ 0 & 0 & 1 \end{bmatrix}$$

where, $\theta_{(\cdot)}$ = Any Euler Angle or angle of rotation argument with respect to a defined axis of rotation.

Frame rotations can be conducted as a combination of stacked principal rotations, which are completed in reverse order of multiplication, denoted by the axes subscripts; e.g. $\mathbf{C}_{312}(\theta_3\theta_1\theta_2) = \mathbf{C}_2(\theta_2)\mathbf{C}_1(\theta_1)\mathbf{C}_3(\theta_3)$. Since filtering of the simulated data will also be needed, and often filters are based in the ECI frame, transformations into the ECI frame from PQW and RSW are as follows [53]:

$$\mathbf{C}_{313}(\Omega, \omega, i) = \begin{bmatrix} \cos \Omega \cos \omega - \sin \Omega \sin \omega \cos i & -\cos \Omega \sin \omega - \sin \Omega \cos \omega \cos i & \sin \Omega \sin i \\ \sin \Omega \cos \omega + \cos \Omega \sin \omega \cos i & -\sin \Omega \sin \omega - \cos \Omega \cos \omega \cos i & -\cos \Omega \sin i \\ \sin \omega \sin i & \cos \omega \sin i & \cos i \end{bmatrix}$$

$$\mathbf{C}_3(\nu) = \begin{bmatrix} \cos \nu & \sin \nu & 0 \\ -\sin \nu & \cos \nu & 0 \\ 0 & 0 & 1 \end{bmatrix} \quad (2.2)$$

where, $\mathbf{C}_{313}(\Omega, \omega, i)$ = DCM for PQW \rightarrow ECI,

$\mathbf{C}_3(\nu)$ = DCM for PQW \rightarrow RSW;

Use either: $\mathbf{C}_3(-\nu)$ or $\mathbf{C}_3^{-1}(\nu)$ for RSW \rightarrow PQW,

Such that: $\mathbf{C}_{313}(\Omega, \omega, i)\mathbf{C}_3^{-1}(\nu)$ is used for RSW \rightarrow ECI

Ω, ω, i, ν = COEs defined in Section 2.1.3.

2.1.2 Spacecraft Dynamics Equations of Motion

Now, with the reference frames and orbital elements defined, the position and velocity vectors can initially be expressed in the Perifocal Reference Frame as follows:

$$\begin{aligned}\vec{r} &= \vec{\mathcal{F}}_P \mathbf{r}_{PQW} \\ \mathbf{r}_{PQW} &= \begin{bmatrix} r_P \\ r_Q \\ r_W \end{bmatrix} = \begin{bmatrix} \frac{p \cos \nu}{1+e \cos \nu} \\ \frac{p \sin \nu}{1+e \cos \nu} \\ 0 \end{bmatrix}\end{aligned}\quad (2.3)$$

$$\begin{aligned}\vec{v} &= \vec{\mathcal{F}}_P \mathbf{v}_{PQW} \\ \mathbf{v}_{PQW} &= \begin{bmatrix} v_P \\ v_Q \\ v_W \end{bmatrix} = \begin{bmatrix} -\sqrt{\frac{\mu}{p}} \sin \nu \\ \sqrt{\frac{\mu}{p}} (e + \cos \nu) \\ 0 \end{bmatrix}\end{aligned}\quad (2.4)$$

where $p = a(1 - e^2)$ and is known as the semilatus rectum, a is the semi-major axis, e is the eccentric anomaly, ν is the true anomaly, and μ is Earth's gravitational parameter, which are all further discussed in Section 2.1.3. These \mathbf{r} and \mathbf{v} vectors can then be rotated into the ECI frame using the $\mathbf{C}_3^{-1}(\nu)$ rotation matrix form of Equation (2.2), which build the basis of the equations of motion. An overall vector (\mathbf{X}) can be used to contain all of the position and velocity vector information:

$$\mathbf{X}_{PQW} = \begin{bmatrix} \mathbf{r}_{PQW} \\ \mathbf{v}_{PQW} \end{bmatrix}$$

which can also be rotated as necessary.

Since the propagator is based as an integrator, the equations of motion for the spacecraft must be in differential form, and the equations for acceleration must be included. The two-body orbital acceleration ($\ddot{\mathbf{r}}$) is defined using the Keplerian two-body equation of motion for spacecraft, accounting only for the gravitational force acting on the spacecraft as induced by the Earth at specified distances (\mathbf{r}), to which the perturbation forces (\mathbf{a}_p) have been added (Cowell's Formulation) [53]:

$$\ddot{\mathbf{r}} = -\mu \frac{\mathbf{r}}{|\mathbf{r}|^3} + \mathbf{a}_p \quad (2.5)$$

The perturbation vector (\mathbf{a}_p) can include any kind of perturbation forces acting on the spacecraft (i.e. natural and artificial) [53]. For this propagator, the perturbation vector

includes only the instantaneous thrust vectors (contained by $\mathbf{U}_{3 \times 1}$), which are related to the applied change in velocity due the maneuver ($\Delta \mathbf{v}$ [53, 54]) over the maneuvering time (t_{man}), such that: $\mathbf{U}_{3 \times 1} = \Delta \mathbf{v} / t_{man}$. Thus, the differential form of the equations are written as follows:

$$\begin{aligned} \dot{\mathbf{X}} &= \begin{bmatrix} \dot{\mathbf{r}} \\ \dot{\mathbf{v}} \end{bmatrix} = \begin{bmatrix} \dot{\mathbf{r}} \\ -\mu \frac{\mathbf{r}}{|\mathbf{r}|^3} + \mathbf{a}_p \end{bmatrix} \\ &= \begin{bmatrix} \dot{\mathbf{r}} \\ -\mu \frac{\mathbf{r}}{|\mathbf{r}|^3} \end{bmatrix} + \begin{bmatrix} \mathbf{0}_{3 \times 3} \\ \mathbf{I}_{3 \times 3} \end{bmatrix} \mathbf{U}_{3 \times 1} \\ &= F(\mathbf{X}, t) + \mathbf{B}\mathbf{U} \end{aligned} \quad (2.6)$$

where,

$$\mathbf{a}_p = \begin{bmatrix} \mathbf{0}_{3 \times 3} \\ \mathbf{I}_{3 \times 3} \end{bmatrix} \mathbf{U}_{3 \times 1} = \mathbf{B}\mathbf{U}_{3 \times 1}$$

and, \mathbf{r} = The orbital position vector in the respective frame,

\mathbf{B} = The input matrix [55]; projects the perturbation onto the state equations [56],

\mathbf{a}_p , = The perturbation vector per the respective frame,

$\mathbf{U}_{3 \times 1}$ = The thrust motion vector per the respective frame.

which can also be written in vector form [56]:

$$\dot{\vec{X}} = \vec{F}(\vec{X}) + B\vec{U}(\vec{X}) \quad (2.7)$$

2.1.3 Classical Orbital Elements (COEs)

This section presents a review of orbital elements used in the propagator process, which can be found in various texts. This information is included for completeness, convenience and understanding for the reader. In general, orbital elements are a set of parameters consisting of up to six elements that fully describe the state of an orbiting object at a point in time. These elements can consist of position (\mathbf{r}) and velocity (\mathbf{v}) components, which are then stored in an overall state vector (\mathbf{X}) [53]. The Classical Orbital Elements (COEs) are a related six-element set used to achieve this orbital description goal [53]. The common set is comprised of: two geometry elements — the semi-major axis (a) and eccentricity (e); three angular orientation elements — inclination (i), Right Ascension of the Ascending Node (RAAN, Ω), argument of perigee (ω); and, one position-time relation element — true anomaly, (ν). Often, a time component can be considered as a seventh element, but will not be included as such for this context, as time is included in the true anomaly component [53]. An illustration of these COEs is presented in Figure 2.2.

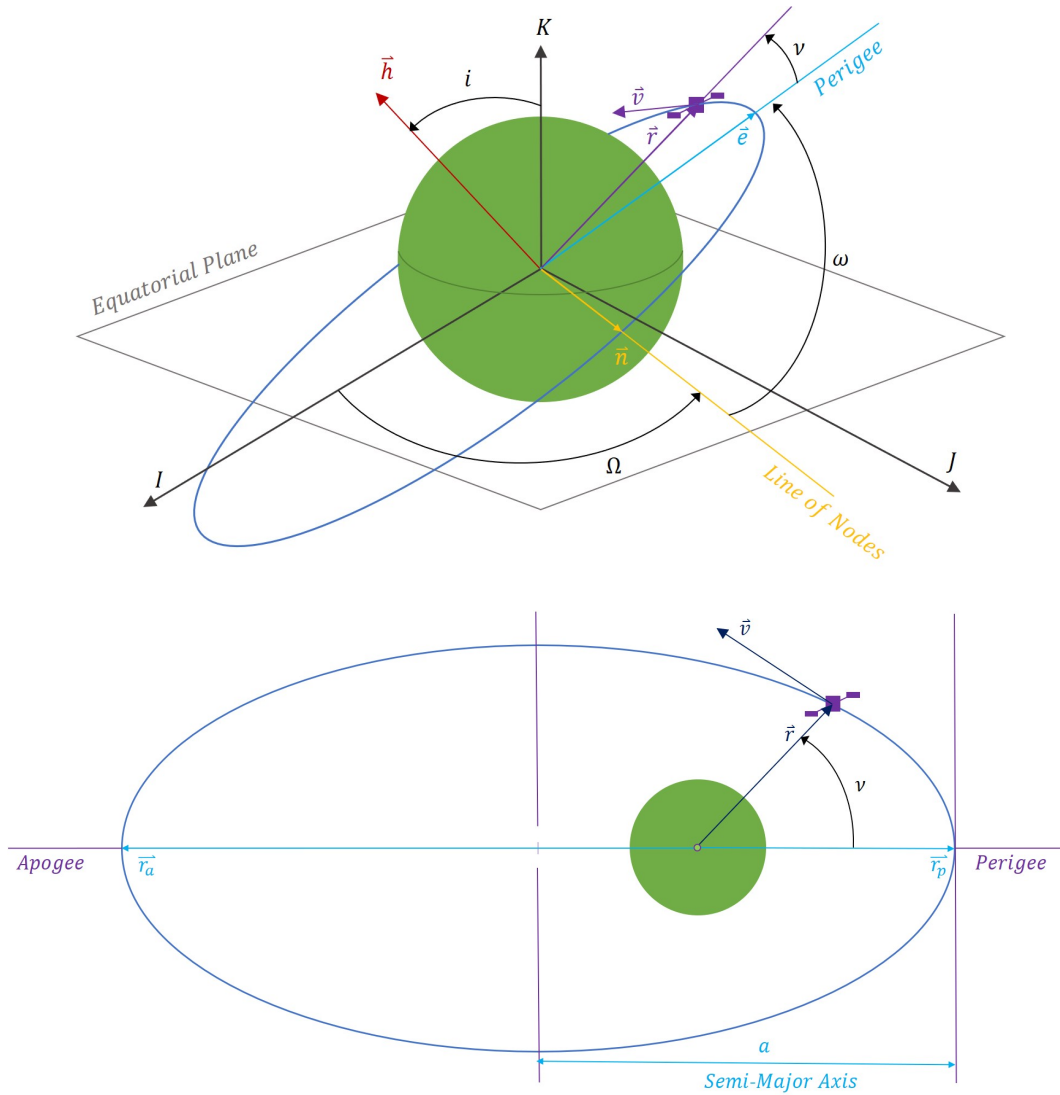


Figure 2.2: Diagram of Classical Orbital Elements (COEs) based on [53,54]. The top image illustrates COE vectors and orientation elements. The bottom image illustrates orbital geometry elements.

The semi-major axis (a) and, eccentricity (e) are the dimensional elements describing the size and shape of the orbit, and are defined by the orbital geometry. The semi-major axis is the longest radius of the orbit from the orbital centre to the orbital perimeter. It can be derived from geometry, calculated from the magnitudes of the position (\mathbf{r}) and velocity vectors (\mathbf{v}), or from the orbital energy (ϵ) magnitude [53]:

$$a = \frac{r_a + r_p}{2} = \frac{r}{2 - \frac{rv^2}{\mu}} = -\frac{\mu}{2\epsilon} \quad (2.8)$$

where,

$$\varepsilon = \frac{|\mathbf{v}|^2}{2} - \frac{\mu}{|\mathbf{r}|} = \frac{-\mu}{2a} \quad (2.9)$$

$$r = |\mathbf{r}|, \quad v = |\mathbf{v}|$$

and, $\mu = 3.986 \times 10^5 \text{ km}^3/\text{s}^2$ is the gravitational parameter of the Earth. Eccentricity (e) is a nondimensional measure describing the ellipticity of the orbit (i.e. the amount that the orbit deviates from a circle). For circular orbits, a is equal to the radius of the orbit, thus $e = 0$. For elliptical orbits, $0 < e < 1$. The eccentricity can be calculated from the position (\mathbf{r}), velocity (\mathbf{v}), and angular momentum (\mathbf{h}) vectors as follows [53]:

$$\mathbf{h} = \mathbf{r} \times \mathbf{v} \quad (2.10)$$

$$\mathbf{e} = \frac{\mathbf{v} \times \mathbf{h}}{\mu} - \frac{\mathbf{r}}{r} \quad (2.11)$$

where,

$$\mathbf{h} = \begin{bmatrix} h_x & h_y & h_z \end{bmatrix}^T \quad (2.12)$$

$$\mathbf{e} = \begin{bmatrix} e_x & e_y & e_z \end{bmatrix}^T \quad (2.13)$$

Orbital inclination (i) and RAAN (Ω) describe the angular orientation of the orbital plane with respect to the ECI frame (previously discussed in Section 2.1.1). Orbital inclination (i) represents the angular tilt of the orbital plane, measured from the K -axis unit vector (\hat{K}) of the ECI frame to the orbital angular momentum vector. Inclination ranges from $0^\circ < i < 180^\circ$ and is calculated as follows [53,54]:

$$i = \cos^{-1} \left(\frac{h_K}{h} \right), \quad i \in [0^\circ, 180^\circ] \quad (2.14)$$

where,

$$h = |\mathbf{h}| = \sqrt{h_I^2 + h_J^2 + h_K^2} \quad (2.15)$$

RAAN (Ω) is the angle between the I -axis unit vector (\hat{I}) of the ECI frame and the ascending node. The ascending node lies on the line of nodes and is the point at which the orbit crosses from the Southern to the Northern hemispheres of the Earth. The line of nodes can be represented in vector notation as, \vec{n} , and can be derived through the following cross product: $\vec{n} = \hat{K} \times \vec{h}$. For equatorial orbits, RAAN is undefined, as there are no nodes ($\vec{n} = 0$). The measurement direction comes from the Right-Hand-Rule

convention viewed from above the North Pole [53]. For all orbits, $0^\circ < \Omega < 360^\circ$ in the I - J plane of the ECI frame. The value of RAAN is dependant on the I -component of the angular momentum vector, and is calculated as follows [53]:

$$\Omega = \tan^{-1} \left(\frac{h_I}{-h_J} \right) = \begin{cases} 0 \leq \Omega \leq 180^\circ, & \text{if } h_I > 0 \\ 180^\circ \leq \Omega \leq 360^\circ, & \text{if } h_I < 0 \end{cases} \quad (2.16)$$

The argument of perigee (ω) describes the angular location of the orbital perigee, and is measured from the ascending node. The perigee (r_p) is the shortest radius of the orbit from the focus (often Earth's centre) to the orbital perimeter. For all orbits, $0^\circ < \omega < 360^\circ$, except for circular or equatorial orbits, as no perigee and no node exist. The argument of perigee is dependant on the K -component of the eccentricity vector and is generally calculated as follows [53]:

$$\omega = \cos^{-1} \frac{e_x \cos \Omega + e_y \sin \Omega}{e} = \begin{cases} 0 < \omega < 180^\circ, & \text{if } e_K \geq 0 \\ 180^\circ < \omega < 360^\circ, & \text{if } e_K < 0 \end{cases} \quad (2.17)$$

$$e = |\mathbf{e}| = \sqrt{e_I^2 + e_J^2 + e_K^2} \quad (2.18)$$

The true anomaly (ν) describes the position of the spacecraft in an orbit at a point in time, and is the relational component from orbital geometry and position to time. It is measured in relation to the perigee, and varies $0^\circ < \nu < 360^\circ$ over the orbital period. For circular orbits, ν is undefined, as there is no perigee. The true anomaly is dependant on the dot product of the position and velocity vectors, and is calculated as follows [53]:

$$\nu = \cos^{-1} \frac{\mathbf{e} \cdot \mathbf{r}}{er} = \begin{cases} 0 < \nu < 180^\circ, & \text{if } \mathbf{r} \cdot \mathbf{v} > 0 \\ 180^\circ < \nu < 360^\circ, & \text{if } \mathbf{r} \cdot \mathbf{v} < 0 \end{cases} \quad (2.19)$$

Note that the $|\dots|$ notation indicates the L_2 norm to be computed as: $|\dots| = \sqrt{x^2 + y^2 + z^2}$ for the respective vector components in the respective frame, where x , y , z are placeholder components of the respective vector.

2.2 Orbital Propagator Tests and Validation

This section showcases results to validate the propagator process discussed in this chapter, which in turn, validates the method used in constructing the sample data for analysis by the filter, as well as the governing equations of motion to be used for the filter. Figure 2.3 shows an original orbit (Orbit 1) of a spacecraft that has undergone a maneuver at the apogee and is now in the new orbit (Orbit 2). The axes correspond to the I - (x_1) and J - (x_2) directions. A circle for the Earth and a point for the orbital focus (centre of the Earth) are included for reference. This result demonstrates an example that the propagator functions as desired and expected. The initial and final orbital elements and orbital energy associated with the maneuvering case in this example are provided in Table 2.1 for reference.

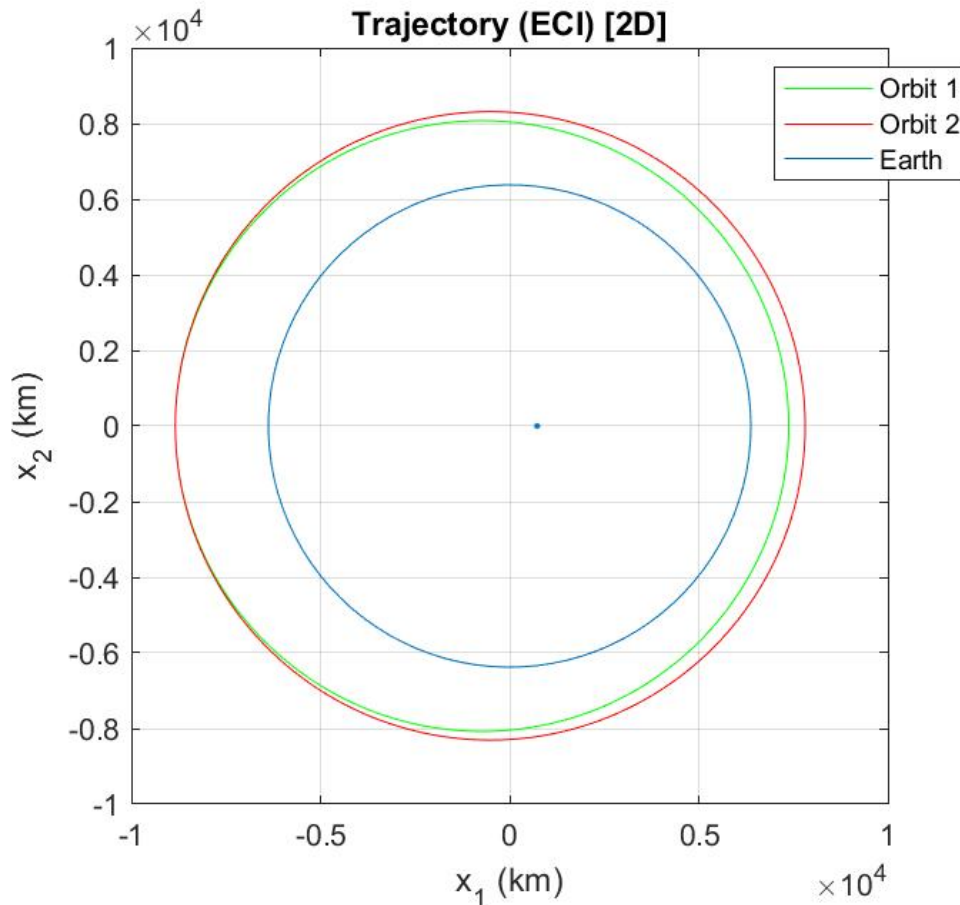


Figure 2.3: Example spacecraft maneuver affect on 2D orbital geometry for $\Delta v = 100$ m/s in the transverse direction applied at the orbital apogee).

For further validation, Figure 2.4 displays the orbital energy over the full simulation, including the maneuver. As shown in the image, there is an increase in orbital energy due to the applied maneuver. Both before maneuver onset and after maneuver completion, the orbital energy is constant, as expected. Since the orbital energy results follow expected trends, this validates the propagator and its process. The initial and final orbital elements and orbital energy associated with the maneuvering case in this example are also provided in Table 2.1 for reference.

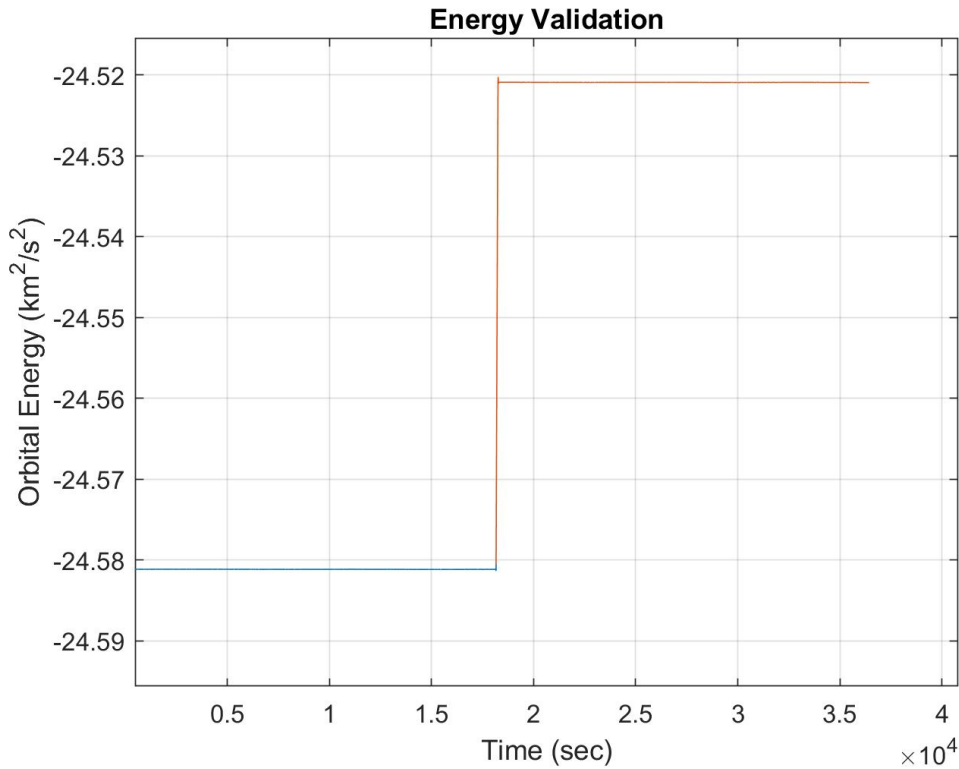


Figure 2.4: Orbital energy plot over full simulation time for propagator validation of $\Delta v = 10$ m/s in the transverse direction applied at the orbital apogee.

Table 2.1: Initial and Final Orbital Elements and Orbital Energy for Validation Cases

	Δv (m/s)	a (km)	e	i (°)	Ω (°)	ω (°)	ν (°)	ϵ (km ² /s ²)
Initial	—	8 107.84	0.090	0	0	0	0	-24.58
Final (Figure 2.3)	100	8 325.33	0.062	0	0	0.520	33.51	-23.94
Final (Figure 2.4)	10	8 127.75	0.087	0	0	0.029	1.944	-24.52

CHAPTER 3

Filtering and Detection

3.1 Filtering Methods

As discussed in Chapter 1, filters are a popular method for the detection of unknown maneuvers. Possibilities include different kinds of Kalman Filtering, batch filters, and others. Here, the focus is on using Kalman Filtering, as a widely used and accepted filtering method [57]. However, since the primary function of a filter is to separate and discard noise from data measurements, a filter will not necessarily detect the occurrence of a maneuver automatically. Thus, along with a filtering method, a maneuver detection and characterisation method is required. As previously discussed (see Section 1.2.2), some methods include the use of Thrust-Fourier-Coefficients (TFCs) for event representation [41], Root Mean Square Error (RMSE) and model probability [39], or a specified covariance-based detection parameter [41]. Since the goal is to maintain simplicity in the algorithm for decreasing computational needs, the use of a detection parameter is desirable and explored further in this section.

3.1.1 Kalman Filtering Overview

The Kalman Filter (KF) and its modified versions are popular filtering systems for several dynamical systems and tracking problems [57, 58]. The KF is a base popular technique used for linear systems. Modifications such as the Extended Kalman Filter (EKF), Unscented Kalman Filter (UKF), or Cubature-Kalman Filter (CKF) allow for the filtering of nonlinear systems. Since spacecraft follow nonlinear dynamical systems, these modified versions of the KF are often utilised. Kalman-based filtering techniques have been widely known and used since the 1960's for filtering noise from measurements and predicting state dynamics [57, 58].

The Kalman Filter is a solution to the Linear-Quadratic Problem (LQP), as a sequential optimal estimator, to estimate the instantaneous state of a system, involving uncertainty and noise [57, 58]. The KF is widely used as it does not require as much computational management as other techniques, nor any specific or unrealistic assumptions [59]. Additionally, the KF allows for inference of missing or unavailable

information from noisy and indirect measurements; can be used for prediction and estimation purposes of dynamical systems [57]; and, can combine measurements of multiple different sensors [40]. With estimation, the KF is able to handle systems that include some random behaviours by using statistical information [57].

The Extended Kalman Filter (EKF) was developed for handling nonlinear systems, and became another popular filter, that is still widely used and accepted [57, 58]. The EKF was even used for a space navigation problem in the Apollo missions to travel to the Moon and back [57]. Though the linearisation process in the EKF can induce errors causing divergence, the process is still robust, and a continued popular choice for use [57]. Partial derivatives as linear approximations of the nonlinear dynamical relations are used in the EKF approach, which accomplish the linearisation objective of the filter [57]. The EKF updates the state trajectory estimate at each time iteration reducing divergence encountered by the linear KF [53].

The Unscented Kalman Filter (UKF) was next developed for nonlinear estimation. It incorporates the higher order system statics in order to avoid the EKF linearisation process by utilising sample point sets, and is capable of estimating the associated quaternions of spacecraft attitude [58]. The UKF makes use of the Unscented Transform (UT), a sigma-point sampling method for propagating state means and covariances of nonlinear systems [57]. Samples are selected and weighted by the UT based on the state estimate, ($\hat{\mathbf{x}}$), and state covariance matrix, (\mathbf{P}) [57].

More recently, the Cubature Kalman Filter (CKF) was developed for high-dimensional state estimation [60]. The main feature of the CKF is the third-degree spherical-radial cubature rule, which allows for multivariate moment integrals passed to the filter to be computed [60]. A square-root version of the CKF was also developed by Arasaratnam and Haykin to improve numerical stability [60]. Modifications and variations to the CKF are still being developed by Jia et al. with promising results [39, 40].

3.1.2 Extended Kalman Filter

As a widely accepted filtering technique, the EKF is a useful option for the spacecraft maneuvering detection and characterisation problem. The EKF follows a sequential process for estimating, updating, and propagating state dynamics [41, 57]. A reference trajectory is used in the EKF to predict and update state estimates, which is also updated at each time step [53]. The advantages of the EKF are well documented as listed in [53]. Thus, this section walks through the EKF process, as based on the algorithm presented by Goff et al. [41], and with background reference to [53].

The EKF is generally governed by two main equations [39,41]:

$$\mathbf{x} = \mathbf{f}(\mathbf{x}, t) + \mathbf{v} \quad (3.1)$$

$$\mathbf{y} = \mathbf{h}(\mathbf{x}, t) + \mathbf{w} \quad (3.2)$$

where, \mathbf{x} = State vector,

$\mathbf{f}(\mathbf{x}, t)$ = Nonlinear state dynamics relationship (Equations (2.5) and (2.6)),

\mathbf{v} = Process noise,

\mathbf{y} = Observations of the state,

$\mathbf{h}(\mathbf{x}, t)$ = Nonlinear relationship of observations to the state,

\mathbf{w} = Observation noise.

To begin the process, state dynamics must first be defined, including a state estimate, ($\hat{\mathbf{X}}$), and a state covariance matrix estimate, ($\hat{\mathbf{P}}$) [41,57]. The state estimate is, again, based on Equations (2.5) and (2.6), where the components are listed in the form of positions and velocities of the spacecraft. The state covariance matrix captures the estimation uncertainty of the states [57], and is often of diagonal matrix form. In order to gain a state covariance estimation from the filter, the State Transition Matrix (STM; Φ) is used. The STM is an evolution operator for dynamical systems [57] that maps the state from one time to the next. It is a Jacobian matrix, can be defined as follows [41,53]:

$$\Phi(t, t_0) = \frac{\partial F(\mathbf{X}, t)}{\partial \mathbf{X}} = \begin{bmatrix} \mathbf{0} & \mathbf{I} \\ \Lambda & \mathbf{0} \end{bmatrix} \quad (3.3)$$

$$\Lambda = \begin{bmatrix} -\frac{\mu}{r^3} + 3\mu\frac{r_1^2}{r^5} & 3\mu\frac{r_1r_2}{r^5} & 3\mu\frac{r_1r_3}{r^5} \\ 3\mu\frac{r_1r_2}{r^5} & -\frac{\mu}{r^3} + 3\mu\frac{r_2^2}{r^5} & 3\mu\frac{r_2r_3}{r^5} \\ 3\mu\frac{r_1r_3}{r^5} & 3\mu\frac{r_3r_2}{r^5} & -\frac{\mu}{r^3} + 3\mu\frac{r_3^2}{r^5} \end{bmatrix}$$

where, μ and r are defined in Section 2.1.3, and $F(\mathbf{X}, t)$ is defined in Section 2.1.1. The STM can then be differentiated to form the following relationship [53]:

$$\dot{\Phi}(t, t_0) = \left(\frac{\partial F(\mathbf{X}, t)}{\partial \mathbf{X}} \right) \Phi(t, t_0) \quad (3.4)$$

When the time interval is zero, the STM is equal to the identity matrix ($\Phi(t_0, t_0) = \mathbf{I}$) and is used as an initial condition to Equation (3.4). The state covariance estimation also relies on the process noise, represented by the Process Noise Covariance Matrix (\mathbf{Q}), which captures error in the propagation of \mathbf{P} through time [53], and is also often of

diagonal form. Thus, the state covariance matrix can be predicted through the following relationship [41,53]:

$$\bar{\mathbf{P}} = \Phi(t, t_0)\hat{\mathbf{P}}\Phi(t, t_0)^T + \mathbf{Q} \quad (3.5)$$

The state prediction ($\bar{\mathbf{X}}$) is the result of integrating Equation (2.6).

Next, the state and state covariance matrix must be updated with observational information provided by the sensors. Observations from sensors can consist of position and velocity data, but more often consist of range, azimuth, elevation, and range-rate data. Note that sensors often operate in $\vec{\mathcal{F}}_{SEZ}$ and $\vec{\mathcal{F}}_{ECF}$ [41,53], which are discussed further in Section 3.2. By using this types of observation set (\mathbf{y}), another matrix relationship of partial derivatives is utilised, called the observation partials matrix or measurement sensitivity matrix (\mathbf{H}), which captures the affect of the changes in the state the observations [41,53,57]:

$$\mathbf{H} = \left(\frac{\partial \hat{\mathbf{y}}}{\partial \mathbf{X}} \right) = \left(\frac{\partial \mathbf{G}(\bar{\mathbf{X}}, t)}{\partial \mathbf{X}} \right) \quad (3.6)$$

where, $\hat{\mathbf{y}}$ represents the calculated observations by $\mathbf{G}(\mathbf{X}, t)$, which maps the predicted state to the observation set and creates a predicted observation set ($\hat{\mathbf{y}}$) [41]. The details of $\mathbf{G}(\mathbf{X}, t)$, and subsequently \mathbf{H} , are further explained in Section 3.2. With the observation mapping matrix, the residuals (ν_e) that the EKF works to minimise can be calculated [41]:

$$\begin{aligned} \nu_e &= \mathbf{y} - \mathbf{G}(\bar{\mathbf{X}}, t) \\ &= \mathbf{y} - \hat{\mathbf{y}} \end{aligned} \quad (3.7)$$

From the observation partials matrix, the observation covariance matrix, which is dependent on both the predicted state covariance and the measurement noise matrix, can be calculated [41]:

$$\mathbf{S} = \mathbf{H}\bar{\mathbf{P}}\mathbf{H}^T + \mathbf{R} \quad (3.8)$$

where, \mathbf{R} is the measurement noise covariance matrix, which captures noise created in the observation measurements made by the sensors, and is often of diagonal matrix form. With the observation covariance matrix, the Kalman gain matrix is calculated [41,53,57]:

$$\mathbf{K} = \bar{\mathbf{P}}\mathbf{H}^T(\mathbf{S})^{-1} \quad (3.9)$$

which, is a defining feature of KFs, and is a partial result of solving the matrix Riccati equation [57]. Together, the Kalman gain and residuals are used in calculating the state and state covariance matrix estimates, using the state and state covariance predictions, respectively, as follows [41,57]:

$$\hat{\mathbf{X}} = \bar{\mathbf{X}} + \mathbf{K}\nu_e \quad (3.10)$$

$$\hat{\mathbf{P}} = (\mathbf{I} - \mathbf{K}\mathbf{H})\bar{\mathbf{P}} \quad (3.11)$$

Finally, the filter has predicted and updated the state and state covariance matrix at the current time step. The filter can then process through the next time step, starting at the beginning again (Equations (2.6) and (3.4)), using the newly estimated data, and reading in the next observational data set.

3.2 Reference Frames and Observation Conversions

Following the three references frames discussed in Section 2.1.1, two additional frames are needed for use with the filter to take into account the positioning of sensors used in observing the maneuvering spacecraft. These two additional frames are the Earth-Centered-Earth-Fixed (ECEF; $\vec{\mathcal{F}}_{ECF}$) and the Topocentric Horizon or South-East-Zenith (SEZ; $\vec{\mathcal{F}}_{SEZ}$) frames [41,53]. These two extra frames are illustrated in Figure 3.1.

The ECEF frame ($\vec{\mathcal{F}}_{ECF}$) is generally used for processing accelerations and observation calculations [53]. This frame is fixed to the Earth, with the origin placed at the centre of the Earth, rotating with the Earth [53]. The E -axis points to the zero-longitude location of the Earth, along the equator (where $\lambda = 0$). The F -axis is aligned with Earth's axis of rotation (through the North Pole), and the C -axis completes the triad. This system is not fixed in space, and thus, also moves with the Earth [53].

The Topocentric Horizon frame ($\vec{\mathcal{F}}_{SEZ}$) is often used for sensor systems, and is another Earth-based system. The origin of the system lies at the sensor location on the surface of the Earth, and the frame rotates with the Earth. The location of the sensor is described by the geodetic latitude (ϕ_{gd}) and longitude (λ), which can be found on a map [53]. The S -axis points towards the South from the sensor location; the E -axis points towards the East from the site location and is undefined when the site is located at the North or South Poles; the Z -axis completes the triad, pointing outwards normal to the site [53]. The orientation of the system is defined by the Local Sidereal Time (LST; θ_{LST}), which is an angle measured from the Vernal Equinox (I -axis of $\vec{\mathcal{F}}_{ECI}$) to the local longitude of the site location, and fixes the system to a location [53]. The SEZ frame

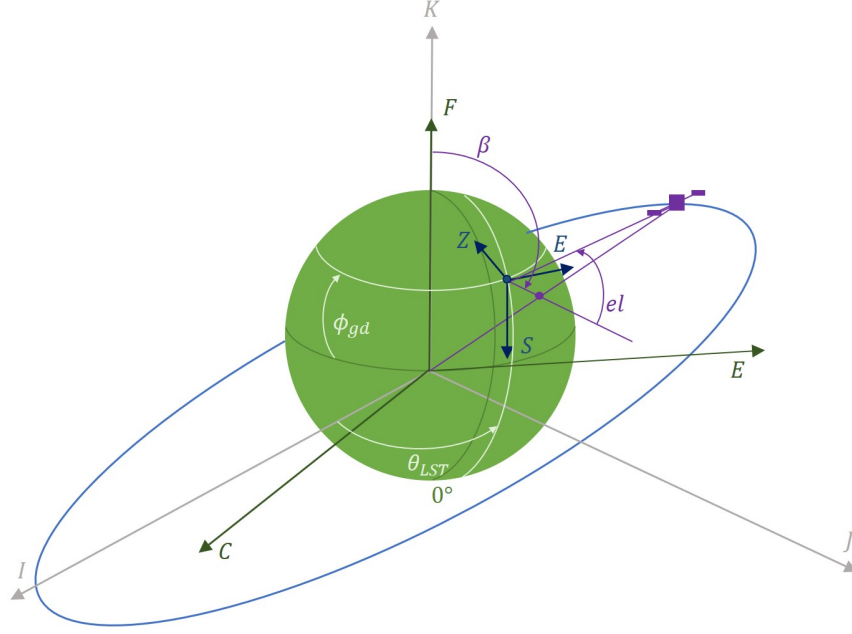


Figure 3.1: Diagram of Reference Frames for observations to be input to the filtering algorithm based on [53] for handling observational data; Earth-Centred-Earth-Fixed (ECEF; $\vec{\mathcal{F}}_{ECF}$), Topocentric Horizon/South-East-Zenith ($\vec{\mathcal{F}}_{SEZ}$).

incorporates viewing angles to describe the location of a satellite in relation to the sensor site. These angles are the azimuth (β) and elevation (el). Azimuth is measured clockwise from the North to the location of the satellite on the Earth's surface (beneath the satellite), and lies within the range of $0^\circ \leq \beta \leq 360^\circ$. Elevation is measured from the site local horizon upwards to the satellite, and lies within the range of $-90^\circ \leq el \leq 90^\circ$ [53].

Similarly to Section 2.1.1, the components in each frame can be transferred to other frames through rotation matrices (DCMs). When dealing with observations, additional components are necessary to complete the process, which include elliptical properties, site location, and Earth's constants. The site location in matrix form within the $\vec{\mathcal{F}}_{ECF}$ is defined as follows [53]:

$$\begin{aligned}
 C_E &= \frac{R_E}{\sqrt{1 - e_E^2 (\sin^2 \phi_{gd})}} \\
 S_E &= \frac{R_E (1 - e_E^2)}{\sqrt{1 - e_E^2 (\sin^2 \phi_{gd})}} \\
 \mathbf{r}_{site_{ECF}} &= \begin{bmatrix} (C_E + h_{ellp}) \cos \phi_{gd} \cos \lambda \\ (C_E + h_{ellp}) \cos \phi_{gd} \sin \lambda \\ (S_E + h_{ellp}) \sin \phi_{gd} \end{bmatrix} \quad (3.12)
 \end{aligned}$$

where, C_E, S_E = Auxiliary quantities obtained from geometric elliptical properties [53],
 R_E = 6378.137 km, Earth's Radius,
 e_E = 0.081819221456, Earth's surface eccentricity,
 ω_E = 7.292115×10^{-5} Rad/s, Earth's rotation speed,
 ϕ_{gd} = Geodetic Latitude of the site,
 λ = Site Longitude,
 h_{ellp} = Height above ellipsoid reference.

Note that the definition of h_{ellp} is similar to that of the height above Mean Sea Level (MSL), and further details can be found in the textbook of [53].

From the above site matrix definition, the observation vector in $\vec{\mathcal{F}}_{ECF}$ can also be defined [41,53]:

$$\rho_{\mathbf{F}}(\mathbf{r}_{sat}, \mathbf{v}_{sat}) = \begin{bmatrix} \mathbf{r}_{sat} - \mathbf{r}_{site} \\ \mathbf{v}_{sat} \end{bmatrix} \quad (3.13)$$

where, $\mathbf{r}_{sat}, \mathbf{v}_{sat}$ = satellite state components,

\mathbf{r}_{site} = site location matrix within the $\vec{\mathcal{F}}_{ECF}$ as defined in Equation (3.12).

In order to rotate components from the ECI frame to the ECEF frame ($\vec{\mathcal{F}}_{ECI} \rightarrow \vec{\mathcal{F}}_{ECF}$), the \mathbf{C}_1 matrix defined in Equation (2.1) can be used. The argument for this rotation is known as the Greenwich Mean Time (GMT) which is a combination of Earth's rotational speed and the present time (t) since the initial start time (t_0) [61]. Thus, this DCM is time-dependant and defined as follows [53,61]:

$$\theta_{GMT} = \omega_E(t - t_0)$$

$$\mathbf{C}_{\mathbf{FI}} = \mathbf{C}_1(\theta_{GMT})$$

Since observation partials will be needed in the filter, this time-dependant DCM will need to be differentiated into its derivative form [53]:

$$\dot{\mathbf{C}}_{\mathbf{FI}} = \begin{bmatrix} -\sin(\theta_{GMT}) & \cos(\theta_{GMT}) & 0 \\ -\cos(\theta_{GMT}) & -\sin(\theta_{GMT}) & 0 \\ 0 & 0 & 0 \end{bmatrix} \quad (3.14)$$

For the rotation from the ECEF frame to the SEZ frame ($\vec{\mathcal{F}}_{ECF} \rightarrow \vec{\mathcal{F}}_{SEZ}$), the DCM is a combination of the \mathbf{C}_2 and \mathbf{C}_3 matrices defined in Equation (2.1). The arguments are based on the longitude and latitude of the site location, and the matrix is defined as follows [53]:

$$\mathbf{C}_{\text{SF}} = \begin{bmatrix} \sin(\phi_{gd}) \cos(\lambda) & \sin(\phi_{gd}) \sin(\lambda) & -\cos(\phi_{gd}) \\ -\sin(\lambda) & \cos(\lambda) & 0 \\ \cos(\phi_{gd}) \cos(\lambda) & \cos(\phi_{gd}) \sin(\lambda) & \sin(\phi_{gd}) \end{bmatrix} \quad (3.15)$$

In Section 2.1.1, it was discussed that the satellite description would be a six-element set consisting of position and velocity vectors. This set would be equally split as 3 position components and 3 velocity components. However, observations are often made in a 4-element set consisting of range (distance from the site to the object), azimuth, elevation, and range rate. Thus, there are: one distance, one velocity, and two viewing angles involved. This means not only are rotation matrices necessary for filtering, but a method for converting the usual 6-element set to the practical 4-element observational set type is also necessary.

First, the predicted state directly post integration is converted from the ECI frame to ECEF ($\vec{\mathcal{F}}_{IJK} \rightarrow \vec{\mathcal{F}}_{ECF}$). Since the set contains velocity terms, the differentiated form of the respective DCM is used (Equation (3.14)), which is time-dependent [41, 53]:

$$\bar{\mathbf{X}}_{\text{F}} = \begin{bmatrix} \mathbf{C}_{\text{FI}}(t) & \mathbf{0} \\ \dot{\mathbf{C}}_{\text{FI}}(t) & \mathbf{C}_{\text{FI}}(t) \end{bmatrix} \bar{\mathbf{X}}_{\text{I}} \quad (3.16)$$

This becomes the satellite information to be used in Equation (3.13), which can then be rotated from ECEF to SEZ ($\vec{\mathcal{F}}_{ECF} \rightarrow \vec{\mathcal{F}}_{SEZ}$) using Equation (3.15) as follows [41, 53]:

$$\boldsymbol{\rho}_{\text{S}} = \begin{bmatrix} \mathbf{C}_{\text{SF}} & \mathbf{0} \\ \mathbf{0} & \mathbf{C}_{\text{SF}} \end{bmatrix} \boldsymbol{\rho}_{\text{F}} \quad (3.17)$$

where, the first three components can be considered range terms and the last three can be considered range rate terms (i.e. $\boldsymbol{\rho}_{\text{S}} = [\rho_{\text{S}} \ \rho_{\text{E}} \ \rho_{\text{Z}} \ \dot{\rho}_{\text{S}} \ \dot{\rho}_{\text{E}} \ \dot{\rho}_{\text{Z}}]^{\text{T}}$). From this, the following components can be defined at each time step [41, 53]:

$$\rho = |\boldsymbol{\rho}| = \left(\sqrt{\rho_{\text{S}}^2 + \rho_{\text{E}}^2 + \rho_{\text{Z}}^2} \right) \quad (3.18)$$

$$\beta = \tan^{-1} \left(\frac{-\rho_{\text{S}}}{\rho_{\text{E}}} \right) \quad (3.19)$$

$$el = \sin^{-1} \left(\frac{\rho_{\text{Z}}}{\rho} \right) \quad (3.20)$$

$$\varpi = (\boldsymbol{\rho} \cdot \dot{\boldsymbol{\rho}}) \quad (3.21)$$

where, $\boldsymbol{\rho}$, ρ = Calculated observation range vector and magnitude, respectively,
 $\dot{\boldsymbol{\rho}}$ = Calculated observation range rate vector,
 β , el = Viewing angles: Azimuth (Rad) and Elevation (Rad), respectively,
 ϖ = Dot product of the range vector by the range rate vector.

Finally, the calculated observation matrix can be assembled [41, 53]:

$$\hat{\mathbf{y}} = \left[\rho \quad \beta \quad el \quad \frac{\varpi}{\rho} \right]^T \quad (3.22)$$

which is used in Equation (3.7).

Now, the H-partials (\mathbf{H}) and mapping ($\mathbf{G}(\bar{\mathbf{X}}, t)$) matrices mentioned in Section 3.1.2 (Equation (3.6)) can be introduced and defined in detail as follows [41, 53]:

$$\mathbf{H} = \frac{\partial \hat{\mathbf{y}}}{\partial \boldsymbol{\rho}_S} \frac{\partial \boldsymbol{\rho}_S}{\partial \boldsymbol{\rho}_F} \frac{\partial \boldsymbol{\rho}_F}{\partial \mathbf{X}_F} \frac{\partial \mathbf{X}_F}{\partial \mathbf{X}_I} = \frac{\partial \mathbf{G}(\bar{\mathbf{X}}, t)}{\partial \bar{\mathbf{X}}} \quad (3.23)$$

which are defined piece by piece per the following [41, 53]:

$$\begin{aligned} \frac{\partial \mathbf{X}_F}{\partial \mathbf{X}_I} &= \begin{bmatrix} \mathbf{C}_{FI}(t) & \mathbf{0} \\ \dot{\mathbf{C}}_{FI}(t) & \mathbf{C}_{FI}(t) \end{bmatrix} \\ \frac{\partial \boldsymbol{\rho}_F}{\partial \mathbf{X}_F} &= \mathbf{I} \\ \frac{\partial \boldsymbol{\rho}_S}{\partial \boldsymbol{\rho}_F} &= \begin{bmatrix} \mathbf{C}_{SF} & \mathbf{0} \\ \dot{\mathbf{C}}_{SF} & \mathbf{C}_{SF} \end{bmatrix} \\ \Upsilon &= \begin{bmatrix} \frac{\rho_S}{\rho} & \frac{\rho_E}{\rho} & \frac{\rho_Z}{\rho} \\ \frac{\rho_E}{\rho_E^2 + \rho_S^2} & -\frac{\rho_S}{\rho_E^2 + \rho_S^2} & 0 \\ -\frac{\rho_S \rho_Z}{\rho^2 \sqrt{\rho^2 - \rho_Z^2}} & -\frac{\rho_E \rho_S}{\rho^2 \sqrt{\rho^2 - \rho_Z^2}} & \frac{\sqrt{\rho^2 - \rho_S^2}}{\rho^2} \\ \frac{\dot{\rho}_S}{\rho} - \frac{\rho_S \varpi}{\rho^3} & \frac{\dot{\rho}_E}{\rho} - \frac{\rho_E \varpi}{\rho^3} & \frac{\dot{\rho}_Z}{\rho} - \frac{\rho_Z \varpi}{\rho^3} \end{bmatrix} \\ \Omega &= \begin{bmatrix} 0 & 0 & 0 \\ 0 & 0 & 0 \\ 0 & 0 & 0 \\ \frac{\rho_S}{\rho} & \frac{\rho_E}{\rho} & \frac{\rho_Z}{\rho} \end{bmatrix} \\ \frac{\partial \hat{\mathbf{y}}}{\partial \boldsymbol{\rho}_S} &= \left[\Upsilon \quad \Omega \right] \end{aligned}$$

3.3 Detection Parameter Amendments, Improvements, and Preliminary Results

The main desirable aspect of the Goff et al. [41] study is the weighted maneuver detection parameter, Ψ , based on the filter residuals and observation covariance estimated by the EKF (outlined in Section 3.1.2). The Ψ parameter is then used as an indicator to initiate a covariance inflation option based on a specified threshold value. This particular inflation process prevents filter divergence, allowing for a converged maneuver detection solution output in real-time [41]. Since Goff et al. [41] use an IMM process in conjunction with the EKF, another parameter, η , is used as a set of potential inflation limits per available model options, and is used as a secondary initiation of covariance inflation based on the trace of the filter-estimated state covariance matrix ($\hat{\mathbf{P}}$). For the purposes of simplicity, since the IMM is not to be used in this dissertation, the η parameter acts as a constant set state covariance trace threshold for the secondary initiation. In addition, the process noise covariance matrix (\mathbf{Q}) is updated to utilise the calculated Ψ -value at each time step. Thus, the following steps are appended to the EKF based on [41] and modified:

1. Calculation of Ψ after residuals Observation Covariance computation:

$$\Psi = \boldsymbol{\nu}_e^T (\mathbf{S})^{-1} \boldsymbol{\nu}_e \quad (3.24)$$

2. Application of Inflation Process:

$$\Psi > \Psi_{th} \rightarrow \text{Inflation check: } \text{tr}(\hat{\mathbf{P}}) < \eta_{th} \rightarrow \hat{\mathbf{P}} = 10 \hat{\mathbf{P}}$$

where, Ψ_{th} = The set threshold detection parameter,

Ψ = The detection parameter,

$\text{tr}(\cdot)$ = The matrix trace computation,

η_{th} = The set state covariance inflation threshold,

$\hat{\mathbf{P}}$ = The estimated State Covariance Matrix.

3. Process Noise Calculation:

$$\mathbf{Q} = \begin{bmatrix} q_r \mathbf{I} & \mathbf{0} \\ \mathbf{0} & q_v \mathbf{I} \end{bmatrix} \quad (3.25)$$

where, q_r, q_v = Scaling components for position and velocity, respectively,
and are defined in Table 3.1.

Once these steps are complete, the filter can go back to the first step with the new state covariance and state estimates as before, using the inflated covariance matrices.

Table 3.1: Values for Process Noise Covariance Inflation Based on Ψ (per [41])

	$0 \leq \Psi$	$10^5 \leq \Psi$	$5 \times 10^5 \leq \Psi$	$10^6 \leq \Psi$	$5 \times 10^6 \leq \Psi$	$10^7 \leq \Psi$	$5 \times 10^7 \leq \Psi$	$10^8 \leq \Psi$	$5 \times 10^8 \leq \Psi$
q_r	0	0.05	0.1	0.5	1	5	10	50	100
q_v	0	5×10^{-5}	1×10^{-4}	5×10^{-4}	1×10^{-3}	5×10^{-3}	0.01	0.05	0.1

3.3.1 Detection Parameter Improvements

As will be illustrated in Section 3.3.2, the previously established method by Goff et al. [41] is able to detect a maneuver, however, the detection is not always clear for all results over the full simulation time. To make the detection as clear and prominent as possible, the original Ψ parameter has been modified, as follows:

$$K = 20 \log_{10}(\Psi + 1) \quad (3.26)$$

This new parameter, K , adjusts the output to showcase and separate the maneuver occurrence from the rest of the data by utilising the base-10 logarithm. The logarithmic parameter definition allows for better handling of high orders of magnitudes in the original Ψ detection parameter, where a linear definition would not necessarily represent the parameter well. Since it is now on a decibel (dB) scale, the factor 20 amplifies the differences between the detection and the threshold, as conventional in control theory, acoustics, or communications [62]. Adding 1 to Ψ shifts all values, guaranteeing positive values at all times, and removes the noticeable undesirable anti-peaks shown in the preliminary results (see Figure 3.2a). This K -parameter is the new method of analysis and addition to the previously accepted methods for maneuver detection and characterisation. For analyses, a maneuver detection occurs when K is at a maximum ($K = K_{\max}$). These maximums can be accumulated over multiple simulations, and a relationship can be explored.

Another difference between K and Ψ is the timing of the implementation; Ψ is applied and used within the EKF algorithm, whereas K is applied after the EKF as a post processing procedure. Though Ψ was intended to be a real-time detection parameter, by placing K after the filtering process, it is possible that false detections could be minimised as only maximum K -values are analysed. This could be assistive to both operators and smaller operating companies, where real-time calculations may be too costly in terms of computational resources.

3.3.2 Preliminary Maneuver Detection Results

Figures 3.2 to 3.4 showcase the capability of both the Ψ -parameter maneuver detection method per Goff et al. [41] and of the K-parameter developed in this research, as an example and for comparison. Figures 3.2 and 3.4a show Ψ and K over the full simulation with an impulsive maneuver of $\Delta v = 5$ m/s applied at apogee in the radial direction, while Figures 3.3 and 3.4b show the results for a $\Delta v = 25$ m/s applied at perigee in the transverse direction. For Figures 3.2 and 3.3, results are plotted using two different scales: 1) Logarithmic, as per the results presented in Goff et al. [41]; and, 2) Linear, as a way to showcase the results in another fashion. The horizontal dashed lines in all figures represent the set threshold values, where $K_{th} = 20 \log_{10}(\Psi_{th=30} + 1)$. The vertical dashed lines represent the times of the applied maneuver. Though it is not visible in these plots, there are actually two vertical dashed lines plotted to represent the maneuvering onset and completion times, respectively.

The orbit for these results was set with an eccentricity of 0.09, an initial spacecraft altitude of 1000 km (which is also the perigee altitude), an initial true anomaly of 0° , and an inclination, RAAN and ω of 0° . The impulsive maneuver was applied after 2 full orbits, in the radial direction at the apogee. The total simulation time was over 5 full orbits of the initial orbital period plus the maneuvering time of $t_{man} = 100$ seconds. The detection threshold was set at $\Psi_{th} = 30$ ($\therefore K_{th} \approx 30$), with a state covariance trace threshold of $\eta_{th} = 1$ [41]. The covariance matrices were set as:

$$\mathbf{R} = \text{diag}\left(\left[\begin{array}{cccccc} (5 \times 10^{-3})^2 & 0.02^2 & 0.02^2 & (0.5 \times 10^{-3})^2 & & \end{array} \right]\right)$$

$$\hat{\mathbf{P}}_0 = \text{diag}\left(\left[\begin{array}{cccccc} 1 \times 10^{-4} & 1 \times 10^{-4} & 1 \times 10^{-4} & 1 \times 10^{-6} & 1 \times 10^{-6} & 1 \times 10^{-6} \end{array} \right]\right)$$

$$\mathbf{Q}_0 = \text{diag}\left(\left[\begin{array}{cccccc} 1 \times 10^{-2} & 1 \times 10^{-2} & 1 \times 10^{-2} & 1 \times 10^{-5} & 1 \times 10^{-5} & 1 \times 10^{-5} \end{array} \right]\right)$$

where, $\hat{\mathbf{P}}_0$ is the initial state covariance matrix estimate and \mathbf{Q}_0 is the initial process noise covariance matrix for the filtering algorithm. Noise of zero-mean Gaussian property was added to the simulated observational data as per the provided \mathbf{R} measurement noise covariance matrix values per Goff et al. [41].

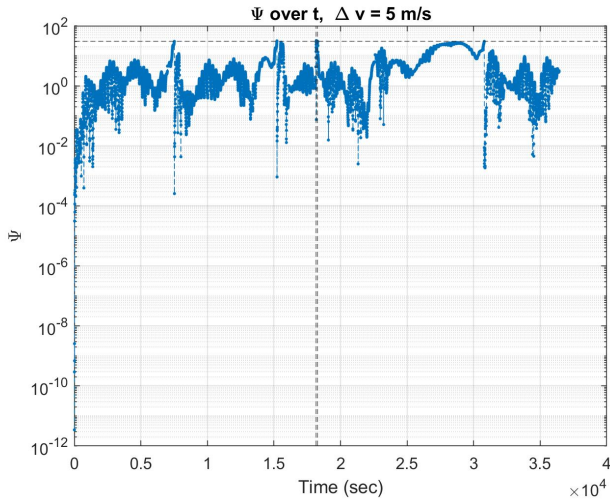
In Figures 3.2a and 3.3a, a small peak at the maneuver time is observable in both cases. However, the peaks are quite near the $\Psi_{th} = 30$ threshold and could be easily missed, at just $\Psi \approx 10^1$ for both cases. There are many low anti-peaks below the threshold, with very large anti-peaks near the beginning of the simulation at $\Psi \approx 10^{-12}$ in both cases.

In addition, the numbers achieved are quite large, causing a great variation in Ψ overall with a large range of $10^2 \leq \Psi \leq 10^{-12}$, reducing the clarity of a maneuver detection peak, especially for smaller magnitude maneuvers or maneuvers at perigee. In some cases, these ranges were even larger with possible ranges of up to $10^3 \leq \Psi \leq 10^{-23}$. On the linear scales, the detection is clearer, with $\Psi \approx 33$ and $\Psi \approx 34$, respectively. However, this could be improved.

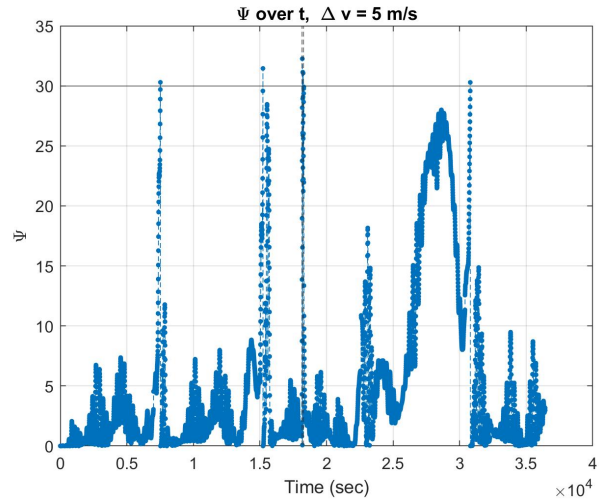
For Figures 3.4a and 3.4b, a prominent spike is visible at the maneuver time, with $K \approx 50$ and $K \approx 37$, respectively. There are no longer any undesired anti-peaks, with all values in the positive range. In addition, the scale is now more comprehensible than in the logarithmic scale, with a smaller range of $0 \leq K \leq 50$ and $0 \leq K \leq 37$, respectively. This shows an improvement from the original detection parameter, where the detection is clear and the range has increased in the positive scale to assist in clarifying a maneuver has taken place. This also shows that the new detection parameter may be robust for many scenarios, and alludes to the possibility of the characterisation of maneuvers and prediction of maneuver type through the development of possible relationships between K and Δv . It is important to note that, for some specific cases, the original Ψ parameter will show clearer detections, where Ψ will become large on the order of $\Psi \approx 10^3$.

It should also be noted that the K -parameter is denoted as κ for the y -axis labels for these figures (Figure 3.4). For discussion purposes, the two variables and notations are considered equivalent for this section. In subsequent sections, κ_{\max} is shown in figures for the y -axis labels, which is the maximum value of κ over the respective simulations, and is then also used interchangeably with K .

For further comparison, a base case for the filter and detection process has been included in Appendix B where no maneuvers have been applied. The result showcases a maximum at $t = 15\,400$ seconds with $K_{\max} = 30.127$ and $\Psi_{\max} = 31.089$. Thus, it can be expected that small maneuvers, where $\Delta v \approx 0$, will incur a detection parameter value of $K_{\max} \approx 30.127$ or $\Psi_{\max} \approx 31.089$, which sets the minimum possible and default output values for the detection parameters, and could result in false detections at these values.

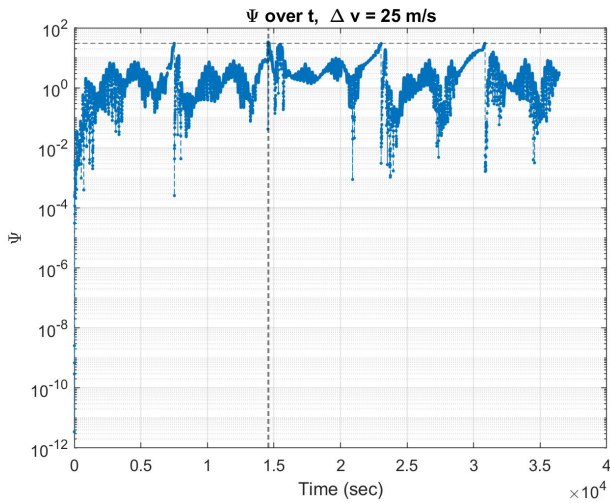


(a)

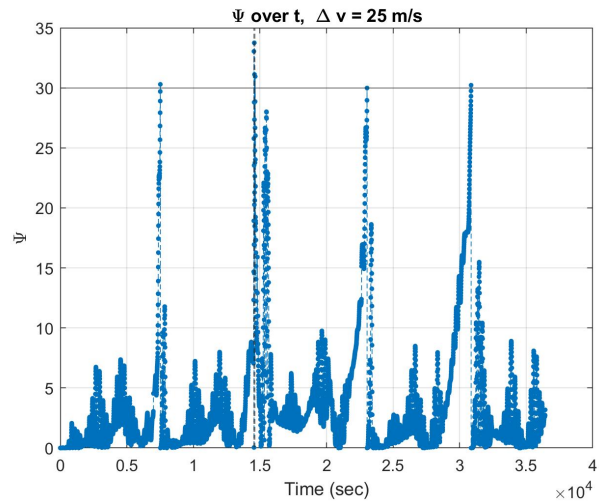


(b)

Figure 3.2: Ψ detection parameter vs. time results for an impulsive radial maneuver of $\Delta v = 5$ m/s applied at apogee, plotted on logarithmic (Figure 3.2a) and linear scales (Figure 3.2b).

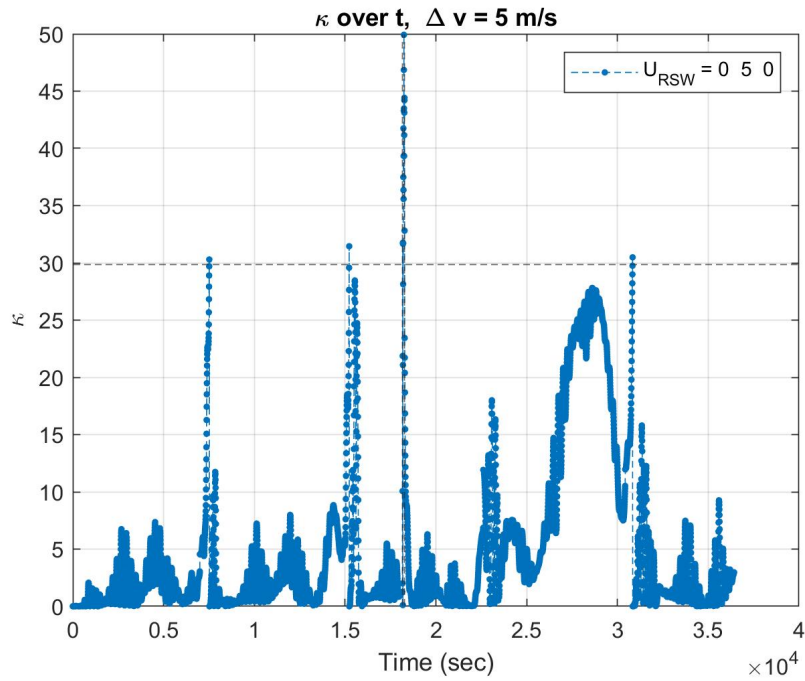


(a)

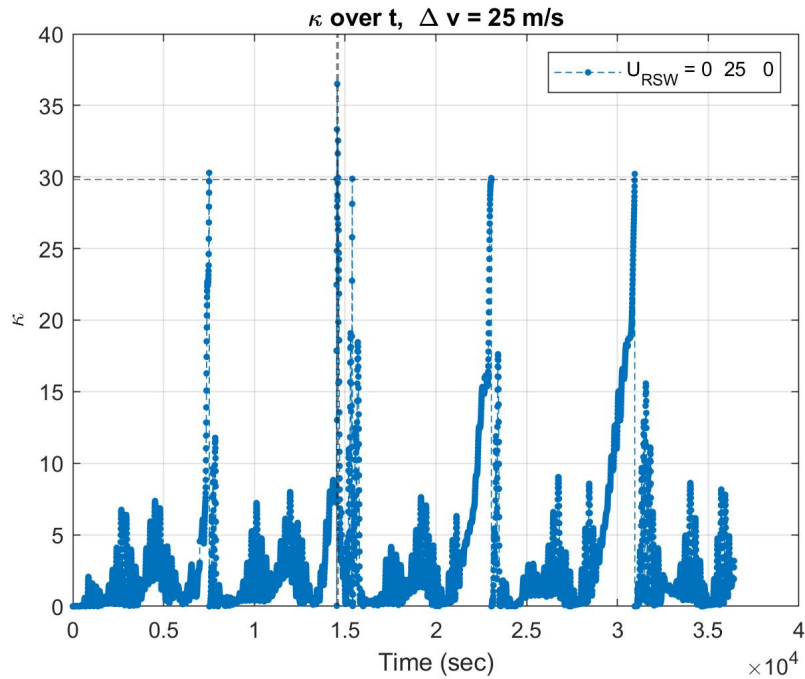


(b)

Figure 3.3: Ψ detection parameter vs. time results for an impulsive transverse maneuver of $\Delta v = 25$ m/s applied at perigee, plotted on logarithmic (Figure 3.3a) and linear scales (Figure 3.3b).



(a) Radial maneuver K vs. time for $\Delta v = 5$ m/s applied at apogee.



(b) Transverse maneuver K vs. time for $\Delta v = 25$ m/s applied at perigee.

Figure 3.4: Results for detection parameter K vs time for a radial impulsive maneuver of $\Delta v = 5$ m/s applied at apogee (Figure 3.4a), and transverse $\Delta v = 25$ m/s applied at perigee (Figure 3.4b).

CHAPTER 4

Maneuver Detection Results and Discussion

4.1 Simulation Setup

For all simulations, it is assumed that all cases can be modelled as 2-body problems (per Chapter 2), without other perturbations (i.e. natural events). Maneuvers are considered to be impulsive — a high magnitude thrust (implemented as a small constant acceleration, since mass is not considered, per Chapter 2) applied over a short time period. Orbital elements can, therefore, be considered constant over the thrust period (set as $t_{man} = 100$ seconds), and the Direct Cosine Matrices (DCMs) can be used at the initial orbit state prior to the maneuver. Only the time dependent DCMs used for filtering observations (Equations (3.14) and (3.15)) require updates at each time step. For all simulations, observation data is assumed to be taken from the Ascension, Atlantic ground station site location ($\phi_{gd} = -7.91^\circ$, $\lambda = -14.4^\circ$, $h_{ellp} = 56.1$ m [53]), with observations taken every 5 seconds, and omitted if the spacecraft is below 1° of elevation per sensor constraints [53]. The observation data was simulated per the propagator presented in Chapter 2, with added zero-mean Gaussian noise per the provided measurement noise covariance matrix in Chapter 3. The Extended Kalman Filter (EKF) technique with the amendments outlined in Chapter 3 was implemented. Though MATLAB has available KF algorithms, including an EKF protocol, the filtering technique was manually coded for simpler customisation and editing.

For the basis of cases, the settings are applied as shown in Section 3.3.2 with the listed Earth constants in Table 4.1 (per [53]). Test cases are simulated by varying the different parameters from Section 3.3.2 — e.g. orbital elements are varied to simulate maneuvering cases in different orbits. Several cases are tested to explore the capability of the new K-parameter, with attempts to find a relationship between K and the maneuvering Δv . The main tests of interest are: varying Δv both in magnitude and direction (Section 4.2.1); varying the maneuver orbital location (Section 4.2.2); and, varying the orbital geometry (Section 4.2.3). From these results, the goal is to find possible relationships between K and Δv per orbital location or maneuver direction. Some results are compared to some of the original results from Goff et al. [41], and other possible test cases are briefly discussed.

Table 4.1: Earth’s Constants Used in All Simulations [53]

R_E (km)	G (km ³ /kg·s ²)	M_E (kg)	μ_E (km ³ /s ²)
6378.137	6.673×10^{-20}	5.973×10^{24}	3.986×10^5

4.2 Detection Parameter Trends

Several case studies were simulated and analysed using simulated observation data as describe above. This section presents the relevant case results with corresponding discussions on how the new K detection parameter may relate to different maneuvering scenarios. Some comparison to the original Ψ -parameter is also provided. Tested scenarios include varied Δv magnitudes, Δv directions, maneuvering locations, orbital geometry and orientation, measurement noise covariance, detection parameter and state covariance inflation thresholds, and maneuver duration. A maneuver occurrence detection is deemed by observing a maximum in K at a certain time, such that $K = K_{\max}$ (denoted as κ_{\max} in all figures. These maximums are accumulated over multiple simulations and analysed (where Δv points are colour coded with red as the smallest and blue as the largest Δv for all figures). Results are discussed to make conclusions about the possible trends in the relationships between K and Δv with some reference and comparison to Ψ and Δv . Curves are fitted to find an approximate analytical relationship between the two parameters in both cases. Finding an analytical relationship between the two parameters, which is important for both maneuver characterisation and prediction purposes for operators. It is possible that different curve fit relationships could be best for different scenarios. The main scenarios of interest, however, are maneuvers applied at the orbital apogee in the transverse direction, and will be the focus for most subsections. A summary table of qualitative summaries for select cases can be found in Appendix C. Results for further cases can be found in Appendices D and E, including a short discussion on maneuver detection timing in Appendix F.

4.2.1 Variation of K with Δv Magnitude and Direction

In this first set of simulations, the impulsive maneuver magnitude, Δv , was varied discretely from 1 m/s to 100 m/s. Figures 4.1 to 4.3 show the variation in the new K detection parameter in relation to the tested Δv values. The K-parameter is denoted as κ_{\max} for the y -axis labels in all figures — as the maximum value was taken from each simulation (described above), which depicts a maneuver detection — and are used for creating the relationships. For discussion purposes, the two are considered equivalent, and the same is consistent for the remainder of this chapter.

For the maneuvers applied in the radial direction, the variation of K ranges from $30 < K < 90$ (Figure 4.1), which is similar in the transverse direction, at $30 < K < 85$ (Figure 4.2), and is smallest, at $30 < K < 45$ (Figure 4.3) for the maneuvers applied in the normal direction. These observations allude to a possible relationship between the ranges of K to Δv . Directional predictions of Δv could be made based on these ranges, where K falling within a certain range of values indicates a particular direction. For example, smaller K-values would be associated with normal maneuvers until $K = 45$, after which K-values indicate transverse maneuvers, where $K > 85$ would indicate radial maneuvers. This could be useful to operators for preliminary predictions. There is also an obvious general trend that as the maneuver velocity magnitude increases, the magnitude of K increases as well, though not necessarily proportionally, as anticipated.

To find an approximate analytical relationship, five curves were fitted to the results for each direction. The corresponding coefficients of the five fitted lines are tabulated in Table 4.2, where the y -variable represents the detection parameter, K, and the x -variable represents Δv . The correlation measures are showcased by the R^2 and R^2 -adjusted values tabulated in Table 4.3. Note that the x -values were not normalised, and thus, have units of Δv (m/s); the y -values follow the K-parameter, which is dimensionless.

To select potential curve fit relationships, the impact of applying an impulsive maneuver to the system must be analysed. Through inspection of the orbital energy equation (Equation (2.9)), it is noticed that there is a relationship present with the square of any velocity vector magnitude. This alludes to the need for a relationship that at least involves a relationship of K to Δv^2 . Further inspection of the orbital energy equation shows that an increase in velocity due to an impulsive maneuver vector affects the equation in the following fashion:

$$v^2 = (\mathbf{v}_0 + \Delta \mathbf{v}) \cdot (\mathbf{v}_0 + \Delta \mathbf{v}) = v_0^2 + 2 (\Delta \mathbf{v}) \cdot (\mathbf{v}_0) + \Delta v^2$$

where, \mathbf{v}_0 is the original velocity vector, $\Delta\mathbf{v}$ is the applied impulsive change in the velocity vector. As a result of the maneuver, both linear and quadratic forms of Δv are now present for all directions. Therefore, functions with linear terms, squared terms, and both linear and squared terms are considered, and a function with a quadratic relationship including dependence on both linear and quadratic terms makes logical sense as a potential best fit relationship expectation. Hence, the five curve fit relationships chosen for investigation are: Linear ($y = mx + b$); Square Root ($y = c + b\sqrt{x}$); Square ($y^2 = c + bx$); Quadratic ($y = b + cx + dx^2$); and, the Logarithm of the Quadratic ($y = 20 \log_{10}(b + cx + dx^2)$). Note that the Square fit relationship is listed as "nonlinear" in the figures, and the two are equivalent for this section.

The expectation, based on the above orbital energy equation expansion, is for the quadratic or logarithmic relationships to be presented as the best fit options, and could consequently return the best Δv predictions given a K-value. It is expected that the term representing v_0^2 will be much greater than the coefficient representing $2v_0$, which will be greater than the coefficient associated with Δv , due to the orders of magnitude in difference between v_0 and Δv , as further discussed later in this section. Thus, the following outcomes through the curve fitting analysis process are expected: $v_0^2 > 2v_0\Delta v > \Delta v^2$ (per direction and overall); and, $K = f(\Delta v, \Delta v^2)$.

From Table 4.2, the coefficients of the fitted curves can be analysed. On the surface it would appear as if the square fit shows the strongest dependence on its coefficients with the highest values. However, due to the units present of the x - and y - variables (since these were not nondimensionalised, as mentioned above, and thus the dimensionless K^2 is compared to Δv (m/s), which does not follow in accordance with the above system inspection and relationship expectations), and the exclusion of a Δv^2 term (deemed necessary in the discussion above); this relationship would not actually be a good fit choice, which is supported by the low correlation values of the R^2 numbers in Table 4.3. Thus, the square fit is omitted in subsequent sections.

Visually, the quadratic and logarithmic fits seem to be the best options in all directions. Physically, this is consistent with the above discussion of the orbital energy equation, and is also consistent with the fact that the system and equations of motion for these scenarios are nonlinear (presented in Chapter 2). Hence, a linear relationship would not be an accurate fit (but is still included throughout as a baseline reference). Additionally, since the new K term is defined using the logarithm, a relationship that incorporates a logarithmic expression makes logical sense as a possible best fit choice. Thus, the two best fit options (quadratic and logarithm of the quadratic) are the focus for discussions.

For all cases shown in Table 4.2, except the logarithmic fit for maneuvers in the radial and transverse directions, the relationship shows a stronger dependence on the Δv -independent terms, suggesting that the values of K have a stronger dependence on these terms, which involve v_0 . This is expected and consistent with energy equation inspection above, as the Δv -independent terms represent v_0^2 , which is the original orbital velocity term squared, and is much larger in order of magnitude than the order of magnitude of a Δv or other terms (e.g. $v_0 \sim 10^3$ m/s, $\Delta v \sim 1$ m/s; where Δv is only but a fraction of v_0 with respect to magnitude). Considering that the orbital energy involves dependence on Δv^2 , the most interesting cases to analyse are the quadratic and logarithmic curve fits, which involve both Δv and Δv^2 terms.

In all directions, for the quadratic fit, the highest dependence is on the Δv -independent term, b (or v_0^2); and the lowest dependence is on the very small Δv^2 term, d , ranging on the order of 10^0 to 10^{-3} . The linear term, c (or $2v_0$, associated with Δv), is generally in the middle, as expected. With both linear and quadratic terms present, this shows that K is a function of Δv and Δv^2 ($\therefore K = f(\Delta v, \Delta v^2)$), and thus involves a complicated relationship with the comparatively low magnitude Δv . This is important, as the Δv is not always applied in the same direction as v_0 and can further complicate the K - Δv relationship. Another observation is that the values of b are generally close to the threshold value of $K_{th} = 20 \log_{10}(\Psi_{th=30} + 1) \approx 30$ (per Equation (3.26) and Section 3.3.2 examples). This is justified by inspecting both the definition of K and the quadratic relationship with Δv . With a logarithmic definition comparable to the definition of a conversion to decibels (dB) [62], 30 in the linear scale is equal to 30 dB, and indicates the lowest possible value for the Δv -independent term. In the quadratic relationship, with $\Delta v = 0$ (or even $\Delta v \approx 0$), only be the v_0^2 term will remain present (or will further dominate the relationship), and thus the Δv -independent term will be near the threshold, such that $b \approx 30 \approx K_{th}$.

The negative value of the d -terms in the quadratic fit may indicate dependence on the negative of Δv^2 for the radial and transverse directions. However, the negative term, c , in both the logarithmic and quadratic relationship for the normal direction is a peculiar result, as it suggests dependence on the negative of v_0 and Δv , yet there is no apparent dependence on the negative of the Δv^2 (due to a positive d -value). It would be expected that with a dependence on the negative of v_0 and Δv , that the d coefficient would be affected as well. However, this result may be justified by inspecting the orbital energy equation (Equation (2.9)) once again, where elements of v_0 and Δv are squared, and thus, any negative values will still result in positive outcomes. In another sense, these negative d -values may indicate that this is not actually a good fit, especially when considering very small values of Δv , as these values may be too close to zero and induce

other computational errors. For these reasons, the relationships with the negative Δv and Δv^2 terms are unclear at this time.

The above quadratic relationship trends with the coefficients changes for the logarithmic fit over the different directions. In the radial and transverse directions, the relationship shows stronger dependence on c , associated with the linear v_0 and Δv terms; though the dependence is still weaker with d , and thus, on Δv^2 . This means that K depends more on the linear Δv variable than with the Δv -independent term depicted in the previous observations for the quadratic relationship. The Δv -independent term, b , is also negative for the radial direction, and thus, K may vary with the negative of v_0^2 for this specific case, though the relationship for negative values is inconclusive at this time. The curve fit for the normal direction follows the same relationship for the quadratic fit cases discussed above, with strongest dependence on v_0^2 , and weakest dependence Δv^2 . In this specific case, the linear coefficient term, c , is negative, again, indicating that K may vary with the negative of v_0 or Δv (but not the negative of Δv^2), which is also consistent with observations of the quadratic fit in the normal direction. Additionally, the R^2 numbers in Table 4.3 support the selection of the logarithmic fit as the best potential curve fit relationship between K and Δv , as $R^2 \approx 1$ for all directions.

In summary, due to the dominating quadratic relationship in Δv present from expanding velocity in the orbital energy equation, and the logarithmic definition of K , it is recommended for the curve fit function for the logarithm of the quadratic to be used for maneuver characterisation and prediction purposes. This would then allow for a calibration of sorts to be carried out by operators. By knowing the K -value (which could even be determined at the time the original Ψ -parameter deems a detection is made) the chosen relationship can be used to determine the most likely impulsive Δv applied and the possible outcomes with respect to orbital geometry and trajectory changes. A sudden change in K would then show the possible onset time of maneuver, similarly to the original Ψ -parameter in Goff et al. [41]. The different values of K and the curve fit coefficients (b , c , d) could then relate to different maneuvering directions and orbital locations, which is briefly explored in the next sections.

At the same time, since the results and testing set up are limited, a concrete relationship may not yet be present, and further testing scenarios are necessary. The possible process for operators could be: 1) Calibrate system per chosen relationship; 2) Determine detection with prominent peak in K ; 3) Apply the logarithmic relationship to K ; 4) Determine Δv type (in terms of direction, magnitude, location, or original orbital properties of the maneuvering spacecraft); 5) Apply collision avoidance prediction or decision-making protocol.

Table 4.2: Apogee Coefficients for Curve Fit Lines of the K- Δv Relationship

	Linear $y = mx + b$		Square Root $y = c + b\sqrt{x}$		Square $y^2 = c + bx$		Quadratic $y = b + cx + dx^2$			Logarithmic $y = 20 \log_{10}(b + cx + dx^2)$		
	m	b	c	b	c	b	b	c	d	b	c	d
Radial	0.5244	46.8325	34.4062	6.4230	1801.6269	83.9924	37.9894	1.6449	-0.01150	-8.9891	74.4401	3.7804
Transverse	0.4608	42.9008	32.9615	5.4092	1604.9774	63.5357	38.09184	1.07015	-0.00627	6.1991	50.6466	0.7132
Normal	0.1269	30.2850	28.6861	1.2167	913.9629	8.9000	31.4265	-0.01770	0.001487	38.9983	-0.5341	0.01768

Table 4.3: Apogee R² Numbers for Curve Fit Lines of the K- Δv Relationship

	Linear $y = mx + b$		Square Root $y = c + b\sqrt{x}$		Square $y^2 = c + bx$		Quadratic $y = b + cx + dx^2$		Logarithmic $y = 20 \log_{10}(b + cx + dx^2)$	
	R ²	R ² adjusted	R ²	R ² adjusted	R ²	R ² adjusted	R ²	R ² adjusted	R ²	R ² adjusted
Radial	0.9547	0.9524	0.8672	0.8406	0.7509	0.7011	0.8934	0.8402	0.9784	0.9676
Transverse	0.9784	0.9773	0.9148	0.8977	0.8205	0.7847	0.8626	0.7939	0.9810	0.9715
Normal	0.9981	0.9980	0.7276	0.6731	0.8795	0.8554	0.9977	0.9966	0.9950	0.9925

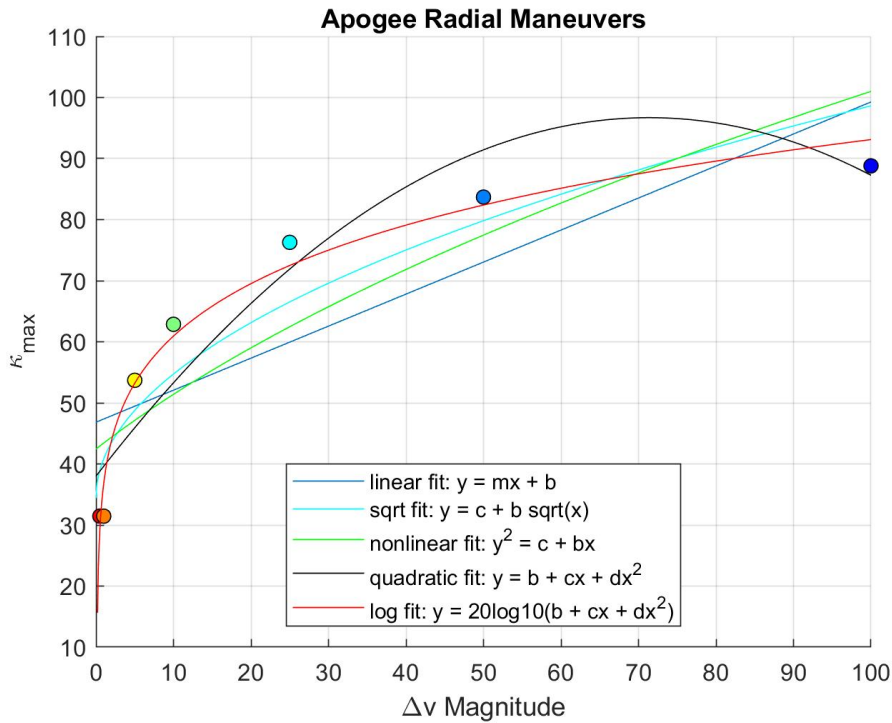


Figure 4.1: Trend of K (κ_{\max}) with varied apogee radial maneuvering Δv (m/s).

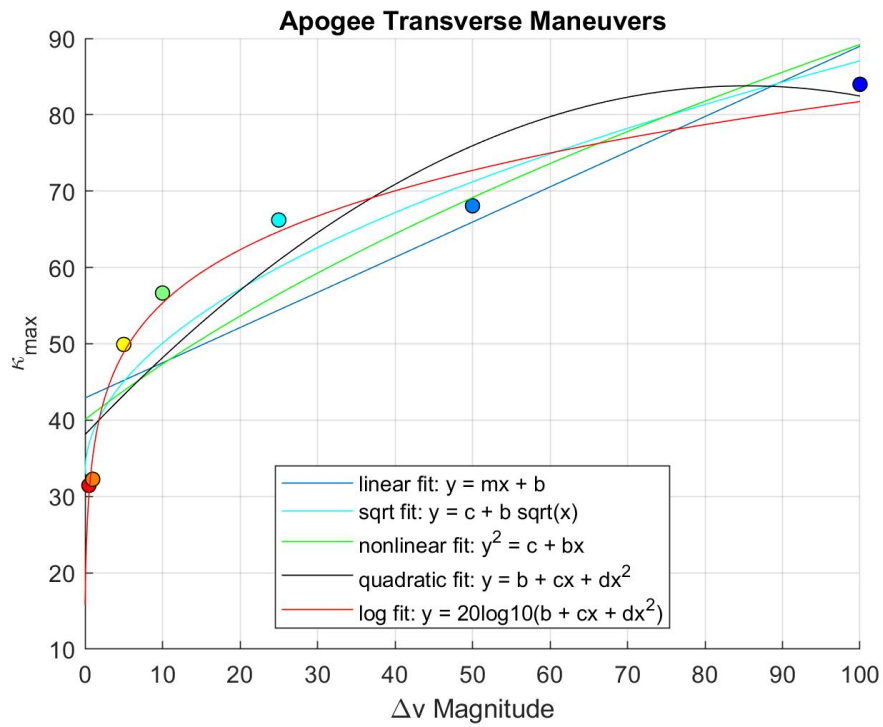


Figure 4.2: Trend of K (κ_{\max}) with varied apogee transverse maneuvering Δv (m/s).

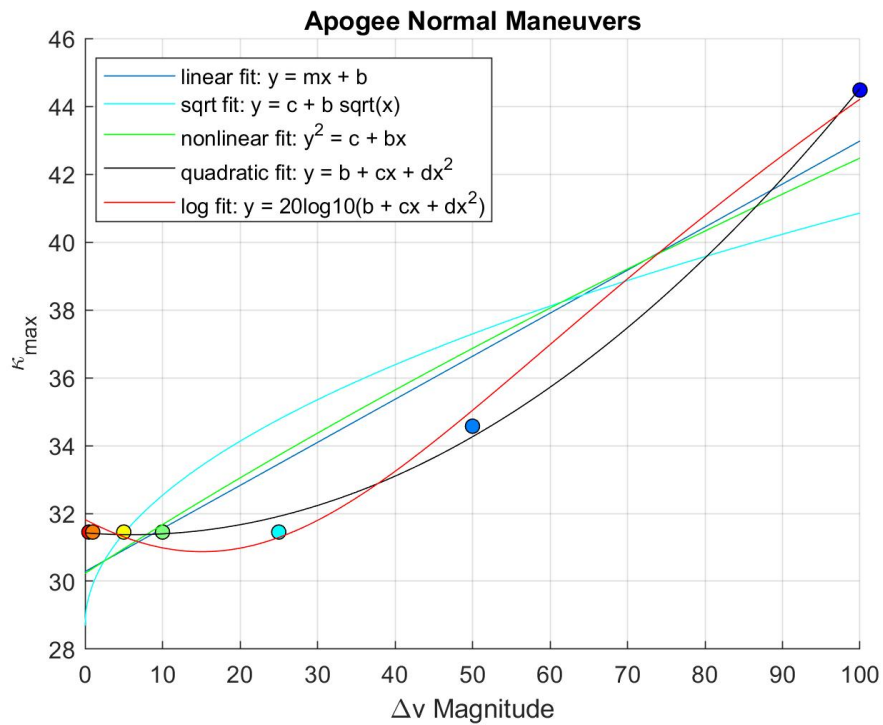


Figure 4.3: Trend of K (κ_{\max}) with varied apogee normal maneuvering Δv (m/s).

For relationships with Ψ vs Δv , Figures 4.4 to 4.6 show the variation in the original Ψ detection parameter by Goff et al. [41] for each applied maneuvering direction at apogee. Overall, the trends are similar to those found for K: the variation of Ψ ranges from the greatest to smallest in the same order as before — radial, transverse, normal; as the maneuver velocity magnitude increases, the magnitude of Ψ increases, which is also consistent with Goff et al. [41]; the relationship is not proportional and is nonlinear, as expected. The same curve fitting methods as for the K cases were used, and the corresponding coefficients of the curve fit equations are tabulated in Table 4.4, while the correlation measures by the R^2 and R^2 -adjusted values are tabulated in Table 4.5.

For the Ψ - Δv curve fits, it was not possible to consistently obtain either: a square fit ($y^2 = c + bx$) — which is analogous to the K- Δv cases (where it had the lowest correlation values), and is not truly physically meaningful; nor, a logarithmic fit — which would not fit well without a logarithmic relationship already present within the definition of Ψ . Hence, these two fits are omitted in all Ψ - Δv results. Similarly to the curve fits for K- Δv , the Ψ -parameter has a stronger dependence on the Δv -independent coefficient (which is v_0^2), and a weaker relationship with Δv^2 , which is also consistent for nearly all maneuvering directions. The trend differs for maneuvers applied in the normal direction with the square root ($y = c + b\sqrt{x}$) fit, where the dependence is weaker on the v_0 term as opposed to stronger. Another interesting observation is that many of the coefficients are negative, some with very large quantities (indicating even greater dependence on the associated values), and are of different values than with the results for the K- Δv cases. The implications of negative coefficients remains unclear at this time.

From the R^2 numbers in Table 4.7 and the corresponding graphs, the best fit option is the quadratic fit for all directions, which supports the observations of the depicted K- Δv relationship proposed above. In addition, the linear correlation values in the radial and transverse directions are outside of the expected range of values for R^2 numbers, which means the linear fit does not correlate well with the results for Ψ . The square root fit correlates less well with the data — decreasing per direction, from radial to transverse to normal — which are much lower than those of the quadratic fit relationship, supporting the quadratic as the best fit choice for Ψ - Δv . This result confirms the conclusions made in the previous discussion on the relationships between the detection parameter and the maneuvering velocity (Δv) with reference to expectations of nonlinear systems, and in regards to the relationship between orbital energy and overall velocity. Thus, the quadratic fit would be the main focus for determination of a Ψ - Δv relationship, supporting the discussion on K curve fits requiring and centring around an included quadratic function. Further Ψ - Δv results are included in Appendix E for reader interest.

Table 4.4: Apogee Coefficients for Curve Fit Lines of the Ψ - Δv Relationship

	Linear $y = mx + b$		Square Root $y = c + b\sqrt{x}$		Quadratic $y = b + cx + dx^2$		
	m	b	c	b	b	c	d
Radial	286.6935	-509.4414	-5074.7721	2977.0210	-827.6546	327.0128	-0.4145
Transverse	147.4418	-966.4376	-2885.1733	1428.0750	415.0241	-27.5972	1.7998
Normal	1.2252	23.7468	9.2188	11.5269	38.3235	-0.6218	0.01899

Table 4.5: Apogee R^2 Numbers for Curve Fit Lines of the Ψ - Δv Relationship

	Linear $y = mx + b$		Square Root $y = c + b\sqrt{x}$		Quadratic $y = b + cx + dx^2$	
	R^2	R^2 adjusted	R^2	R^2 adjusted	R^2	R^2 adjusted
Radial	-157.2368	-165.1486	0.9350	0.9220	0.9956	0.9934
Transverse	-870.7472	-914.3346	0.7281	0.6737	0.9855	0.9782
Normal	0.7025	0.6876	0.6577	0.5886	0.9987	0.9980

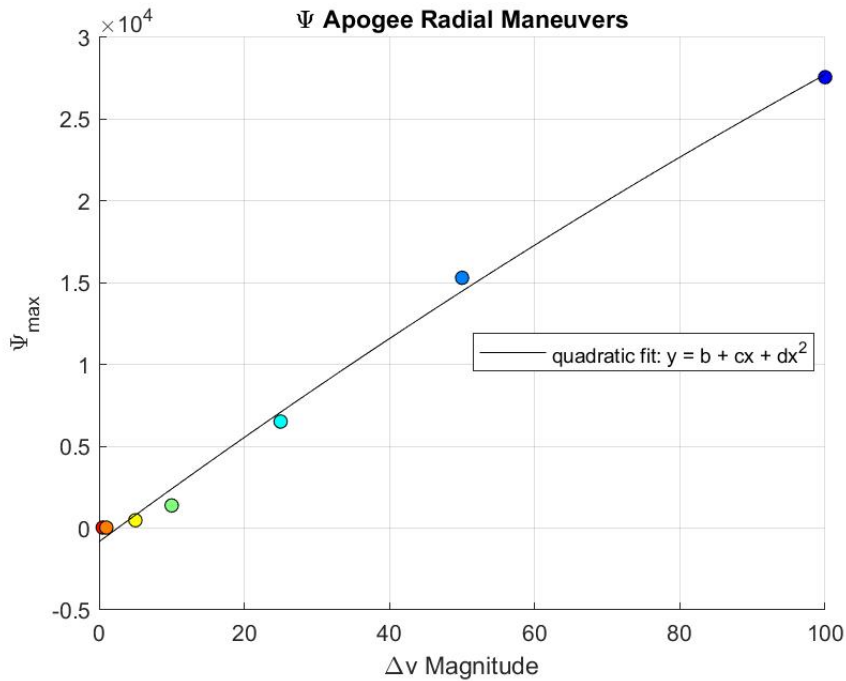


Figure 4.4: Trend of Ψ (Ψ_{\max}) with varied apogee radial maneuvering Δv (m/s).

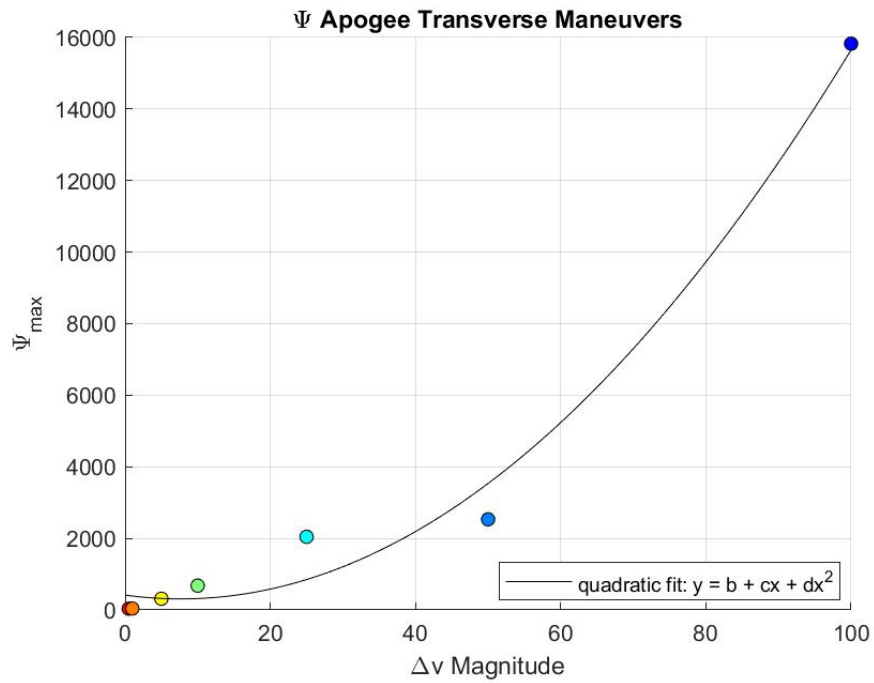


Figure 4.5: Trend of Ψ (Ψ_{\max}) with varied apogee transverse maneuvering Δv (m/s).

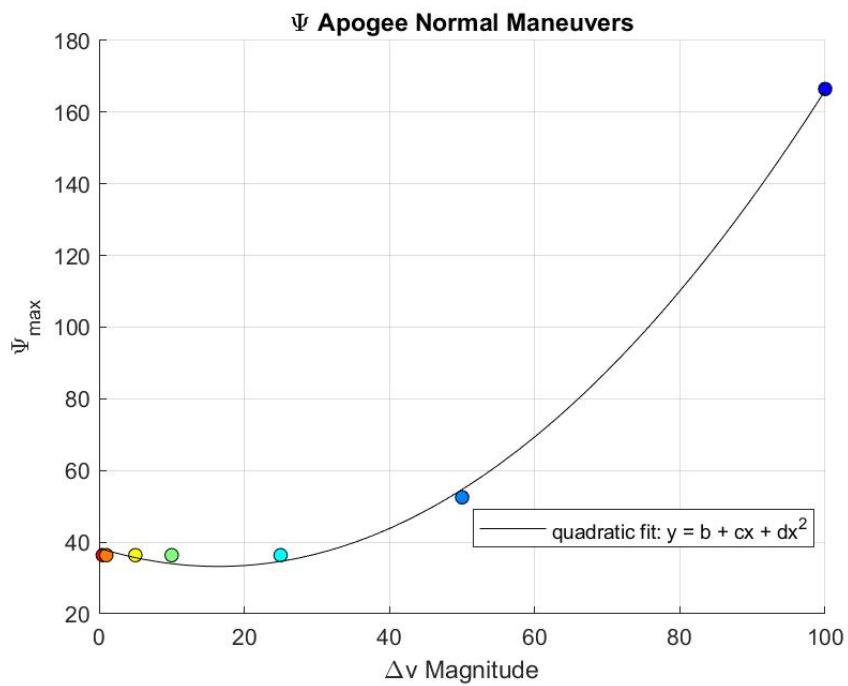


Figure 4.6: Trend of Ψ (Ψ_{\max}) with varied apogee normal maneuvering Δv (m/s).

4.2.2 Variation of K with Orbital Location

In this set of simulations the relationship of $K-\Delta v$ is tested at different orbital locations. The same maneuvers from Section 4.2.1 were applied at the orbital perigee, as well as the two locations halfway between orbital perigee and apogee of the same orbital geometry as Section 4.2.1. Figure 4.7 shows the variation in the new K detection parameter versus the tested Δv maneuvering values applied at the orbital perigee, while Figures 4.8 and 4.9 show the results for maneuvers applied at the halfway points after perigee and after apogee, respectively. Similarly, the original Ψ -parameter was tested in these scenarios and curve fits were applied, of which the results and discussions can be found in Appendix E. As stated in Section 4.2.1, the focus is on maneuvers in the transverse direction, thus only these results are illustrated in this section. A qualitative summary of results is included in Appendix C.

For transverse maneuvers applied at the orbital perigee, the variation of the new K detection parameter ranges from $30 < K < 47$. At a quarter of the orbit after orbital perigee, the variation in the range is $30 < K < 60$, and similar at $30 < K < 70$ for transverse maneuvers applied at a quarter of the orbit after apogee. The similar ranges for the orbital halfway points makes sense, as the velocities would be near equal at these locations (in terms of magnitude), hence, the ranges should be comparable in these areas. For transverse maneuvers, the largest variance in K occurs when maneuvers are applied at apogee, followed by the halfway point after apogee, then the halfway point after perigee, leaving the smallest range to maneuvers applied in the transverse direction at perigee. Therefore, if $K_{(\cdot)}$ represents the range of the K-parameter at different maneuvering locations, then: $K_{\text{ap}} > K_{1/4 \text{ ap}} > K_{1/4 \text{ per}} > K_{\text{per}}$, for transverse maneuvers.

This observation can be justified by considering Kepler's Laws, as spacecraft velocity is greatest at the perigee [53,54]. By inspecting and applying vis-viva equations [53,54], it is apparent that perigee maneuvers require larger Δv magnitudes, implying that greater added energy is required for a change to occur. Thus, the associated variance in the range of K is decreased, as changes in velocity at perigee would be less easily conducted and affect less change. Overall, the same expected general trends can be deduced in all cases, where the magnitude of K increases with increasing Δv in a nonlinear fashion. In this scenario, the five curve fits were more closely packed when plotted together.

The coefficient values of the fitted curves for perigee maneuvering cases in Table 4.6, are more consistent with each other than in the previous section; the Δv -independent variable, b (which is v_0^2), for each fit case and maneuvering direction contains the largest value, and thus, K has greater dependence on v_0^2 for all of these cases. The only negative values are in the Δv^2 term, d , of the quadratic fit for the radial and transverse

maneuvering cases, which were also negative in the previous section. The peculiarity and unclear implications of the negative terms to the K - Δv relationship remains consistent as well. In addition, this d -term is the smallest value overall, across all curve fit relationships and maneuvering directions for this scenario, and is also consistent with the previous section. The small d -values at an order of magnitude of 10^{-4} and 10^{-5} indicate a weak dependence on Δv^2 for K . These consistencies in the observations of the results support the focus of curve fits involving a quadratic relationship as best possible options for the analytical relationship between the K detection parameter and Δv .

By the R^2 numbers in Table 4.7 for the perigee maneuver location, the logarithmic and quadratic fits would not immediately seem to be the best fit options for maneuvers applied at perigee. However, physically and visually, as previously discussed, the curve fit should involve a quadratic relationship, due to the nature of the nonlinear system, as evidenced by inspecting the orbital energy equation, which is consistent with the results discussed in Section 4.2.1. Consequently, the quadratic and logarithm of the quadratic curve fits are chosen as the focus for discussion of the maneuvers applied at the halfway points between orbital perigee and apogee.

The coefficient values of the fit curves for maneuvering cases at a quarter of the orbit after perigee are tabulated in Table 4.8. Overall, the same trend is observed as with the perigee maneuvering case, where the larger values of the Δv -independent terms in the fitted curves allude to having the strongest influence on K . The Δv^2 d -terms for the logarithmic and quadratic fits are still the smallest for all directions, but are slightly larger at orders of magnitudes of 10^{-3} and 10^{-4} for the quadratic cases, which allude to a slightly stronger relationship to Δv^2 in these cases. There are also two negative coefficients in the logarithmic fit: the term, c , for the transverse direction, meaning that K depends on the negative of v_0 and Δv ; and the term, d , for the normal direction indicating that K depends on the negative of the Δv^2 . That said, the true implications of the negative relationship remains unclear at this time.

As for the coefficients for the curve fits in the quarter of an orbit after apogee cases, the coefficients vary greatly from each other, especially for the different directions in the logarithmic fit, as shown in Table 4.9. The coefficients of the radial direction are the largest for the logarithmic fit with this case than any of the previous cases. This implies that in the radial direction, K has a stronger dependence on all of its associated coefficients and is prone to greater variance in this relationship than with those of the other directions for maneuvers applied at a quarter of the orbit after apogee. In addition, the negative linear term, c (which is double v_0 and associated with Δv), is now observed in the radial maneuvering direction for the logarithmic case, rather than the transverse case observed

before with maneuvers applied at a quarter of the orbit after perigee. As with the apogee maneuvering cases, the small d -terms of the quadratic fits are negative in the radial and transverse directions, alluding to a potential relationship with the negative of Δv^2 , though the true implications remain unclear. However, the order of magnitude of d is higher than both the perigee and quarter of an orbit after perigee cases ($d \sim 10^{-2}$ or $d \sim 10^{-3}$), relating more closely to apogee cases, with orders of magnitudes of 10^0 and 10^{-1} , respectively by direction. The d -term for the normal direction of the logarithmic fit is the smallest, which implies that this case varies least with Δv^2 than the other directions of this fit. This is consistent with expectations and justifiable per discussions in the previous sections.

In summary, there seems to be a consistent trend with the quadratic and logarithmic relationships when analysing the coefficients, with some variance between the different maneuvering locations and directions. It is possible that a relationship between curve fit coefficients and different maneuvering locations exists. However, at this time, there may not be a prominent nor discernible pattern to dictate a consistent relationship per orbital location, and thus, further analysis is necessary.

Table 4.6: Perigee Coefficients for Curve Fit Lines of the K- Δv Relationship

	Linear $y = mx + b$		Square Root $y = c + b\sqrt{x}$		Quadratic $y = b + cx + dx^2$			Logarithmic $y = 20 \log_{10}(b + cx + dx^2)$		
	m	b	c	b	b	c	d	b	c	d
Radial	0.1893	32.1677	28.9354	2.0181	31.7478	0.2425	-0.0005471	39.03095	0.9433	0.01966
Transverse	0.1551	31.3475	28.7300	1.6462	31.1161	0.1845	-0.0003015	35.1564	0.8710	0.008205
Normal	0.1668	31.3728	28.7394	1.7267	31.4375	0.1586	0.00008421	37.5967	0.4785	0.01593

Table 4.7: Perigee R^2 Numbers for Curve Fit Lines of the K- Δv Relationship

	Linear $y = mx + b$		Square Root $y = c + b\sqrt{x}$		Quadratic $y = b + cx + dx^2$		Logarithmic $y = 20 \log_{10}(b + cx + dx^2)$	
	R^2	R^2 adjusted	R^2	R^2 adjusted	R^2	R^2 adjusted	R^2	R^2 adjusted
Radial	0.9981	0.9980	0.8538	0.8246	0.8666	0.7999	0.8647	0.7971
Transverse	0.9998	0.9998	0.9615	0.9538	0.9816	0.9724	0.9808	0.9712
Normal	0.9996	0.9995	0.9220	0.9063	0.9866	0.9799	0.9820	0.9730

Table 4.8: Coefficients for Best Curve Fit Lines of the $K-\Delta v$ Relationship at a Quarter of the Orbit after Perigee

	Linear $y = mx + b$		Square Root $y = c + b\sqrt{x}$		Quadratic $y = b + cx + dx^2$			Logarithmic $y = 20 \log_{10}(b + cx + dx^2)$		
	m	b	c	b	b	c	d	b	c	d
Radial	0.2275	31.8943	27.9710	2.4342	30.8090	0.3650	-0.001414	35.9044	1.1951	0.03279
Transverse	0.2784	30.7748	26.2759	2.9067	30.09432	0.3646	-0.0008866	36.7672	-0.3567	0.07954
Normal	0.1271	32.4990	29.9451	1.4470	30.6833	0.3572	-0.002365	33.4793	2.1565	-0.01053

Table 4.9: Coefficients for Curve Fit Lines of the $K-\Delta v$ Relationship at a Quarter of the Orbit after Apogee

	Linear $y = mx + b$		Square Root $y = c + b\sqrt{x}$		Quadratic $y = b + cx + dx^2$			Logarithmic $y = 20 \log_{10}(b + cx + dx^2)$		
	m	b	c	b	b	c	d	b	c	d
Radial	0.5120	39.5683	25.4666	6.7439	14.9420	3.6323	-0.03208	60.9982	-25.0722	3.7655
Transverse	0.3435	34.2645	28.05677	3.7441	32.7966	0.5295	-0.001912	36.1324	4.1442	0.1324
Normal	0.01584	31.3606	31.1321	0.1588	31.3974	0.01118	0.00004794	37.1588	0.04458	0.0003044

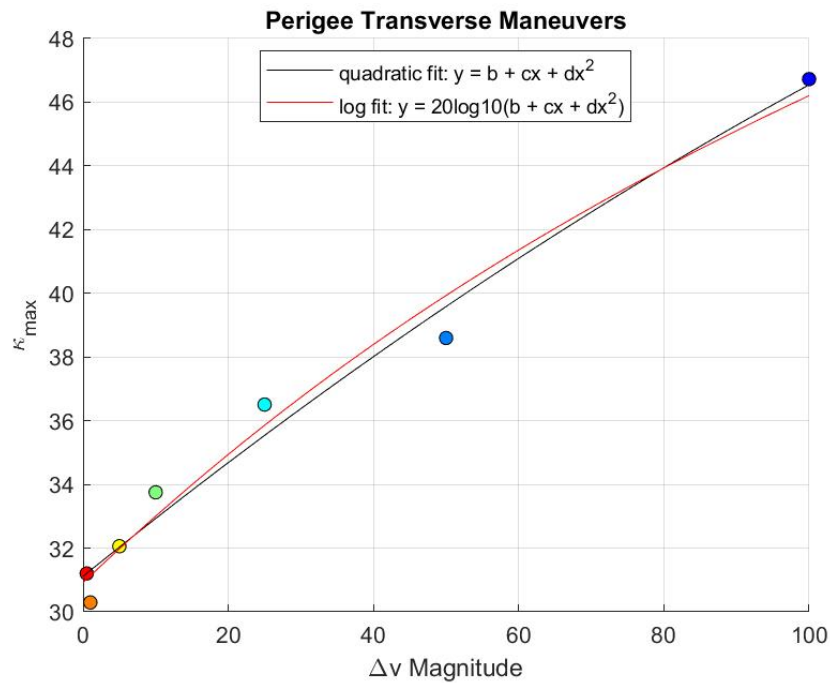


Figure 4.7: Trend of K (κ_{\max}) with transverse perigee maneuvers of varied Δv (m/s).

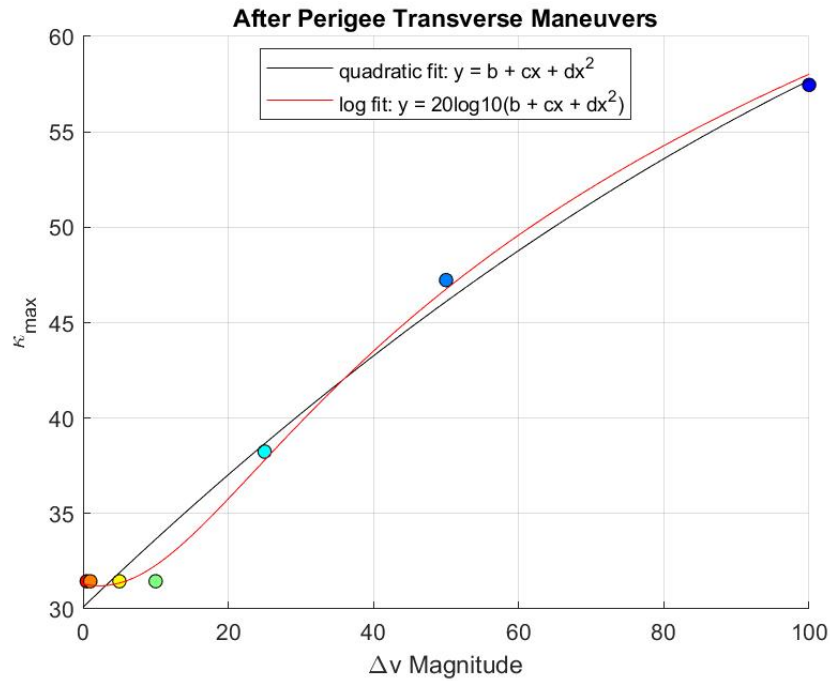


Figure 4.8: Trend of K (κ_{\max}) with transverse maneuvers of varied Δv (m/s) applied at a quarter of the orbit after perigee.

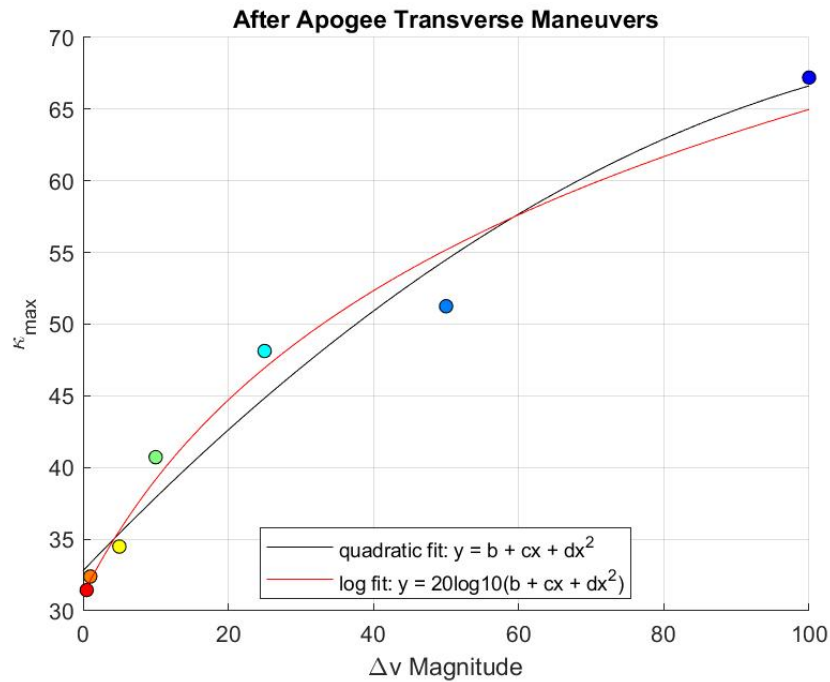


Figure 4.9: Variation of K (κ_{\max}) with transverse maneuvers of varying Δv (m/s) applied at a quarter of the orbit after the orbital apogee.

4.2.3 Variation of K with Different Orbits

In this set of simulations, the maneuvers from Section 4.2.1 were applied at both the orbital perigee and apogee of a different Low Earth Orbit (LEO). The tested orbital cases are shown in Table 4.10, where the results for orbital Case 1 were previously presented in Sections 4.2.1 and 4.2.2.

Table 4.10: Initial Orbital Elements of Tested Orbital Cases

	a (km)	e	i (°)	Ω (°)	ω (°)	$\nu_{t=0}$ (°)
Case 1	8 107.8	0.09	0	0	0	0
Case 2	7 345.4	0.05	10	0	0	0

Figures 4.10 and 4.11 show the variation in the K detection parameter versus the tested Δv values for the different orbit (orbital Case 2) with maneuvers applied in the transverse direction at the orbital perigee and apogee, respectively. A qualitative summary of these results is included in the tables of Appendix C. Results and discussion for comparison with the Ψ parameter can be found in Appendix E.

For the apogee transverse maneuvers, the range is $30 < K < 70$, and is smaller, at $30 < K < 39$ for the transverse maneuvers applied at perigee. This is consistent with the results of the previous section, where the perigee transverse maneuvers varied less than at apogee. As expected, the same general trend can be deduced: the magnitude of K increases with increasing Δv in a nonlinear fashion.

Furthermore, the v_0^2 terms of the curve fits contain the largest values, consistently suggesting stronger dependence of K on v_0^2 , evidenced by Table 4.11. The Δv^2 terms in the quadratic and logarithmic fits are the smallest, consistently suggesting weaker dependence of K on Δv^2 . The order of magnitude of the d -terms are larger at apogee than perigee, which is consistent with previous results for the logarithmic fit. One major difference, is that all Δv^2 terms are negative in the quadratic fit. This may have relation to either the size or orbital inclination, or both, though is currently unclear. In addition, K varies with the negative of Δv^2 in the radial and transverse directions applied at apogee, as well as the negative of v_0 (associated with Δv), for the logarithmic apogee radial and normal directions of this orbital case. Per previous discussions, the true relations and implications of the negative coefficient values remains unclear at this time. Maneuvers in the normal direction have the greatest dependence on v_0 for the quadratic and logarithmic cases at perigee, which differs from the results of orbital Case 1 (of Section 4.2.2). Again, more testing may be necessary to discern a consistent K- Δv relationship with varied orbital location, maneuvering direction, and orbital geometry.

Table 4.11: Coefficients for the Curve Fit Lines of the K - Δv Relationship for Maneuvers Applied in the Second Orbital Case

Perigee Maneuvers										
	Linear $y = mx + b$		Square Root $y = c + b\sqrt{x}$		Quadratic $y = b + cx + dx^2$			Logarithmic $y = 20 \log_{10}(b + cx + dx^2)$		
	m	b	c	b	b	c	d	b	c	d
Radial	0.1583	33.2557	30.1230	1.7908	31.0721	0.4350	-0.0028448	35.6503	2.7260	-0.008520
Transverse	0.0803	32.6230	30.7937	0.9659	31.0769	0.2762	-0.0020144	34.1933	1.7915	-0.01276
Normal	0.1180	32.8775	30.7174	1.2930	32.7304	0.1367	-0.0001916	41.0632	1.0416	0.001312

Apogee Maneuvers										
	Linear $y = mx + b$		Square Root $y = c + b\sqrt{x}$		Quadratic $y = b + cx + dx^2$			Logarithmic $y = 20 \log_{10}(b + cx + dx^2)$		
	m	b	c	b	b	c	d	b	c	d
Radial	0.4074	32.1499	25.0698	4.3729	30.1785	0.6572	-0.002568	38.3991	-0.9417	0.2937
Transverse	0.4281	33.9230	25.3862	4.8579	28.8522	1.0706	-0.006606	29.7950	1.2838	0.4742
Normal	0.4417	32.6904	24.7332	4.8083	29.6725	0.8241	-0.003932	38.3408	-2.1765	0.4690

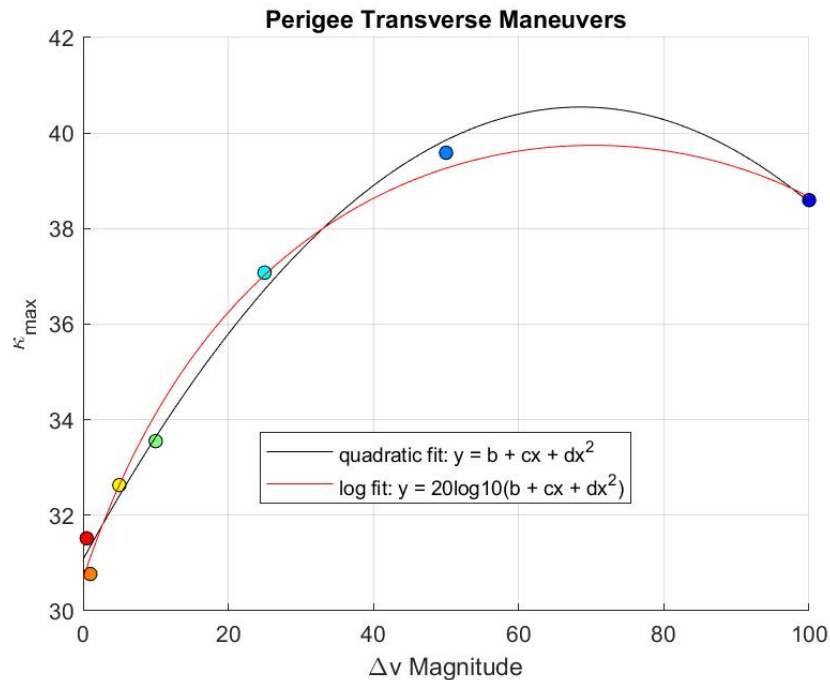


Figure 4.10: Trend of K (k_{\max}) with Transverse Perigee Maneuvers of varying Δv (m/s) for the Second Orbital Case.

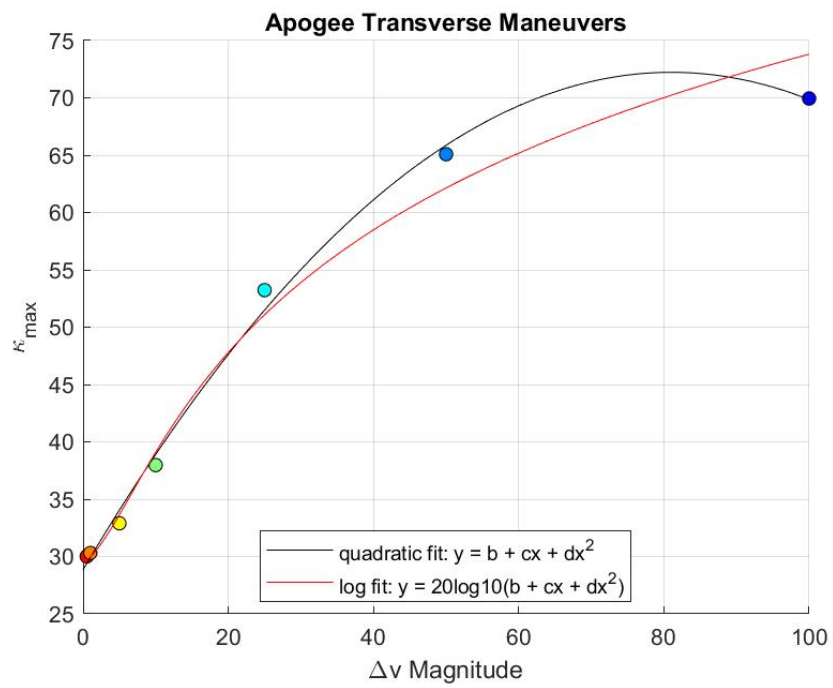


Figure 4.11: Trend of K (κ_{\max}) with Transverse Apogee Maneuvers of varying Δv (m/s) for the Second Orbital Case.

4.2.4 Variation of K with Measurement Noise Covariance, \mathbf{R}

In this set of simulations, the order of magnitudes in the measurement noise covariance matrix were varied in two cases: 1) $\mathbf{R} = 10\mathbf{R}$; and, 2) $\mathbf{R} = \mathbf{R}/10$. The maneuvers from Section 4.2.1 were applied at both the perigee and apogee of orbital Case 1 defined previously. This section showcases the apogee transverse maneuver results, with perigee results provided in Appendix D. Since the quadratic and logarithmic curve fits were previously selected for the relationships of focus, only these results are evaluated. Appendix E contains the results for the original Ψ -parameter for reader interest.

For the first case ($\mathbf{R} = 10\mathbf{R}$), the range is $30 < K < 95$ for the maneuvers applied at the orbital apogee (Figure 4.12), and larger at $20 < K < 140$ for perigee maneuvers (Figure D.1), which is different than the previously discussed results. For the second case ($\mathbf{R} = \mathbf{R}/10$), the range is $30 < K < 85$ for the maneuvers applied at the orbital apogee (Figure 4.13), and is smaller at $30 < K < 55$ for perigee maneuvers (Figure D.2). From these ranges, no true discernible pattern can be determined. However, it is interesting that with a change in measurement noise covariance, the ranges of K have increased for all cases. The range for the first case ($\mathbf{R} = 10\mathbf{R}$) is greatest at apogee. The range for the second case ($\mathbf{R} = \mathbf{R}/10$) is greatest at perigee. Thus, if the measurement noise covariance were to be a variable that could be selected or controlled by a spacecraft operator, this may provide capability for discerning a relationship with the maneuver location.

Overall, the same general trend can be deduced in all cases — that the magnitude of K increases with increasing Δv in a nonlinear fashion, as expected. However, for perigee maneuvers with $\mathbf{R} = 10\mathbf{R}$ (Figure D.1) there seems to be an anomaly at $\Delta v = 50$ m/s, which skews the curve fits, creating difficulty for the curves to find a good fit. That said, if the anomaly were removed, the range would be much smaller, at $30 < K < 60$, which is still greater in range than the results in Section 4.2.2, and remains consistent with the above discussion. These observations imply that transverse maneuvers applied at perigee produce smaller variation in K with different magnitudes of Δv , while the same maneuvers applied at apogee produce a greater range in K. Thus, it may be possible to make predictions, stating that K will only fall within a certain range indicative of an applied perigee maneuver, whereas a greater K could indicate the application of an apogee maneuver. This would be highly useful to operators, though further tests would assist in concretely defining this relationship.

The fit coefficients are found in Appendix D (Tables D.1 and D.2), depicting the same general trends: greater dependence on v_0^2 and weaker dependence on Δv^2 . Various negative coefficients are present, the implications of which remain unclear and support the need for further tests.

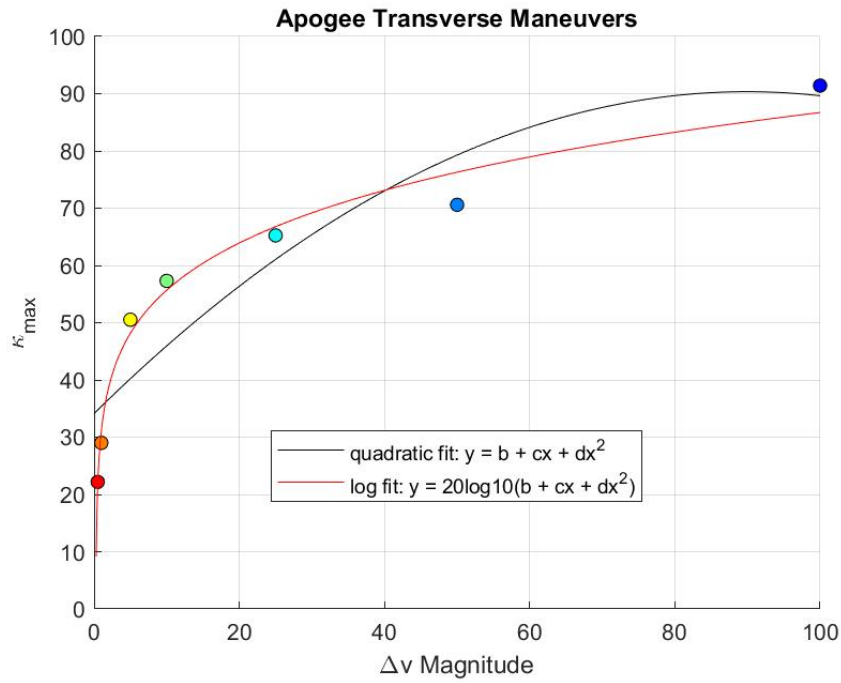


Figure 4.12: Variation of K (κ_{\max}) with Transverse Apogee Maneuvers of varying Δv (m/s) for the first Orbital Case with $\mathbf{R} = 10\mathbf{R}$.

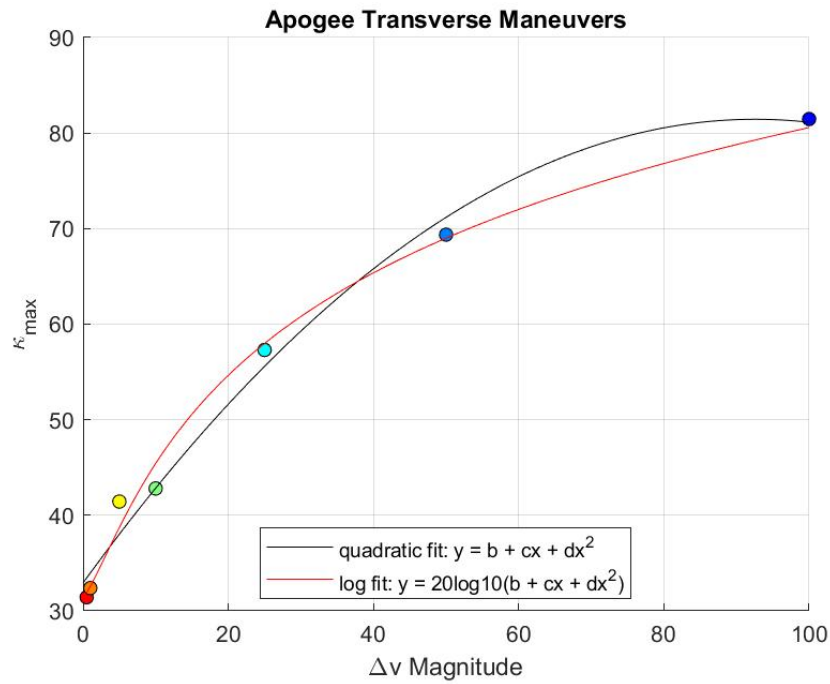


Figure 4.13: Variation of K (κ_{\max}) with Transverse Apogee Maneuvers of varying Δv (m/s) for the first Orbital Case with $\mathbf{R} = \mathbf{R}/10$.

4.2.5 Variation of K with Ψ Threshold and State Covariance Inflation Threshold, η

In this set of simulations, the maneuvers from Section 4.2.1 were applied at both the orbital perigee and apogee of the Case 1 orbit from previous sections. The thresholds of the original Ψ detection parameter and the state covariance inflation parameter, η , were varied in three cases: 1) $\Psi_{th} = 10$; 2) $\Psi_{th} = 100$; and, 3) $\eta_{th} = 0.1$. With transverse maneuvers being the direction of main interest, only these results are illustrated. Further results for these scenarios, and the respective tabulated results can be found in Appendix D (Tables D.3 to D.5). Following suit, results for Ψ in these scenarios are included in Appendix E for reference, and will not be discussed here.

From analysing Figures 4.14 to 4.16, few conclusions can be made. For a lower Ψ_{th} the range in the variation of K is comparable to Section 4.2.1 but has shifted to $21 < K < 75$. For a lower η_{th} the range in the variation of K has increased to $30 < K < 100$ in comparison Section 4.2.1. However, both visually and by the coefficients of the curve fits, similar trends to Section 4.2.1 are depicted. These observations suggest that lowering these thresholds has minimal impact on the K- Δv relationship K due to Δv .

For larger Ψ_{th} , the range of K has shifted and increased to $40 < K < 160$. There is an anomaly at $\Delta v = 50$ m/s, possibly skewing the results, which also occurred in the results of Section 4.2.4. In addition, by Figure 4.15, the logarithmic fit may have struggled to reach a best fit result, deduced by the second curve shown at the lower maneuvering values. This may suggest that a larger Ψ_{th} may not be adequate for detecting smaller magnitude Δv maneuvers. Analysing the coefficients (see Appendix D, Table D.4), the terms are generally on similar orders of magnitude, but with less dependence on negative terms. This suggests that a larger Ψ_{th} value has some impact on the K- Δv relationship, though is possibly minimal.

Overall, further analyses would assist in discerning a relationship with variance in Ψ_{th} and η_{th} on the K- Δv relationship.

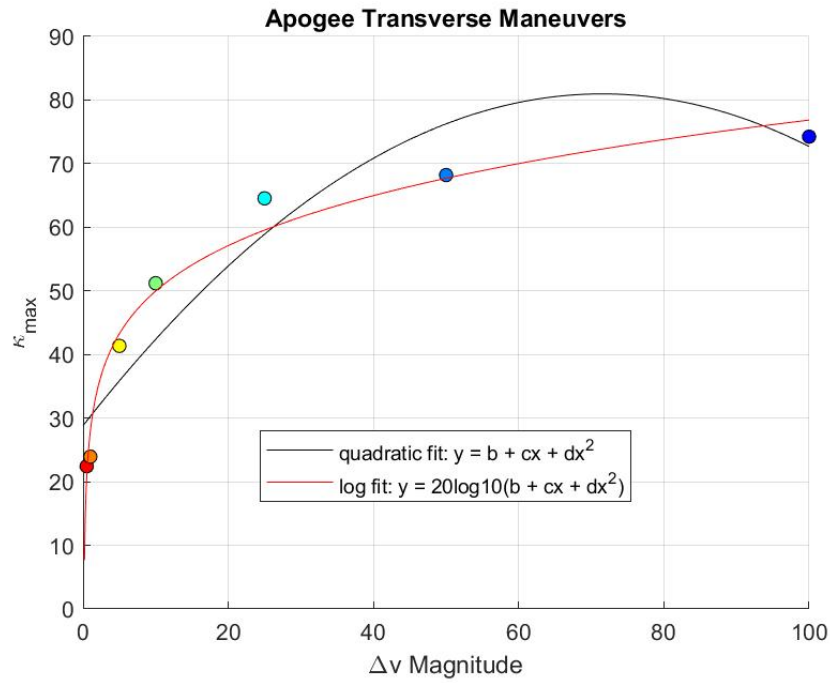


Figure 4.14: Variation of K (κ_{\max}) with transverse apogee maneuvers of varying Δv (m/s) for the first Orbital Case with $\Psi_{th} = 10$.

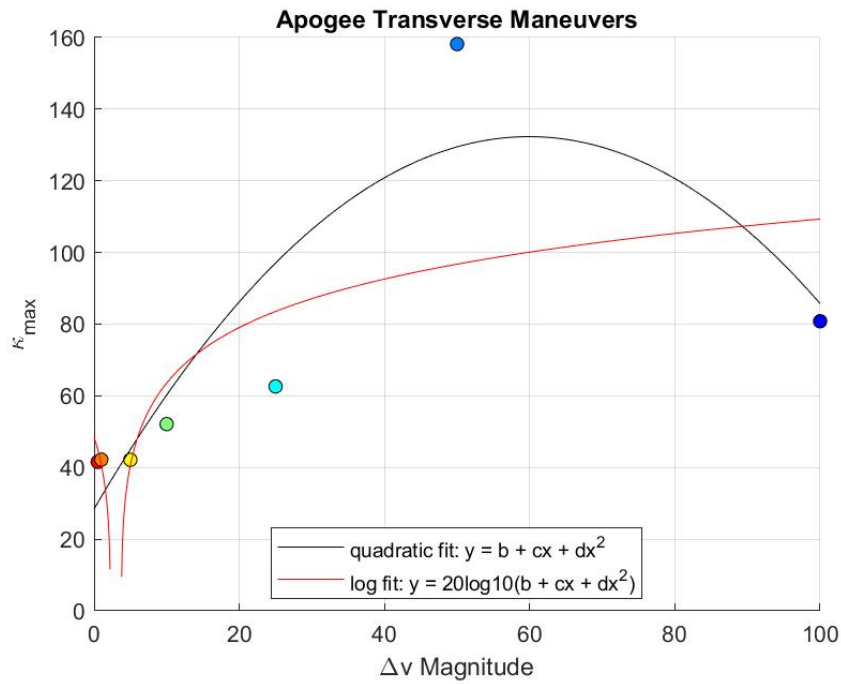


Figure 4.15: Variation of K (κ_{\max}) with transverse apogee maneuvers of varying Δv (m/s) for the first Orbital Case with $\Psi_{th} = 100$.

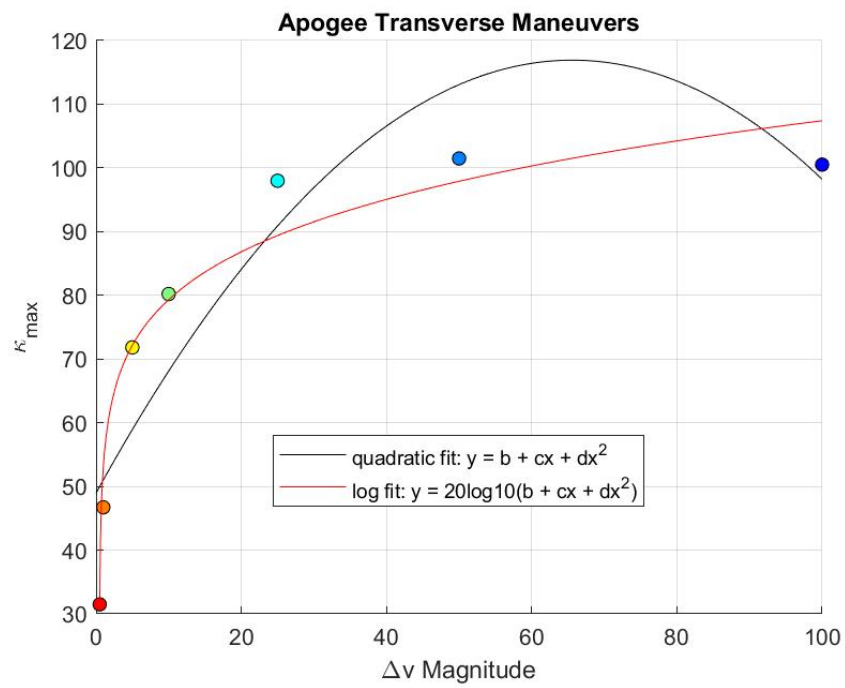


Figure 4.16: Variation of K (κ_{\max}) with transverse apogee maneuvers of varying Δv (m/s) for the first Orbital Case with $\eta_{th} = 0.1$.

4.2.6 Variation of K with Maneuver Duration

In this near final set of simulations, the Section 4.2.1 maneuvers are applied at the perigee and apogee of the Case 1 orbital geometry of previous sections. The maneuver duration is varied in two cases: 1) $t_{man} = 10$ seconds; and, 2) $t_{man} = 1000$ seconds. In all previous simulations, the maneuvering thrust duration was set as $t_{man} = 100$ seconds. With apogee transverse maneuvers as the direction and location of interest, only these results are illustrated. Results for perigee maneuvers and the corresponding tabulated results for the curve fits of these scenarios can be found in Appendix D (Tables D.6 and D.7); while results for Ψ are included in Appendix E for reference.

In the first case ($t_{man} = 10$ seconds, Figure 4.17), the K- Δv relationship is inconsistent with the previous results, showing only a straight line at a constant K-value near K_{th} , which is likely analogous to the default detection output of this case with no applied maneuvers (see Appendix B with discussion in Sections 3.3.2 and 4.2.1). The coefficients of the curve fits (Table D.6) make this apparent, where the v_0^2 term is near the default parameter output value. This is justifiable, as $t_{man} = 10$ seconds is quite fast and may not truly be practical with current engines [62]. Thus, with such a fast duration, almost no change is affected in the overall velocity, such that almost no change is observed in K. This is supported by the near zero Δv and Δv^2 coefficients, indicating nearly no variance nor relationship to these terms, such that $\Delta v \approx 0$, and hence, $b \approx K_{th}$. This implies a possible limitation of K, where maneuvers may need to be near at least 100 seconds ($t_{man} \sim 10^2$) for any discernible relationship, though further tests would be necessary to make a concrete conclusion.

For the second case ($t_{man} = 1000$ seconds, Figure 4.18) the relationship for apogee maneuvers follow the same expected general trend, where the magnitude of K increases with increasing Δv in a nonlinear fashion. This is a promising result for developing relationships with longer duration maneuvers. However, for these maneuvers at the perigee (see Appendix D and fig. D.7), the results seem to be erroneous, where no discernible relationship can be deduced, indicating that a maneuvering time of 1000 seconds is too long for an accurate detection or relationship to be obtained for perigee maneuvers. This alludes to another possible limitation of the detection parameters, necessitating further tests. This supports the notion that that maneuver duration has an impact on the detection and predicted characterisation of maneuvers.

For both cases, it is possible that tuning the Ψ and η thresholds could assist in the detection of longer and shorter duration maneuvers, and further tests would be required.

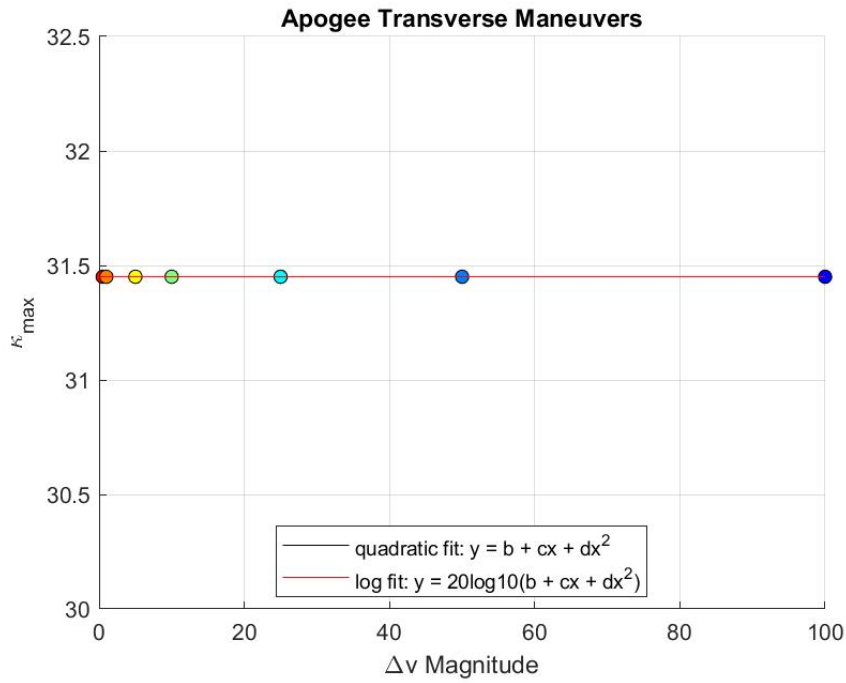


Figure 4.17: Variation of K (κ_{\max}) with Transverse Apogee Maneuvers of varying Δv (m/s) for the first Orbital Case with $t_{man} = 10$ seconds.

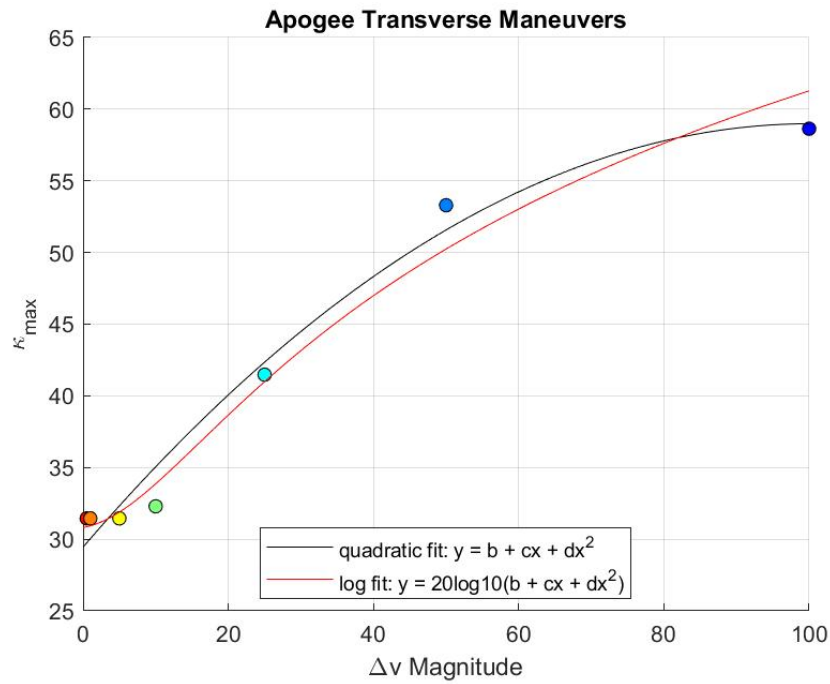


Figure 4.18: Variation of K (κ_{\max}) with Transverse Apogee Maneuvers of varying Δv (m/s) for the first Orbital Case with $t_{man} = 1000$ seconds.

4.2.7 Variation of K with Small-Scale Δv 's

For all previous cases, it is important to note that all maneuvers were of m/s scale. However, it is possible for maneuvers to occur at smaller scales, for example, in the cm/s range. In this section, maneuvering thrust magnitudes in the cm/s range are explored for velocities varied discretely from 1 cm/s to 100 cm/s.

In order to accomplish this, it was found that the Ψ_{th} and η_{th} values required some tuning, such that a detection could be consistently determined by the Ψ and K parameters. Setting $\Psi_{th} = 10$ ($\therefore K_{th} \approx 21$) and $\eta_{th} = 0.1$ was found to yield results of similar consistency to the larger magnitude Δv cases (on the m/s scale) explored in the preceding sections of this chapter. Modifying these thresholds supports suggestions in prior sections that modifications would be necessary for certain cases.

For the apogee transverse maneuvers (Figure 4.19), the overall expected trend of previous sections is observed, where the detection parameter maximum increases with increasing Δv , and is easily visible as shown by Figure 4.21. Thus, the parameters are able to consistently detect maneuvers even on this smaller magnitude scale. At the same time, for perigee maneuvers (Figure 4.20), a trend is less easily determined. If the first test point were to be removed ($\Delta v = 0.5$ cm/s), the same general trends with better curve fit relationships would likely exist. This means that at perigee, the smaller maneuvers are harder for the parameter to accurately detect — which is supported by the lower peak among other peaks near the threshold shown in Figure 4.22 — and consequently for an accurate relationship to be obtained, which is consistent with discussions in the previous sections as well, concerning smaller maneuver magnitudes. It is possible other values of Ψ_{th} and η_{th} would assist in detections of maneuvers on the even smaller scale, especially for perigee, where other peaks past the threshold are visible, which could influence false detections. At the same time, spacecraft velocity is greatest at the orbital perigee, which alludes to the requirement for larger Δv maneuvers to be applied for a noticeable orbital change to occur. The the final orbital elements for the two presented cases are tabulated in Table 4.12, supporting that such small maneuvers incur minimal change, and is included for reference.

Another interesting observation of this case is that the curve fit relationships show very little dependence on the Δv and Δv^2 terms, some of which are negative, for maneuvers applied in the normal direction. At the same time, radial and transverse maneuvers applied at apogee depend greatly on Δv^2 , with a coefficient on the order of magnitude of 10^2 , which is larger than and inconsistent with most tested cases. Further analyses on the cm/s scale may be useful in assisting to solidify relationships between K and Δv , as these results pose counterintuitive conclusions in comparison to the

previous sections based on analysis of the curve fit coefficients. On the other hand, for perigee maneuvers, the trends in the coefficients of the curve fit relationships are generally consistent with previous results overall: greatest dependence is observed on v_0^2 , and weakest dependence is observed on Δv^2 , with focus on the logarithmic fit.

In addition, from inspecting the graphs, it is noticed that the variation in K is smaller than in previous cases. For apogee maneuvers the variation ranges from $21 < K < 46$, and is $21 < K < 22$ for perigee maneuvers. This supports the notion that small maneuvers both in general (and applied at perigee in particular) will have decreased effects on the variation of K , as these maneuvers will be orders of magnitude even smaller than the operating v_0 of the spacecraft.

Table 4.12: Initial and Final Orbital Elements and Orbital Energy for for Δv in the cm/s Range

$\Delta v = 5$ (cm/s)	Location	a (km)	e	i (°)	Ω (°)	ω (°)	ν (°)	ϵ (km ² /s ²)
Initial (Case 1)	—	8 107.84	0.09000	0	0	0	0	-24.58
Final (Figure 4.21)	Apogee	8 108.10	0.08996	0	0	0.00205	5.85	-24.58
Final (Figure 4.22)	Perigee	8 108.21	0.09004	0	0	0.00307	5.82	-24.58

Table 4.13: Coefficients for the Curve Fit Lines of the K - Δv Relationship in the cm/s Range for the First Orbital Case with $\Psi_{th} = 10$ and $\eta_{th} = 0.1$

Perigee						
	Quadratic $y = b + cx + dx^2$			Logarithmic $y = 20 \log_{10}(b + cx + dx^2)$		
	b	c	d	b	c	d
Radial	21.8017	5.7870	-3.7443	12.2506	9.3672	-6.0455
Transverse	21.8444	-0.8447	1.0225	12.3640	-1.1825	1.4415
Normal	22.3267	-0.6406	2.7946	13.0947	-1.6050	5.3681

Apogee						
	Quadratic $y = b + cx + dx^2$			Logarithmic $y = 20 \log_{10}(b + cx + dx^2)$		
	b	c	d	b	c	d
Radial	20.2600	21.1746	5.7709	12.7318	-47.7166	249.3969
Transverse	20.7902	10.8329	15.0671	13.5088	-56.4986	227.0109
Normal	21.3362	-4.8765×10^{-07}	4.3069×10^{-07}	11.6630	1.2635^{-09}	-8.5542^{-10}

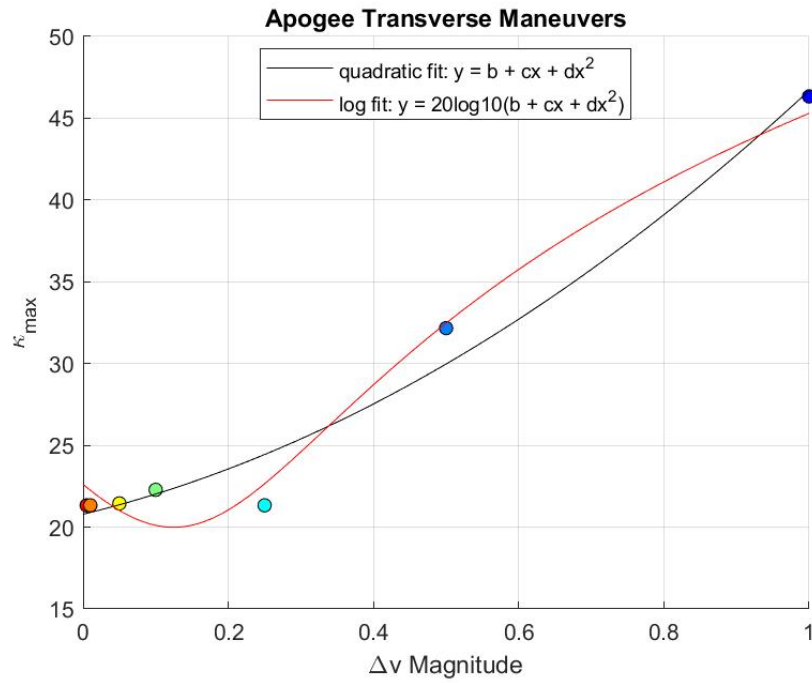


Figure 4.19: Variation of K (κ_{\max}) with transverse apogee maneuvers of varying Δv (m/s) in the cm/s range for the first Orbital Case with $\Psi_{th} = 10$ and $\eta_{th} = 0.1$.

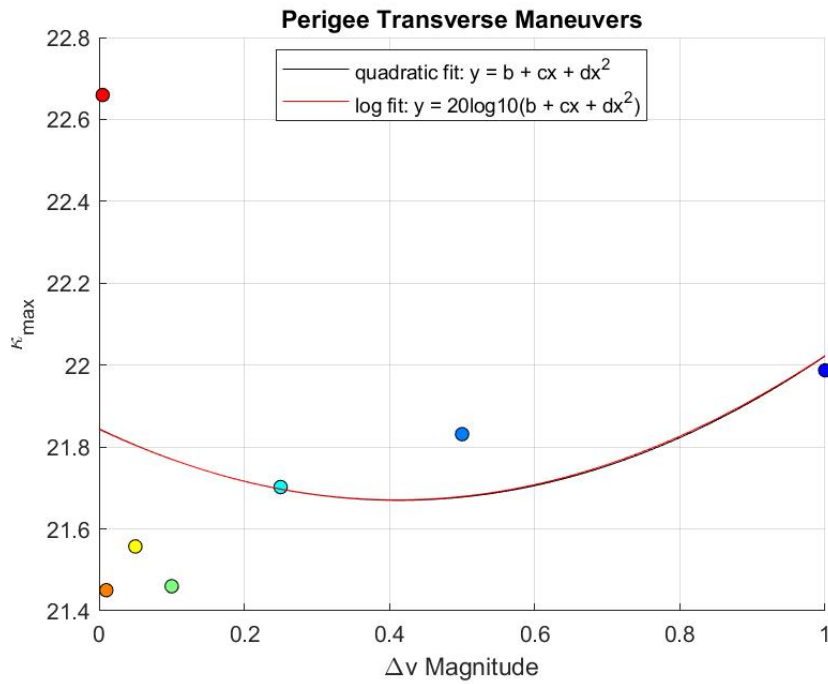


Figure 4.20: Variation of K (κ_{\max}) with transverse apogee maneuvers of varying Δv (m/s) in the cm/s range for the first Orbital Case with $\Psi_{th} = 10$ and $\eta_{th} = 0.1$.

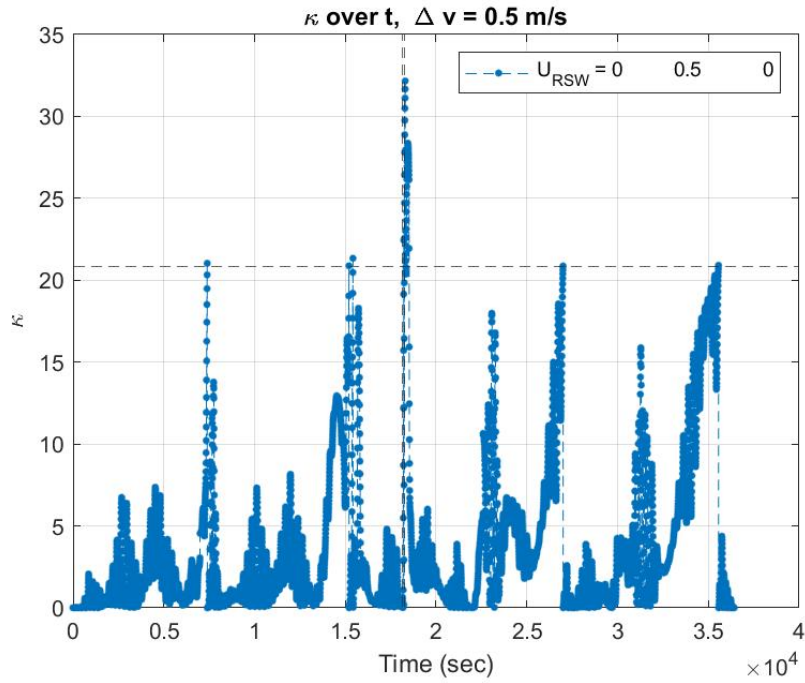


Figure 4.21: Transverse apogee κ vs. time for $\Delta v = 0.05 \text{ m/s} = 5 \text{ cm/s}$; $\kappa_{max} = 46.7961$, at $t = 18\,450$ seconds ($\Psi_{th} = 10$, $\eta_{th} = 0.1$).

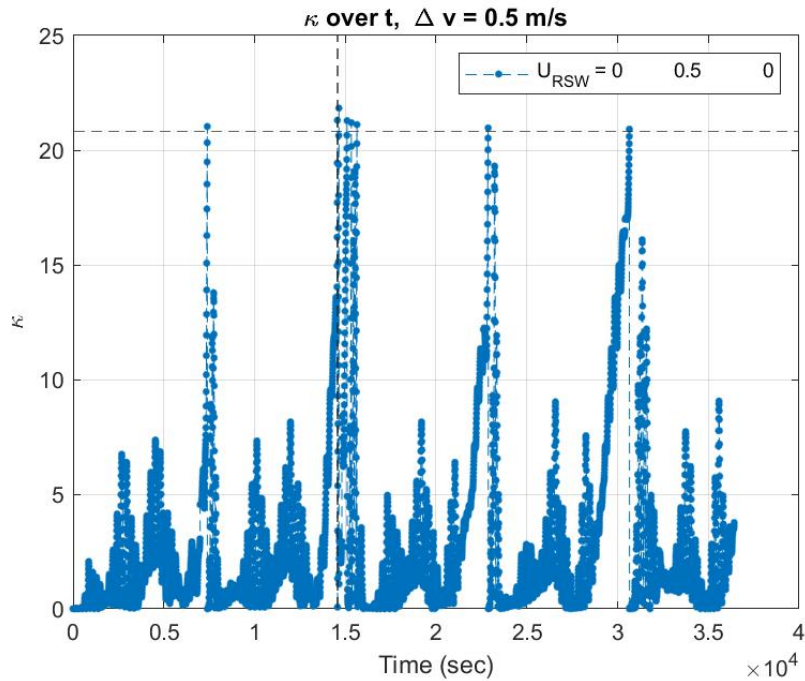


Figure 4.22: Transverse perigee κ vs. time for $\Delta v = 0.05 \text{ m/s} = 5 \text{ cm/s}$; $\kappa_{max} = 24.8591$, at $t = 14\,855$ seconds ($\Psi_{th} = 10$, $\eta_{th} = 0.1$).

CHAPTER 5

Conclusions and Future Work

5.1 Conclusions and Final Key Points

Through an extensive review process, it was determined that the methods proposed by Goff et al. [41] provided the best foundation to achieve the goals of this thesis. Being able to define and utilise a single parameter to determine the occurrence of an unknown event was of high interest, as it alludes to a simple and consistent method of maneuver detection without complicated processing prior to maneuver detection. The method proposed by Goff et al. [41] included an IMM process to handle multiple sensor data, which can add a layer of complexity, increasing computational demand. Hence, the goal was to add to the work of Goff et al. [41], by implementing a single parameter detection method that can easily detect and relate to maneuvers from single-sensor data. Furthermore, the work by Goff et al. [41] alluded to a preliminary relationship between the detection parameter and the maneuvering velocity, but does not include a method for characterising maneuvers, which supports the need to determine analytical relationships with maneuvering velocity in terms of both magnitude and direction, accompanying the aforementioned goal.

This dissertation proposes a possible improvement to the method presented by Goff et al. [41], by using the same concept for a single detection parameter to identify maneuvers, and consequently develop a preliminary relationship between the parameter (K , as well as Ψ) and the applied maneuvering magnitudes (Δv). The method proposed utilises the same base detection parameter (Ψ) and inflation covariance protocol, and builds onto the quadratic relationship between the original Ψ parameter and Δv magnitudes applied, where the new detection parameter (K) places the detection magnitudes into a decibel scale while eliminating any large magnitude anti-peaks in the K results when observed over time. This is helpful in determining event occurrence by result observation as the peaks in K can be more prominent than in Ψ observed over time, though some maneuvering scenarios may favour the use of the original Ψ parameter in a linear scale for better detection. In terms of the K - Δv and Ψ - Δv relationships, it was found that in general, as the maneuvering Δv magnitude increased, the magnitudes of K and Ψ also increased. These relationships were found to be

nonlinear due to included dependence on the square of the maneuvering velocity (Δv^2), fitting best with either a quadratic (for Ψ) or logarithm of the quadratic (for K) relationships with indications to the ranges of the variation in K per applied maneuver direction or location. The possible procedure an operator could follow to implement and utilise the new parameter was also outlined (Section 4.2.1), along with inference to indicators of maneuvering type and details based on the variations in K through results of the several tested scenarios.

The chosen filtering technique was the same as that of Goff et al. [41] with added amendments, and it was decided to manually implement the code for ease of use, as opposed to manipulating the existing EKF protocol in MATLAB after some attempts. Future work to build on this dissertation can include further testing with presented cases, as well as application to simulations of break-up or berthing events, multiple maneuvering scenarios, multiple sensors and other site locations or space-based sensing, the inclusion of natural perturbations, and implementation with the existing MATLAB protocol, which are discussed further in Section 5.2.

Overall, this work was successful in exploring and developing a method for maneuver detection, and establishing the nonlinear relationship between maneuver detection parameters and the maneuvering Δv magnitude, all while maintaining low computational demands. The success of this work could be extended to small satellite operators that may not be as computationally rich as large space agencies or companies, only having limited resources for SSA algorithms. With a simpler, less computationally demanding base method, extensions can then be applied for multi-sensor use and determination, or other case scenarios.

5.2 Possibilities for Future Work

Though several cases were tested in this research, there are still several more testing scenarios possible, as indicated in several discussions within Chapter 4. Most test cases only considered the relationships between the detection parameter and Δv for one orbital geometry and orientation in the Low Earth Orbit (LEO) regime. More simulations of the outlined test scenarios should be conducted for multiple orbital types to obtain complete and more concrete relationships. Additionally, other orbital regimes should be explored, testing if the relationships proposed remain consistent. For further detail, an exploration on the affects of maneuvering direction and orbital energy could be explored for further assistance in establishing concrete maneuver detection and characterisation relationships.

As shown in Section 3.3.1, the calculation of K was applied after the EKF as a simple post processing procedure. However, the original detection parameter, Ψ , was calculated within the EKF protocol. Thus, K could be implemented at the same step for a real-time result. It would be interesting to observe how implementation in this manner could impact maneuver characterisation, and if Ψ and K could be used in conjunction to minimise false detections or obtain rapid real-time predictions for characterising detected maneuvers. This would test the implementation of established relationships between K and Δv in another fashion for robust solutions to be used by operators.

Furthermore, only the case of single maneuver detection was explored. In the future, spacecraft that undergo multiple maneuvers could be explored as well. A preliminary test of this scenario was tested (though not presented), and the results seemed promising with the current work. With increasing needs in space defense, this is a valuable and pertinent area of exploration.

In addition, simulations only included data coming from one sensor and fixed site location on the Earth. In reality, operators may receive data from multiple sensors or site locations, or from space-based sensors. Kalman Filters are able to incorporate and fuse data from multiple sensors. Hence, this would be another useful extension of efforts and apply to more realistic cases.

This dissertation only explored cases for satellites that maneuver and stay as one whole satellite. With the increasing risk of collisions and thus possibilities for break-up events, this would be another pertinent area to explore. In the same vein, with increases in space launches and satellite ridesharing, berthing events would be another compelling area to explore. In these cases, one observed spacecraft becomes multiple, and could highlight interesting relationships between maneuver detection and maneuver magnitudes. At the same time, it is possible for a spacecraft to rendezvous another, which could be another interesting case to explore.

Lastly, since MATLAB already has an existing EKF protocol, among other KF algorithms, it would be valuable and desirable to be able to implement the work for this dissertation to function with indicated algorithms. Being able to implement this work with the available MATLAB protocol would allow for ease of use, implementation and accessibility for operators interested in using these methods.

APPENDIX A: FULL FILTERING PROCESS STEPS

This EKF process is based on [41] and [53,57] as discussed in Section 3.1.

1. Read and Define observation information:

$$\mathbf{y}_i, \mathbf{R}_i$$

2. Read or Define State and process information:

$$\hat{\mathbf{P}}_{i-1}, \hat{\mathbf{x}}_{i-1}, \Phi(t_{i-1}, t_{i-1}) = \mathbf{I}, \mathbf{Q}_i$$

3. Propagate State information to obtain State prediction and STM; $\bar{\mathbf{x}}_{\mathbf{F}_i}, \Phi(t_i, t_{i-1})$:

$$t_{i-1} \rightarrow t_i$$

$$\bar{\mathbf{x}}_{\mathbf{F}_i} = \int (\dot{\mathbf{x}} = \mathbf{f}(\mathbf{x}, t))_i$$

$$\Phi_i = \int \left(\dot{\Phi} = \left(\frac{\mathbf{f}(\mathbf{x}, t)}{d\mathbf{x}} \right) \Phi(t_i, t_{i-1}) \right)_i$$

4. Apply Mapping Process to $\bar{\mathbf{x}}$ (Section 3.2):

$$\bar{\mathbf{x}}_{\mathbf{F}_i} = \begin{bmatrix} \mathbf{C}_{\mathbf{FI}}(t_i) & \mathbf{0} \\ \dot{\mathbf{C}}_{\mathbf{FI}}(t_i) & \mathbf{C}_{\mathbf{FI}}(t_i) \end{bmatrix} \bar{\mathbf{x}}_{\mathbf{I}_i}, \quad \rho_{\mathbf{F}_i} = \rho_{\mathbf{F}_i}(\bar{\mathbf{x}}_{\mathbf{F}_i}), \quad \rho_{\mathbf{S}_i} = \begin{bmatrix} \mathbf{C}_{\mathbf{SF}} & \mathbf{0} \\ \mathbf{0} & \mathbf{C}_{\mathbf{SF}} \end{bmatrix} \rho_{\mathbf{F}_i}$$

5. Define and build State estimate in terms of observation data elements (Section 3.2):

$$\hat{\mathbf{y}}_i = \begin{bmatrix} \rho & \beta & el & \dot{\rho} \end{bmatrix}^\top$$

6. Build H-partials Matrix (Section 3.2):

$$\mathbf{H}_i = \frac{\partial \hat{\mathbf{y}}}{\partial \rho_{\mathbf{S}}} \frac{\partial \rho_{\mathbf{S}}}{\partial \rho_{\mathbf{F}}} \frac{\partial \rho_{\mathbf{F}}}{\partial \mathbf{x}_{\mathbf{F}}} \frac{\partial \mathbf{x}_{\mathbf{F}}}{\partial \mathbf{x}_{\mathbf{I}}}$$

7. Calculate State Covariance prediction:

$$\bar{\mathbf{P}}_i = \Phi(t_i, t_0) \hat{\mathbf{P}}_{i-1} \Phi(t_i, t_0)^\top + \mathbf{Q}_i$$

8. Calculate filtering residuals to reference orbit:

$$\boldsymbol{\nu}_{e_i} = \mathbf{y}_i - \hat{\mathbf{y}}$$

9. Calculate Observation Covariance:

$$\mathbf{S}_i = \mathbf{H}_i \bar{\mathbf{P}}_i \mathbf{H}_i^\top + \mathbf{R}_i$$

10. Calculate Ψ Detection Parameter:

$$\Psi_i = \boldsymbol{\nu}_{e_i}^\top (\mathbf{S}_i)^{-1} \boldsymbol{\nu}_{e_i}$$

11. Calculate Kalman Gain Matrix:

$$\mathbf{K}_i = \bar{\mathbf{P}}_i \mathbf{H}_i^\top (\mathbf{S}_i)^{-1}$$

12. Calculate update to obtain State and State Covariance estimates:

$$\hat{\mathbf{x}}_i = \bar{\mathbf{x}}_i + \mathbf{K}_i \boldsymbol{\nu}_{e_i}$$

$$\hat{\mathbf{P}}_{i-1} = (\mathbf{I} - \mathbf{K}_i \mathbf{H}_i) \bar{\mathbf{P}}_i$$

13. Perform Ψ -check and Covariance Inflation:

$$\Psi_i > \Psi_{th} \rightarrow \text{Inflation check:}$$

$$\text{tr}(\hat{\mathbf{P}}_i) < \eta_{th} \rightarrow \hat{\mathbf{P}}_i = 10 \hat{\mathbf{P}}_i$$

14. Perform Process Noise Covariance Inflation (per Table 3.1):

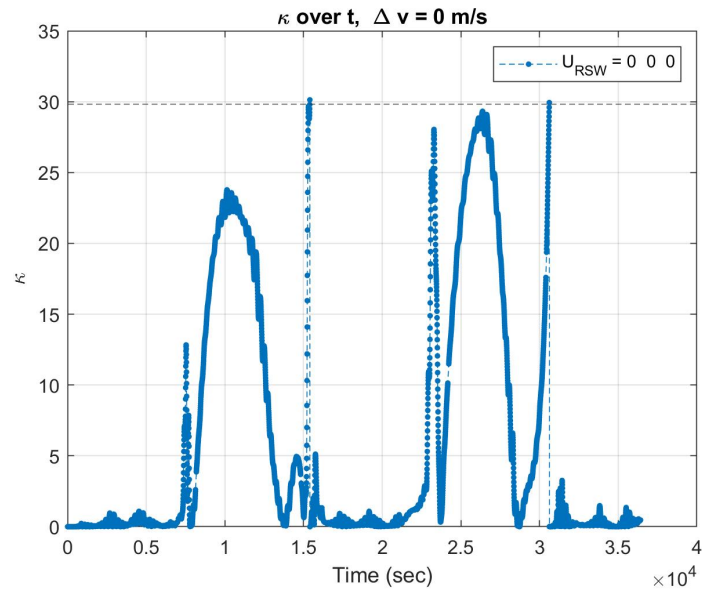
$$\mathbf{Q}_i = \begin{bmatrix} q_{r_i} \mathbf{I} & \mathbf{0} \\ \mathbf{0} & q_{v_i} \mathbf{I} \end{bmatrix}$$

15. Repeat Steps 1 to 14 with new $\hat{\mathbf{x}}_i$, $\hat{\mathbf{P}}_i$, \mathbf{Q}_i

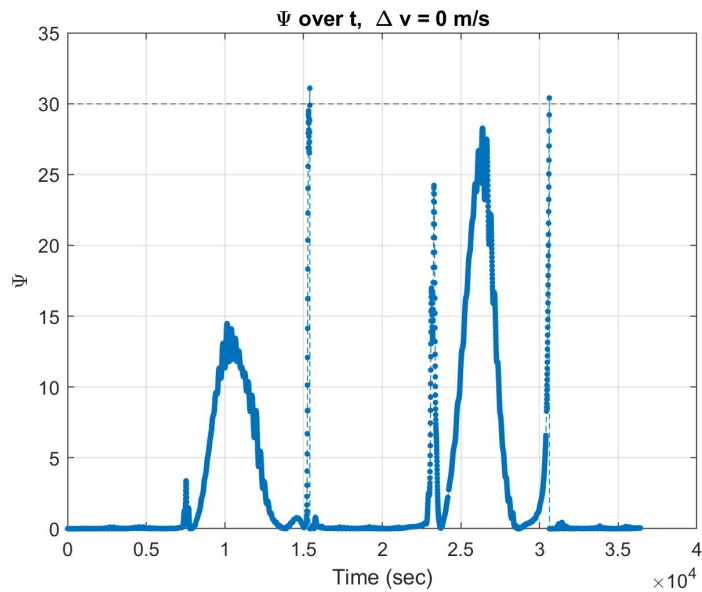
16. Apply new K detection calculation to all Ψ values (there is possibility for this to be implemented in Step 10 and accumulated after the Ψ calculation, but further investigation is necessary):

$$K = 20 \log_{10}(\Psi + 1)$$

APPENDIX B: NO MANEUVER BASE RESULT



(a)



(b)

Figure B.1: Base filtering results of K and Ψ for no applied maneuvers; $K_{max} = 30.127$ and $\Psi_{max} = 31.089$ at $t = 15\ 400$ seconds.

APPENDIX C: QUALITATIVE SUMMARIES

Table C.1: Summary of $K-\Delta v$ Relationship for Most Pertinent Tests

Apogee Man			Perigee Man		
	Range of K	Logarithmic comments $y = 20 \log_{10}(b + cx + dx^2)$		Range of K	Logarithmic comments $y = 20 \log_{10}(b + cx + dx^2)$
Radial	30 <K <90 Largest Variation	Greatest dependence on c both overall and per direction Negative b Weaker dependence on d Largest coefficient values overall Largest variance in K-range	Radial	30 <K <51	Greatest dependence on b both overall and per direction Negative b Weaker dependence on d
Transverse	30 <K <85	Greater dependence on c Weaker dependence on d	Transverse	30 <K <47	Greater dependence on b Weakest dependence on d overall
Normal	30 <K <45	Greater dependence on b Negative c Weakest dependence on d overall Most consistent relationship with subsequent cases	Normal	31 <K <49	Greater dependence on b Negative c Weaker dependence on d

Quarter of an Orbit after Apogee			Quarter of an Orbit after Perigee		
	Range of K	Logarithmic comments $y = 20 \log_{10}(b + cx + dx^2)$		Range of K	Logarithmic comments $y = 20 \log_{10}(b + cx + dx^2)$
Radial	30 <K <50	Greatest dependence on b both overall and per direction Negative c Weaker dependence on d	Radial	31 <K <53	Greater dependence on b Weaker dependence on d
Transverse	30 <K <70	Greater dependence on b Weaker dependence on d overall	Transverse	30 <K <60	Greatest dependence on b both overall and per direction Negative c Weaker dependence on d
Normal	31 <K <33 Smallest Variation	Greater dependence on b Small c on similar order to d Weakest dependence on d overall Smallest variance in K-range	Normal	31 <K <43	Greater dependence on b Negative d Weakest dependence on d

Apogee Man Case 2			Perigee Man Case 2		
	Range of K	Logarithmic comments $y = 20 \log_{10}(b + cx + dx^2)$		Range of K	Logarithmic comments $y = 20 \log_{10}(b + cx + dx^2)$
Radial	30 <K <70	Greatest dependence on b both overall and per direction Negative c Weakest dependence on d	Radial	31 <K <49	Greater dependence on b Negative d Weaker dependence on d Anomaly at $\Delta v = 50$ m/s, else variation would be 31 < K < 45
Transverse	30 <K <39	Greater dependence on b Weaker dependence on d	Transverse	30 <K <70	Greater dependence on b Negative d Weaker dependence on d
Normal	30 <K <73	Greater dependence on b Negative c Weaker dependence on d	Normal	30 <K <45	Greatest dependence on b both overall and per direction Negative d Weakest dependence on d

APPENDIX D: FURTHER TEST CASE RESULTS

D.1 Variation in Measurement Noise Covariance

Table D.1: Coefficients for Curve Fit Lines of the $K-\Delta v$ Relationship for Maneuvers Applied to the First Orbital Case with $\mathbf{R} = 10\mathbf{R}$

	Perigee					
	Quadratic $y = b + cx + dx^2$			Logarithmic $y = 20 \log_{10}(b + cx + dx^2)$		
	b	c	d	b	c	d
Radial	29.8466	0.3323	-0.00006416	39.3434	-1.6154	0.1220
Transverse	16.4436	3.0313	-0.02582	51.4830	-16.5070	2.2429
Normal	32.5980	0.1455	0.0002462	40.4518	0.9560	0.01301

	Apogee					
	Quadratic $y = b + cx + dx^2$			Logarithmic $y = 20 \log_{10}(b + cx + dx^2)$		
	b	c	d	b	c	d
Radial	31.0509	2.0385	-0.01363	14.1845	-10.6937	13.0489
Transverse	34.1347	1.2505	-0.006954	-10.6593	44.5899	1.7214
Normal	19.2349	0.5999	-0.002783	10.9665	-0.07235	0.04534

Table D.2: Coefficients for Curve Fit Lines of the $K-\Delta v$ Relationship for Maneuvers Applied to the First Orbital Case with $\mathbf{R} = \mathbf{R}/10$

	Perigee					
	Quadratic $y = b + cx + dx^2$			Logarithmic $y = 20 \log_{10}(b + cx + dx^2)$		
	b	c	d	b	c	d
Radial	32.2048	0.3305	-0.0007745	41.3952	1.1477	0.05345
Transverse	31.6454	0.3932	-0.001950	35.1306	2.8321	0.006256
Normal	34.9705	0.1886	0.0007809	69.5088	-2.4769	0.1241

	Apogee					
	Quadratic $y = b + cx + dx^2$			Logarithmic $y = 20 \log_{10}(b + cx + dx^2)$		
	b	c	d	b	c	d
Radial	33.1228	0.6123	-0.003639	37.7550	6.7726	0.01568
Transverse	32.9230	1.04829	-0.005662	36.6849	4.8364	1.01634
Normal	31.6855	0.06656	-0.0003007	38.3265	0.3214	-0.001195

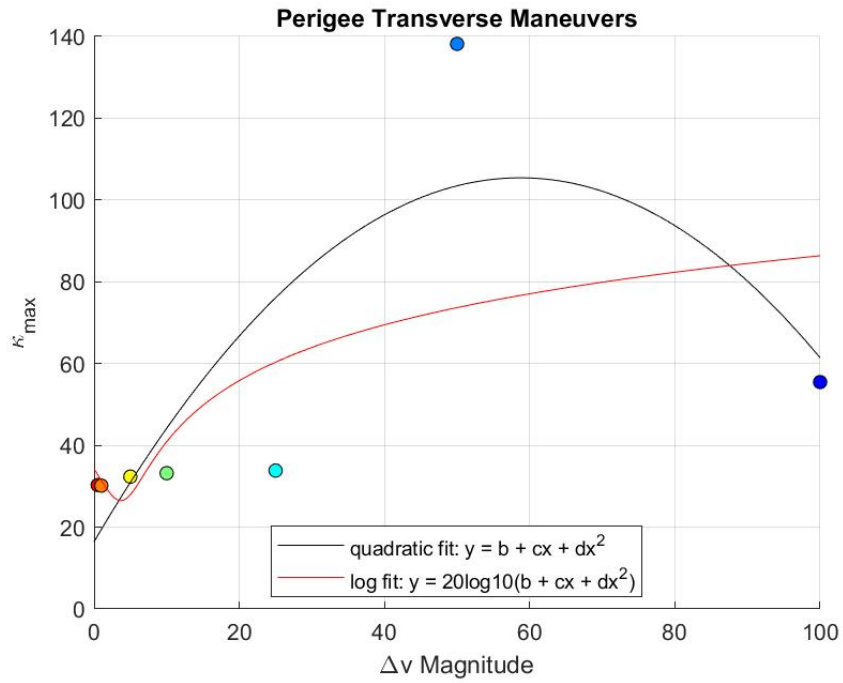


Figure D.1: Variation of K (κ_{\max}) with transverse perigee maneuvers of varying Δv (m/s) for the first Orbital Case with $\mathbf{R} = 10\mathbf{R}$.

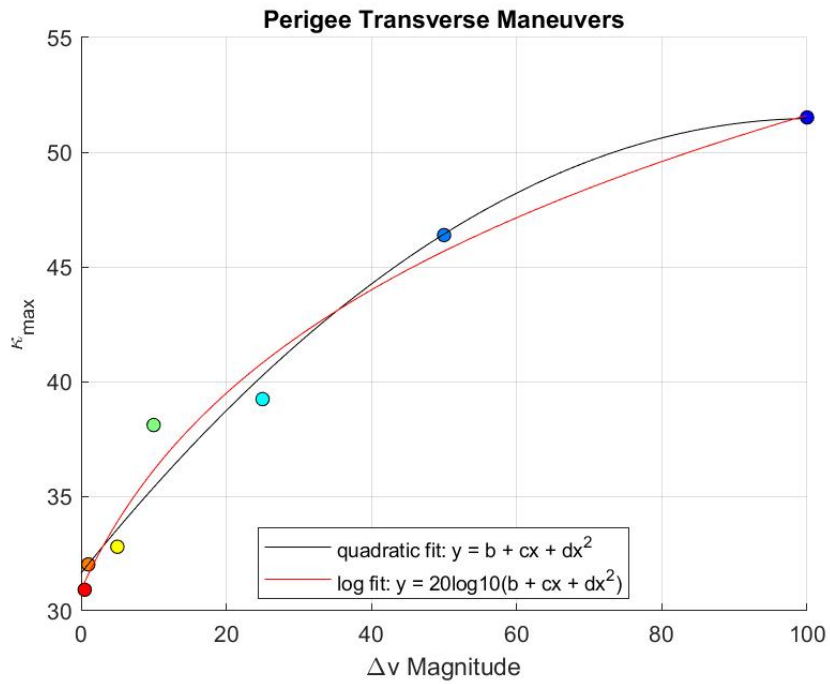


Figure D.2: Variation of K (κ_{\max}) with transverse perigee maneuvers of varying Δv (m/s) for the first Orbital Case with $\mathbf{R} = \mathbf{R}/10$.

D.2 Variation in Ψ and η Thresholds

Table D.3: Coefficients for Curve Fit Lines of the $K-\Delta v$ Relationship for Maneuvers Applied in the First Orbital Case with $\Psi_{th} = 10$

Perigee						
	Quadratic $y = b + cx + dx^2$			Logarithmic $y = 20 \log_{10}(b + cx + dx^2)$		
	b	c	d	b	c	d
Radial	21.5310	0.5604	-0.002574	13.4670	0.2297	0.04198
Transverse	22.3863	0.2243	0.0002361	14.5230	-0.1145	0.02023
Normal	23.8234	0.3512	-0.0008171	17.3971	0.005315	0.03227

Apogee						
	Quadratic $y = b + cx + dx^2$			Logarithmic $y = 20 \log_{10}(b + cx + dx^2)$		
	b	c	d	b	c	d
Radial	29.3968	1.8226	-0.01288	1.8633	18.2847	3.1166
Transverse	28.8241	1.4585	-0.01020	-3.1182	27.6177	0.4199
Normal	21.4546	0.1930	0.00005035	12.5925	0.01685	0.01013

Table D.4: Coefficients for Curve Fit Lines of the $K-\Delta v$ Relationship for Maneuvers Applied the First Orbital Case with $\Psi_{th} = 100$

Perigee						
	Quadratic $y = b + cx + dx^2$			Logarithmic $y = 20 \log_{10}(b + cx + dx^2)$		
	b	c	d	b	c	d
Radial	41.6476	0.0895	0.0006081	118.3562	1.2338	0.03686
Transverse	42.4253	0.2045	-0.0009702	123.6157	5.0505	-0.01822
Normal	43.2556	0.1104	-0.0001722	140.6565	2.6074	0.0009403

Apogee						
	Quadratic $y = b + cx + dx^2$			Logarithmic $y = 20 \log_{10}(b + cx + dx^2)$		
	b	c	d	b	c	d
Radial	40.7810	1.0432	-0.005966	119.0851	-1.6129	2.4392
Transverse	28.4328	3.4693	-0.02896	265.2980	-187.4138	31.1539
Normal	40.2001	0.1011	-0.0005599	102.2277	1.3348	-0.006285

Table D.5: Coefficients for Curve Fit Lines of the K - Δv Relationship for Maneuvers Applied the First Orbital Case with $\eta_{th} = 0.1$

Perigee						
	Quadratic $y = b + cx + dx^2$			Logarithmic $y = 20 \log_{10}(b + cx + dx^2)$		
	b	c	d	b	c	d
Radial	29.8573	0.9501	-0.005175	34.6704	0.07479	0.5207
Transverse	32.1711	0.7860	-0.003813	38.7328	3.1336	0.3687
Normal	29.3335	0.6578	-0.003041	37.7427	-1.2857	0.2173

Apogee						
	Quadratic $y = b + cx + dx^2$			Logarithmic $y = 20 \log_{10}(b + cx + dx^2)$		
	b	c	d	b	c	d
Radial	53.0094	2.0438	-0.01591	-921.9259	1919.0585	-2.5311
Transverse	48.9655	2.0718	-0.01579	-371.9054	807.0640	15.4323
Normal	29.5032	0.5568	-0.002246	37.3095	-1.0182	0.1627

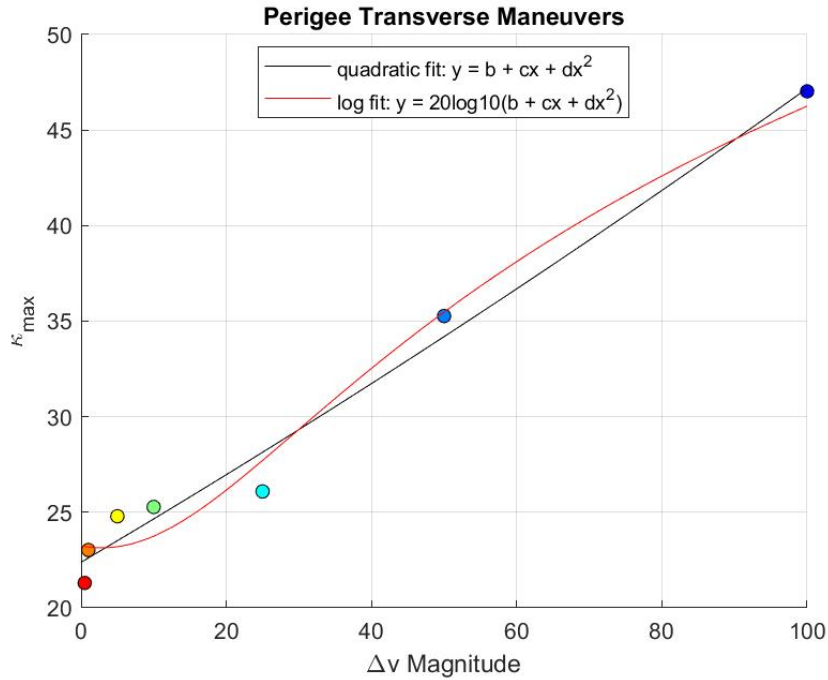


Figure D.3: Variation of K (κ_{\max}) with transverse perigee maneuvers of varying Δv (m/s) for the first Orbital Case with $\Psi_{th} = 10$.

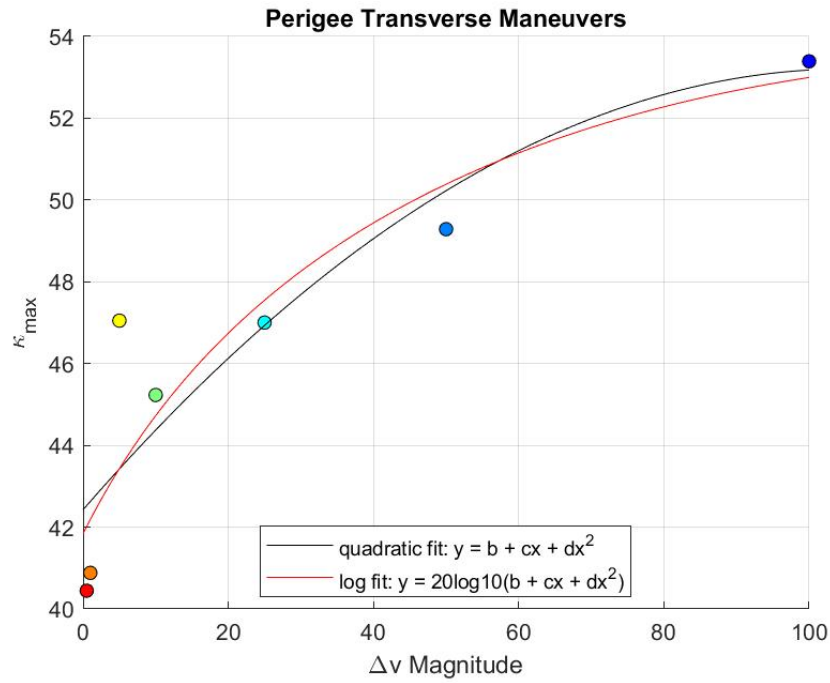


Figure D.4: Variation of K (κ_{\max}) with Transverse Perigee Maneuvers of varying Δv (m/s) for the first Orbital Case with $\Psi_{th} = 100$.

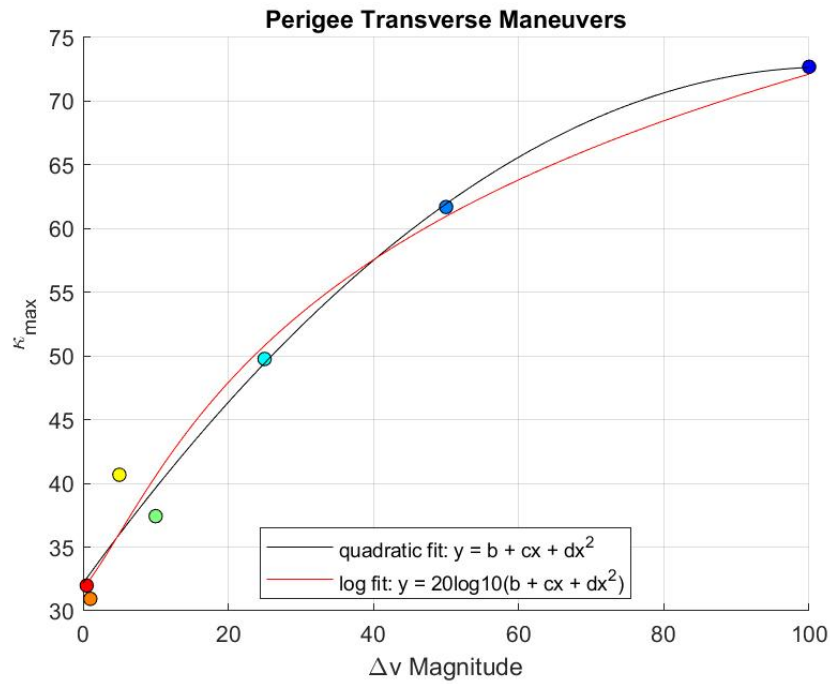


Figure D.5: Variation of K (κ_{\max}) with Transverse Perigee Maneuvers of varying Δv (m/s) for the first Orbital Case with $\eta_{th} = 0.1$.

D.3 Variation in Maneuvering Duration

Table D.6: Coefficients for Curve Fit Lines of the $K-\Delta v$ Relationship for Maneuvers Applied in the First Orbital Case with $t_{man} = 10$ seconds

Perigee						
	Quadratic $y = b + cx + dx^2$			Logarithmic $y = 20 \log_{10}(b + cx + dx^2)$		
	b	c	d	b	c	d
Radial	30.6572	-0.006445	0.00002683	34.1085	-0.02516	0.0001071
Transverse	30.5031	0.007568	-0.00006713	33.5005	0.03019	-0.0002678
Normal	30.4248	-0.005986	0.00004789	33.2060	-0.02254	0.0001801

Apogee						
	Quadratic $y = b + cx + dx^2$			Logarithmic $y = 20 \log_{10}(b + cx + dx^2)$		
	b	c	d	b	c	d
Radial	31.4506	-1.8531×10^{-17}	3.0408×10^{-19}	37.3707	3.9433×10^{-16}	-3.4953×10^{-18}
Transverse	31.4506	-5.9364×10^{-17}	6.1872×10^{-19}	37.3707	1.3742×10^{-16}	-1.4649×10^{-18}
Normal	31.4506	1.0797×10^{-17}	2.3296×10^{-19}	37.3707	3.8066×10^{-16}	-4.6939×10^{-18}

Table D.7: Coefficients for Curve Fit Lines of the $K-\Delta v$ Relationship for Maneuvers Applied in the First Orbital Case with $t_{man} = 1000$ seconds

Perigee						
	Quadratic $y = b + cx + dx^2$			Logarithmic $y = 20 \log_{10}(b + cx + dx^2)$		
	b	c	d	b	c	d
Radial	34.5977	0.2875	-0.001694	50.3754	2.9058	-0.01305
Transverse	35.4383	0.3215	-0.002140	59.3274	3.0385	-0.01501
Normal	30.2060	0.2311	0.00005453	39.8329	-1.1565	0.06120

Apogee						
	Quadratic $y = b + cx + dx^2$			Logarithmic $y = 20 \log_{10}(b + cx + dx^2)$		
	b	c	d	b	c	d
Radial	29.8168	0.5985	-0.002561	36.6241	-0.3647	0.1765
Transverse	29.4469	0.5896	-0.002943	34.7140	0.3762	0.1086
Normal	55.2973	-0.0508	-0.002301	915.9655	-26.3132	0.1752

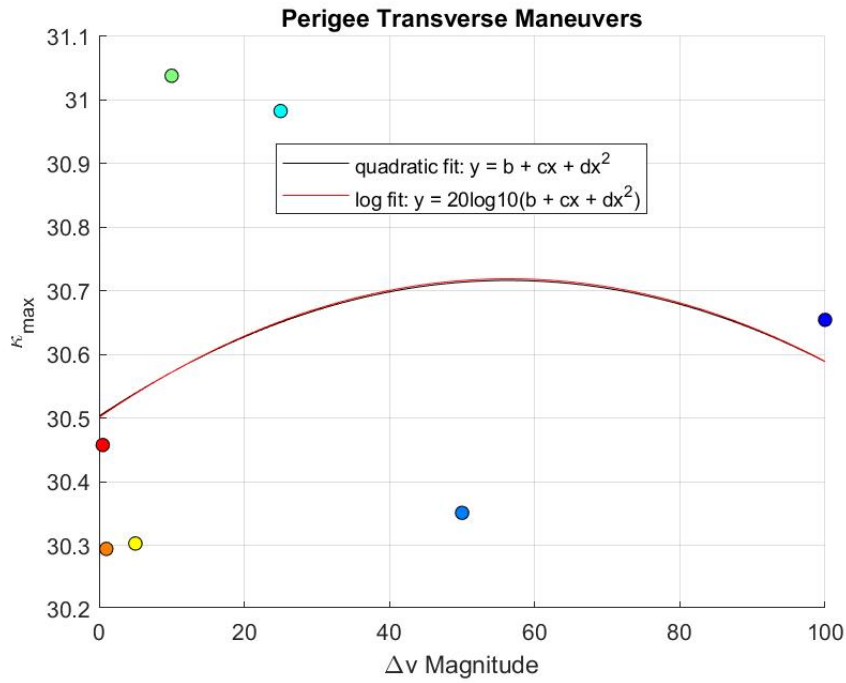


Figure D.6: Variation of K (κ_{\max}) with transverse perigee maneuvers of varying Δv (m/s) for the first Orbital Case with $t_{man} = 10$ seconds.

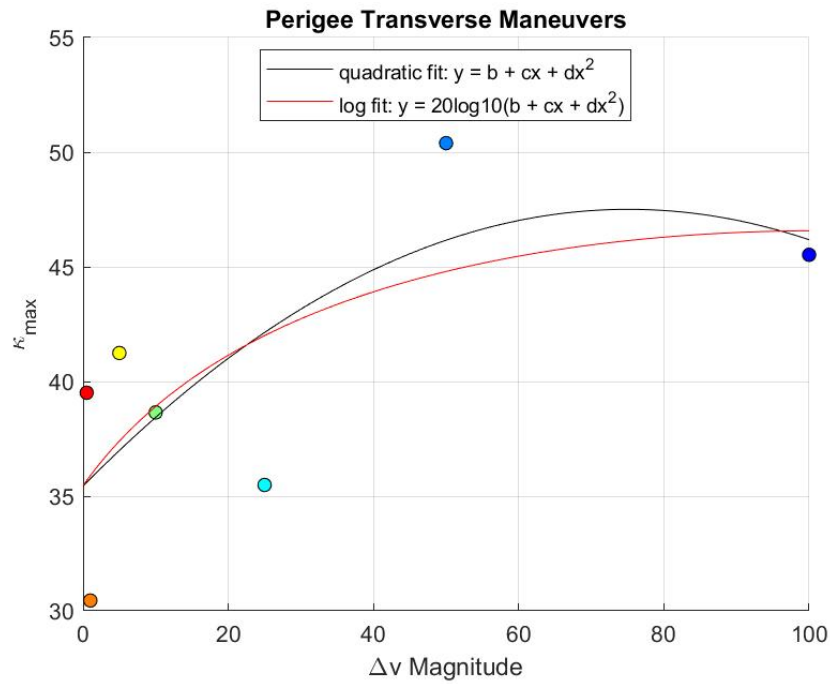


Figure D.7: Variation of K (κ_{\max}) with transverse perigee maneuvers of varying Δv (m/s) for the first Orbital Case with $t_{man} = 1000$ seconds.

APPENDIX E: FURTHER Ψ RESULTS

E.1 Variance in Orbital Location

For the Ψ - Δv results of maneuvers applied at the orbital perigee, the range of the original detection parameter is $40 < \Psi < 220$. At a quarter of the orbit after orbital perigee, the range is $40 < \Psi < 180$, and is much smaller, at $36 < \Psi < 44$ for the maneuvers at a quarter of the orbit after apogee. Thus, for transverse maneuvers, the largest variance in Ψ occurs when maneuvers are applied at apogee, then at perigee, followed by after perigee, leaving the smallest range to maneuvers applied in the transverse direction after apogee. This is consistent with the trend for the K-parameter described in Section 4.2.2, where the largest range of values occurred at the apogee maneuvering location, and the smallest variance occurred with transverse maneuvers applied at the perigee. The same overall observation is deduced that Ψ increases with increasing Δv , and is consistent with Goff et al. [41], with a non-proportional relationship, as expected and stated previously.

The coefficient values for the curve fits of the Ψ - Δv relationship of the perigee maneuvering cases are shown in Table E.1. Similarly to the curve fits for K- Δv , the coefficients for the quadratic and linear curves are generally consistent, where the v_0^2 b -term contains the largest value, and implies that the variance of Ψ has a stronger dependence on v_0^2 . With the square root relationship, the opposite is true, and suggests that Ψ could vary with the square root of the velocity for transverse maneuvers at perigee. Focusing on the quadratic case (per Chapter 4), the d -term remains the smallest, consistently suggesting that Ψ varies less with Δv^2 than v_0^2 .

Table E.3 shows the coefficient values of the fit curves for maneuvering cases at a quarter of the orbit after perigee. Overall, the same general trend is observed, where the Δv -independent term contains the largest quantity throughout, and suggests that Ψ depends greatly on v_0 . This is consistent with the K results of the same case. However, there is more variance with the negatives of the values than previously. Focusing on the quadratic fit, the v_0^2 term is largest in the transverse direction, suggesting the Ψ has a stronger dependence on v_0^2 . The d -term of the quadratic fit in the normal direction is negative and suggests a relationship with the negative of Δv^2 . However, the relationship and implications of negative coefficients is unclear (per Chapter 4). All the d -terms in the quadratic fit for this maneuvering location are small, on the order of 10^{-2} , which is more consistent and less than the apogee case, yet consistent with the K results.

As for the coefficients for the curve fits in the quarter of an orbit after apogee cases, all fits for radial direction maneuvers contain very large values on the orders of 10^4 to 10^6 as presented in Table 4.9. This suggests that Ψ depends greatly on these coefficients for this direction. In the same vein, the smallest values are observed in the coefficients of the curve fits in the normal direction, and suggests Ψ posses a weaker relationship with coefficients in this direction. Throughout the quadratic fit case, the term b suggest greatest dependence on v_0^2 and the term, d , suggests weakest dependence on Δv^2 for all directions, as expected. Relationships with negative associated values are observed in both of the b - and d - terms of the radial direction, as well as in the c -term of the transverse direction. This is different than most previous cases, and is most similar to the apogee maneuver cases.

By the R^2 numbers for perigee maneuvers as shown in Table E.4, the best fit is still the quadratic fit ($y = b + cx + dx^2$) for all directions, which is consistent with prior results and discussion, and follows for the maneuvers applied at the halfway points between orbital perigee and apogee.

Table E.1: Perigee Coefficients for Curve Fit Lines of the Ψ - Δv Relationship

	Linear $y = mx + b$		Square Root $y = c + b\sqrt{x}$		Quadratic $y = b + cx + dx^2$		
	m	b	c	b	b	c	d
Radial	2.8782	25.6178	-15.8893	28.8495	37.8495	1.3284	0.01594
Transverse	1.7403	26.6309	1.9799	17.3369	36.7267	0.4611	0.01320
Normal	2.1167	22.9639	-5.4687	20.7142	38.8352	0.1057	0.02068

Table E.2: Coefficients for Curve Fit Lines of the Ψ - Δv Relationship at a Quarter of the Orbit after Perigee

	Linear $y = mx + b$		Square Root $y = c + b\sqrt{x}$		Quadratic $y = b + cx + dx^2$		
	m	b	c	b	b	c	d
Radial	4.1456	15.6343	-44.5148	41.6403	27.6287	2.6258	0.01563
Transverse	6.9597	-18.8903	-110.6424	67.6931	32.3082	0.4726	0.06670
Normal	1.1899	42.6251	19.08540	13.4578	23.9234	3.5596	-0.02437

Table E.3: Perigee Coefficients for Curve Fit Lines of the Ψ - Δv Relationship at a Quarter of the Orbit after Apogee

	Linear $y = mx + b$		Square Root $y = c + b\sqrt{x}$		Quadratic $y = b + cx + dx^2$		
	m	b	c	b	b	c	d
Radial	2.2890×10^5	5.3091×10^6	-2.4518×10^6	3.3644×10^6	-1.1841×10^7	2.4020×10^6	-2.2344×10^4
Transverse	21.09013	-127.5794	-395.3867	202.6771	84.9014	-5.8324	0.2768
Normal	0.07408	35.9315	34.8720	0.7404	36.1376	0.048797	0.0002685

Table E.4: Perigee R^2 Numbers of the Ψ - Δv Relationship at Perigee

	Linear $y = mx + b$		Square Root $y = c + b\sqrt{x}$		Quadratic $y = b + cx + dx^2$	
	R^2	R^2 adjusted	R^2	R^2 adjusted	R^2	R^2 adjusted
Radial	0.8368	0.8286	0.8261	0.7913	0.9635	0.9453
Transverse	0.9506	0.9481	0.8241	0.7889	0.9913	0.9869
Normal	0.6086	0.5890	0.7756	0.7307	0.9924	0.9885

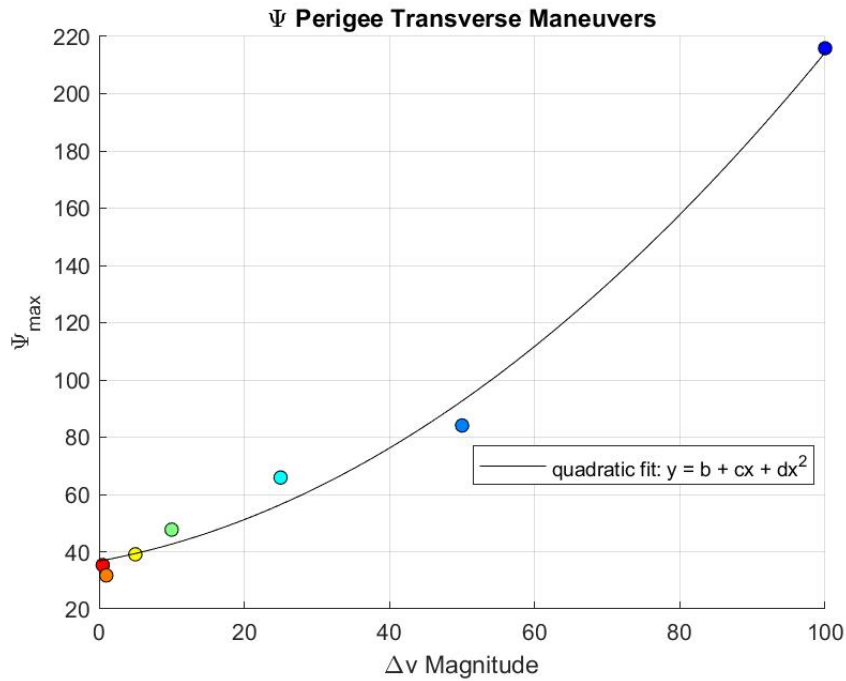


Figure E.1: Trend of Ψ (Ψ_{\max}) with transverse perigee maneuvers of varied Δv (m/s).

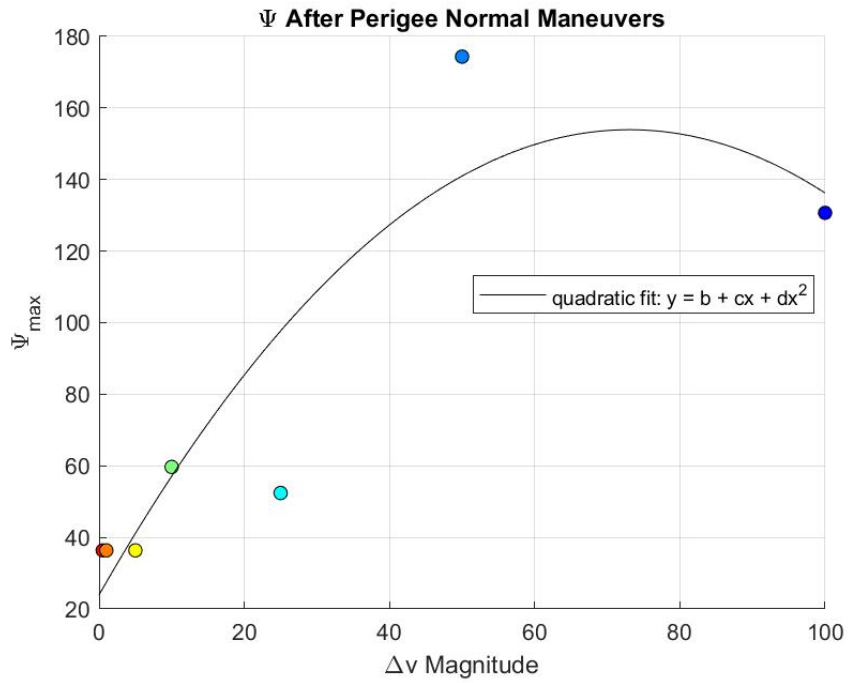


Figure E.2: Trend of Ψ (Ψ_{\max}) with varied transverse maneuver Δv (m/s) applied at a quarter of the orbit after the Orbital Perigee.

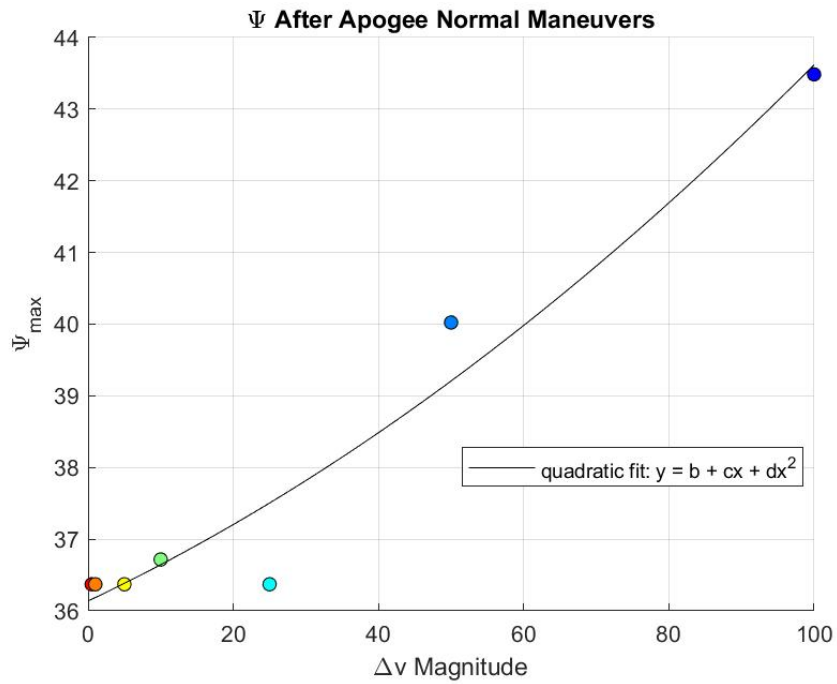


Figure E.3: Trend of Ψ (Ψ_{\max}) with varied Transverse maneuver Δv (m/s) applied at a quarter of the orbit after the Orbital Apogee.

E.2 Variation in Orbital Geometry and Orientation

Figures E.4 and E.5 show the variation in the Ψ detection parameter versus the tested Δv values for this scenario set. For the apogee transverse maneuvers, the resulting range is $0 < \Psi < 35\ 00$, and is smaller, at $0 < \Psi < 800$ for the transverse maneuvers applied at perigee. This is consistent with the results found in the previous sections, where apogee maneuvers generally had a greater variance in transverse maneuvers, for both Ψ and K parameters. Again, the same general trend is deduced, that the magnitude of Ψ increases with increasing Δv in a nonlinear fashion, as expected.

Once again, the same trends are followed as in orbital Case 1, where the v_0^2 terms of the curve fits contain the largest values, suggesting stronger dependence of Ψ on these values, especially for the apogee maneuvers, as presented in Table E.5. With apogee maneuvers, the transverse direction shows the greatest dependence on v_0^2 of the quadratic fit, with the largest variance between coefficients, from 10^2 (term b) to 10^{-2} (term d), and both of these terms are negative. At the same time, the coefficient, C , indicates a relationship with the negative of double v_0 (associated with Δv) for the radial and normal directions in the quadratic fit for apogee maneuvers. With perigee maneuvers, the only negative term relationship is associated with the Δv^2 in the normal direction of the quadratic fit. There is also greater variance in the order of magnitude of the coefficients in the apogee quadratic fits, in comparison to the Case 1 orbital geometry.

By the R^2 numbers in Table E.6, the best fit is consistently the quadratic fit, as per the previous discussion. In this case, the linear correlations in the apogee maneuvers are far away from the accepted range of values for R^2 numbers, and supports that the linear fit is not a best fit for the results.

Table E.5: Coefficients for Curve Fit Lines of the Ψ - Δv Relationship for Maneuvers Applied in the Second Orbital Case

Perigee Maneuvers							
	Linear $y = mx + b$		Square Root $y = c + b\sqrt{x}$		Quadratic $y = b + cx + dx^2$		
	m	b	c	b	b	c	d
Radial	4.1456	15.6343	-44.5148	41.6403	27.6287	2.6258	0.01563
Transverse	6.9597	-18.8903	-110.6424	67.6931	32.3082	0.4726	0.06670
Normal	1.1899	42.6251	19.0854	13.4578	23.9234	3.5596	-0.02437

Apogee Maneuvers							
	Linear $y = mx + b$		Square Root $y = c + b\sqrt{x}$		Quadratic $y = b + cx + dx^2$		
	m	b	c	b	b	c	d
Radial	30.5115	-225.2407	-614.1337	293.5652	48.9411	-4.2289	0.3572
Transverse	32.9212	-103.8998	-607.2513	336.8416	-105.9170	33.1768	-0.002628
Normal	41.9022	-303.4334	-848.9792	405.9118	33.6872	-0.8129	0.4392

Table E.6: R^2 Numbers for Maneuvers Applied in the Second Orbit Case for the Ψ - Δv Relationship

Perigee Maneuvers							
	Linear $y = mx + b$		Square $y = c + b\sqrt{x}$		Quadratic $y = b + cx + dx^2$		
	R^2	R^2 adjusted	R^2	R^2 adjusted	R^2	R^2 adjusted	
Radial	0.8509	0.8434	0.8571	0.8285	0.9839	0.9758	
Transverse	-0.04538	-0.09765	0.7736	0.7284	0.9996	0.9995	
Normal	0.03142	-0.01701	0.6957	0.6348	0.8122	0.7183	

Apogee Maneuvers							
	Linear $y = mx + b$		Square $y = c + b\sqrt{x}$		Quadratic $y = b + cx + dx^2$		
	R^2	R^2 adjusted	R^2	R^2 adjusted	R^2	R^2 adjusted	
Radial	-28.8408	-30.3329	0.7347	0.6817	0.9999	0.9999	
Transverse	-6.2975	-6.6624	0.8946	0.8735	0.9796	0.9694	
Normal	-156.7523	-164.6400	0.7584	0.7101	0.9999	0.9999	

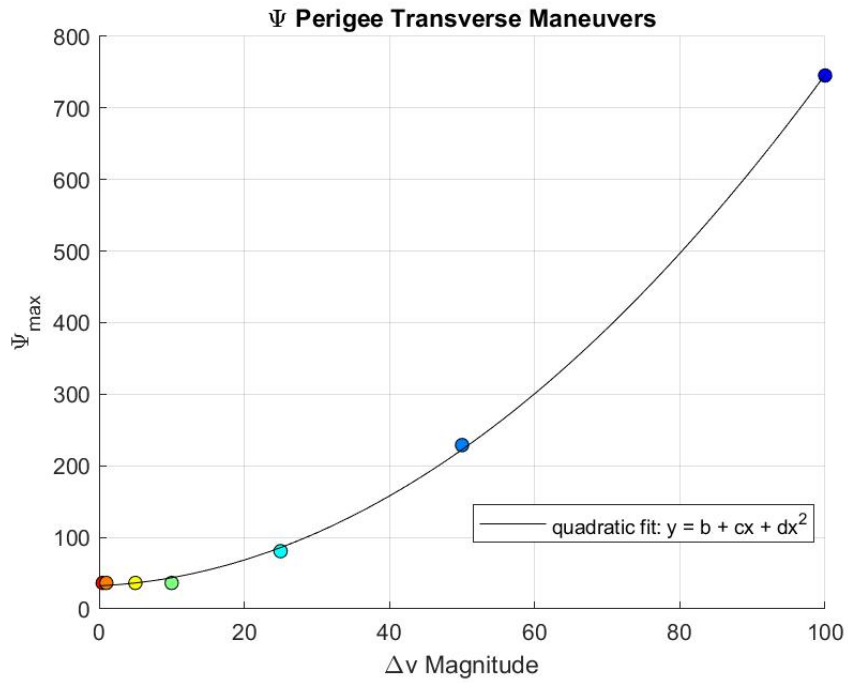


Figure E.4: Trend of Ψ (Ψ_{\max}) with transverse perigee maneuvers of varying Δv (m/s) for the Second Orbital Case.

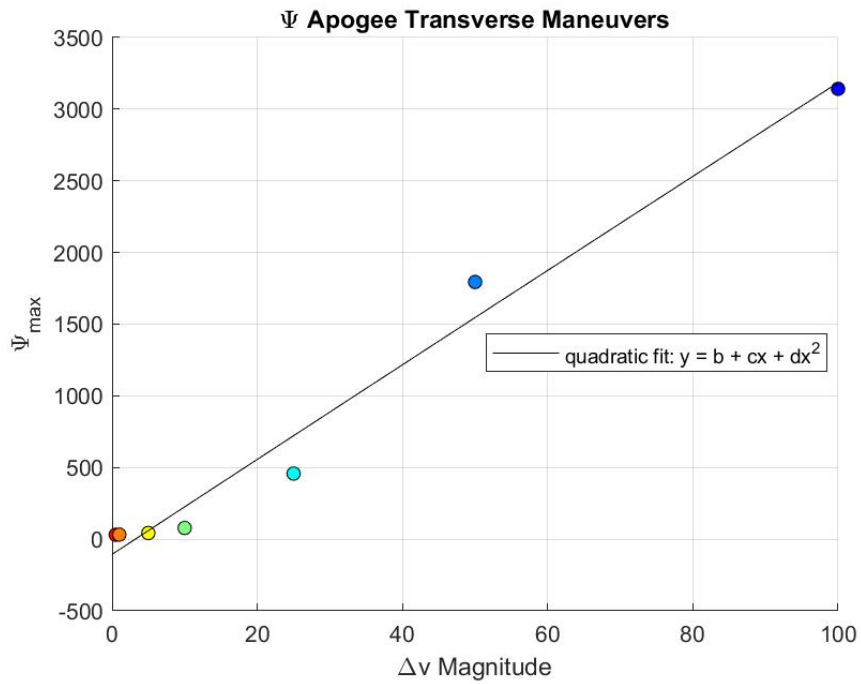


Figure E.5: Trend of Ψ (Ψ_{\max}) with transverse apogee maneuvers of varying Δv (m/s) for the Second Orbital Case.

E.3 Variation of Measurement Noise Covariance

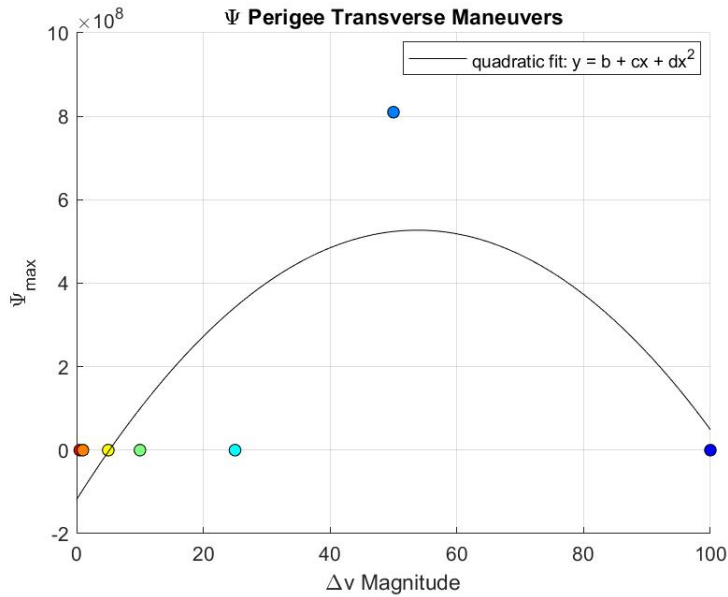


Figure E.6: Variation of Ψ (Ψ_{\max}) with transverse perigee Maneuvers of varying Δv (m/s) for the first Orbital Case with $\mathbf{R} = \mathbf{R}/10$.

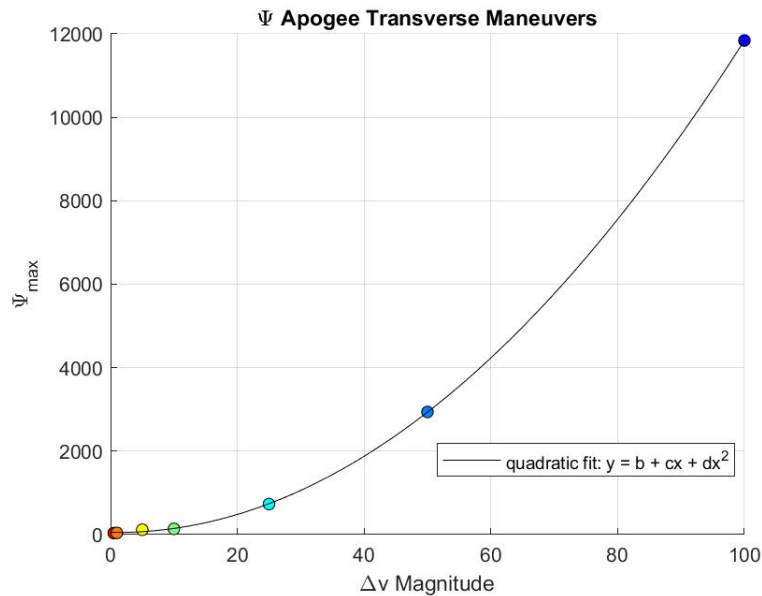


Figure E.7: Variation of Ψ (Ψ_{\max}) with transverse apogee maneuvers of varying Δv (m/s) for the first Orbital Case with $\mathbf{R} = \mathbf{R}/10$.

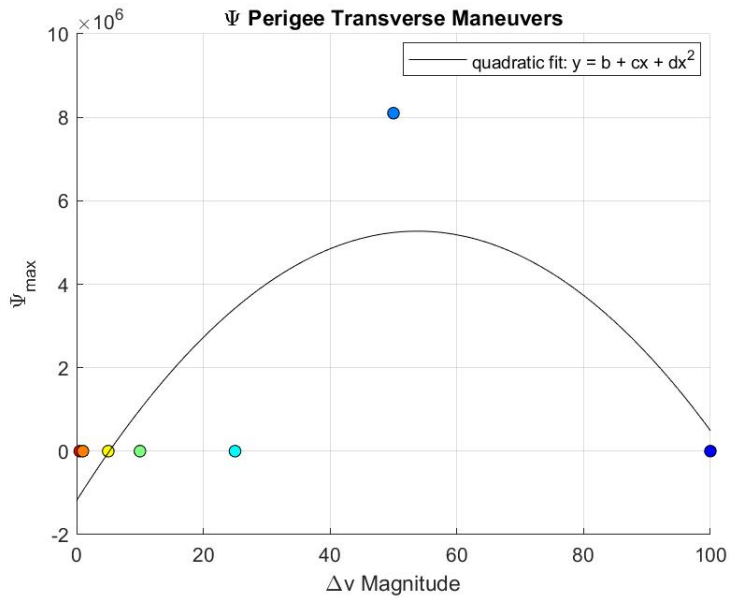


Figure E.8: Variation of Ψ (Ψ_{\max}) with transverse perigee maneuvers of varying Δv (m/s) for the first Orbital Case with $\mathbf{R} = 10\mathbf{R}$.

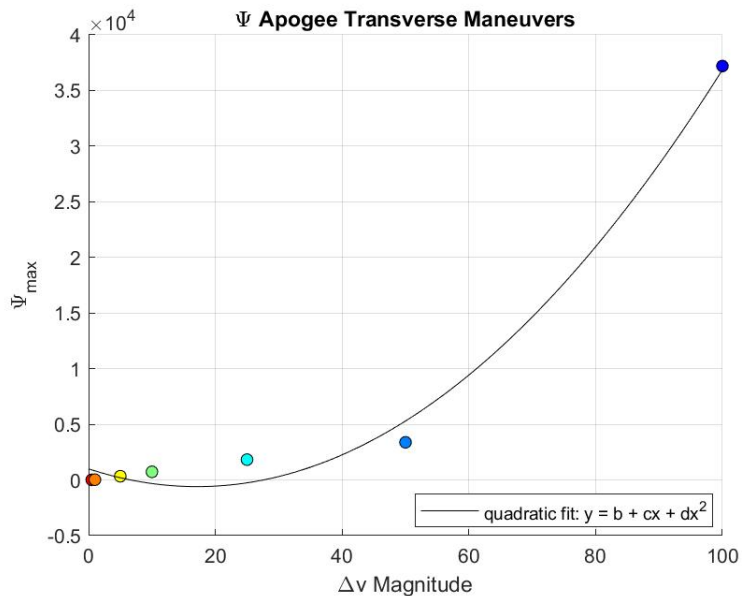


Figure E.9: Variation of Ψ (Ψ_{\max}) with transverse apogee maneuvers of varying Δv (m/s) for the first Orbital Case with $\mathbf{R} = 10\mathbf{R}$.

E.4 Variance in Ψ and η Thresholds

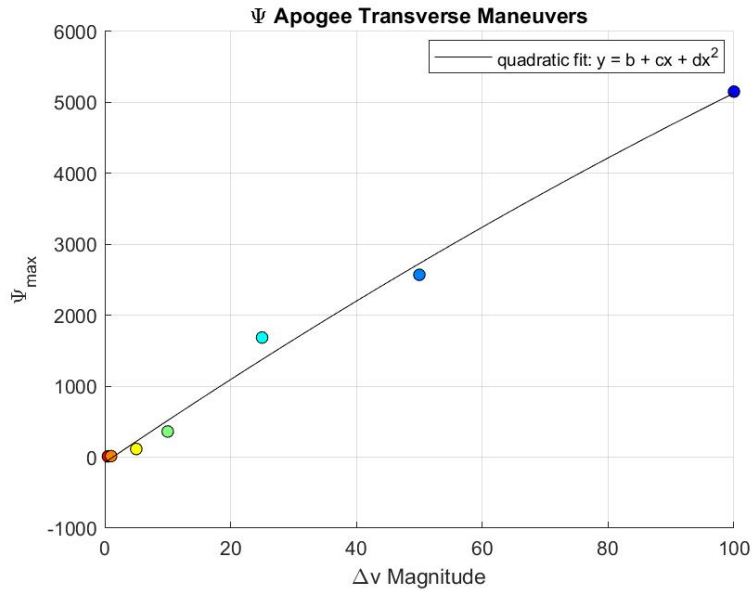


Figure E.10: Variation of Ψ (Ψ_{\max}) with transverse apogee maneuvers of varying Δv (m/s) for the first Orbital Case with $\Psi_{th} = 10$.

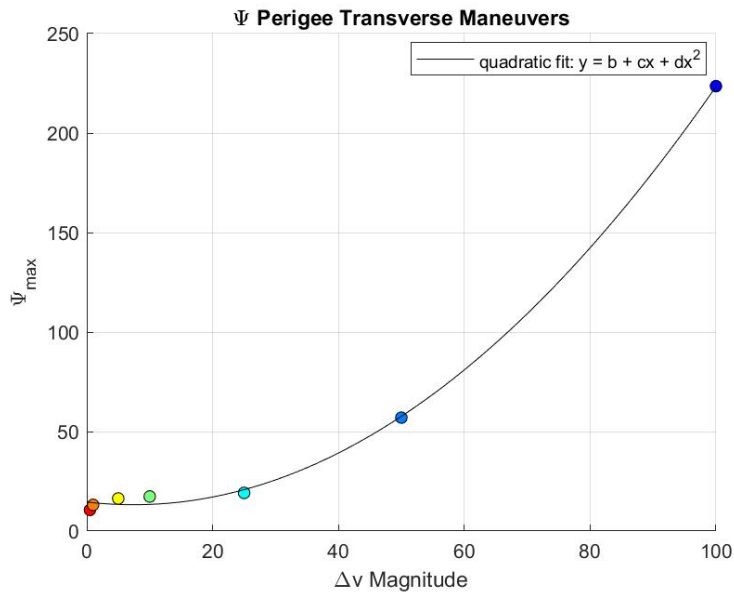


Figure E.11: Variation of Ψ (Ψ_{\max}) with transverse perigee maneuvers of varying Δv (m/s) for the first Orbital Case with $\Psi_{th} = 10$.

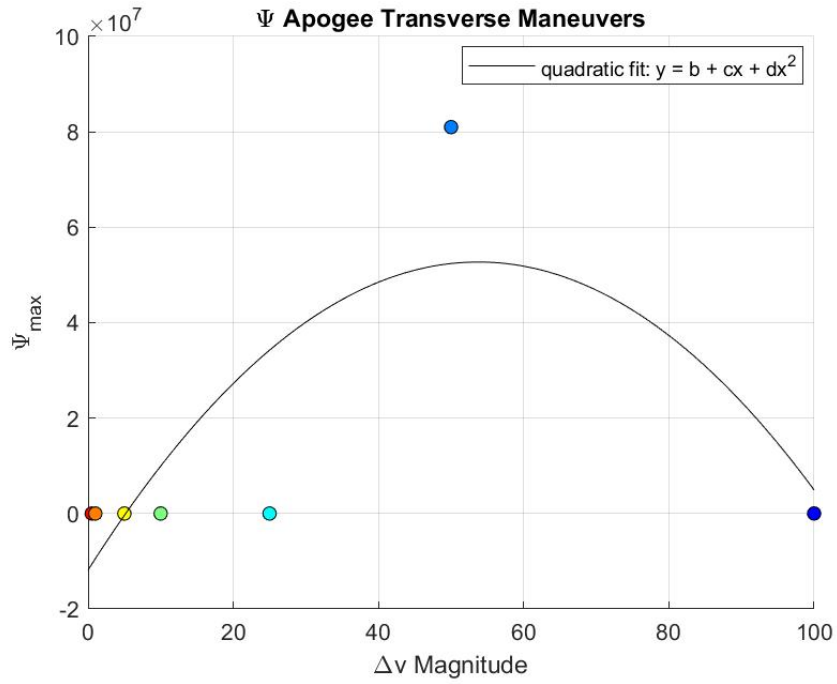


Figure E.12: Variation of Ψ (Ψ_{\max}) with transverse maneuvers of varying Δv (m/s) applied at apogee with $\Psi_{th} = 100$ for the first Orbital Case.

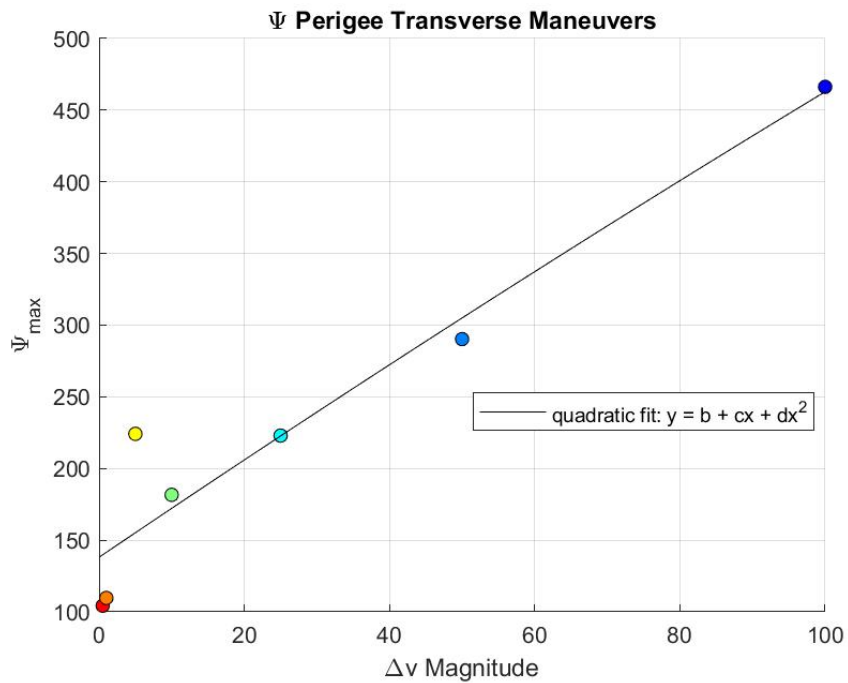


Figure E.13: Variation of Ψ (Ψ_{\max}) with transverse maneuvers of varying Δv (m/s) applied at perigee with $\Psi_{th} = 100$ for the first Orbital Case.

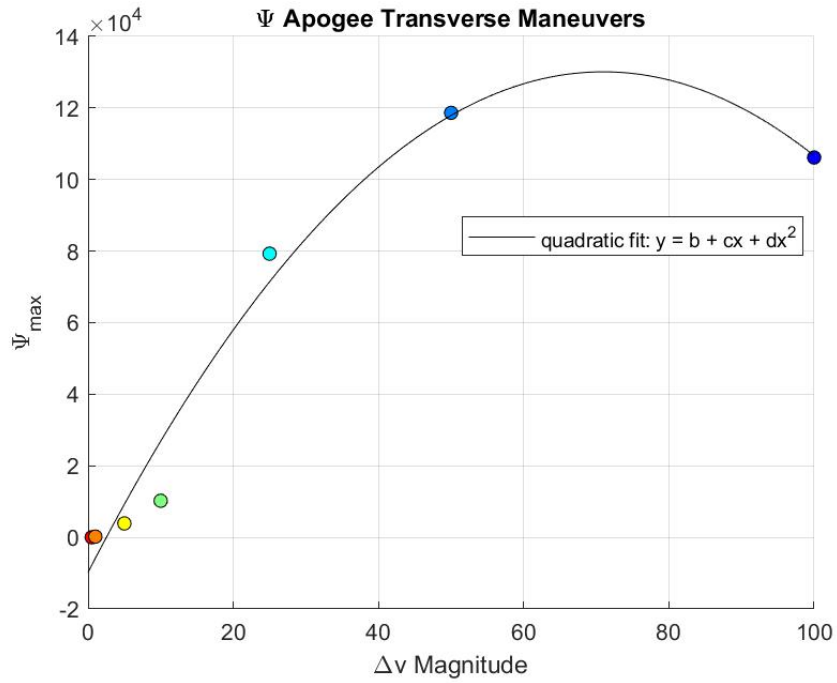


Figure E.14: Variation of Ψ (Ψ_{\max}) with transverse apogee maneuvers of varying Δv (m/s) for the first Orbital Case with $\eta_{th} = 0.1$.

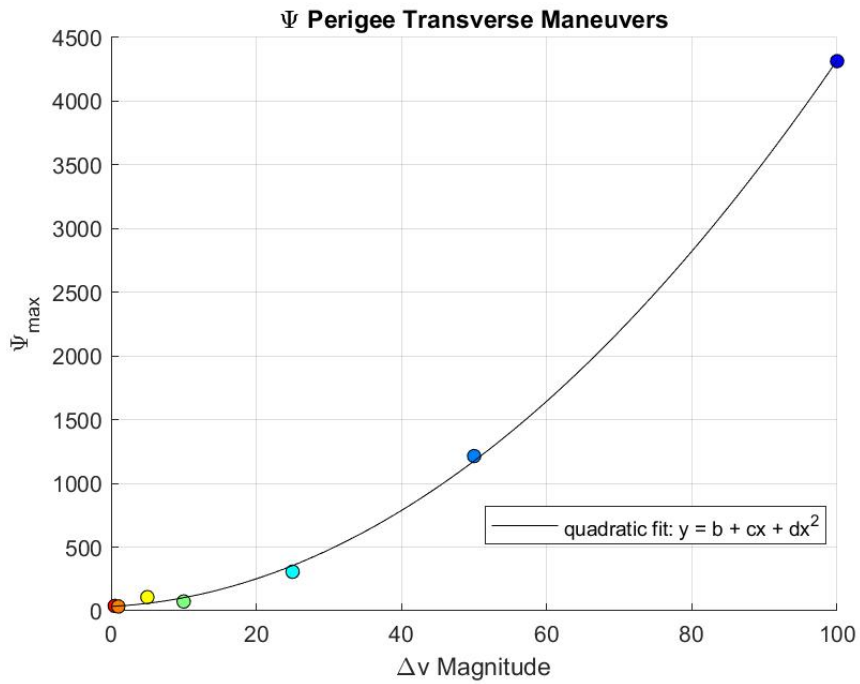


Figure E.15: Variation of Ψ (Ψ_{\max}) with transverse perigee maneuvers of varying Δv (m/s) for the first Orbital Case with $\eta_{th} = 0.1$.

E.5 Variance in Maneuver Duration

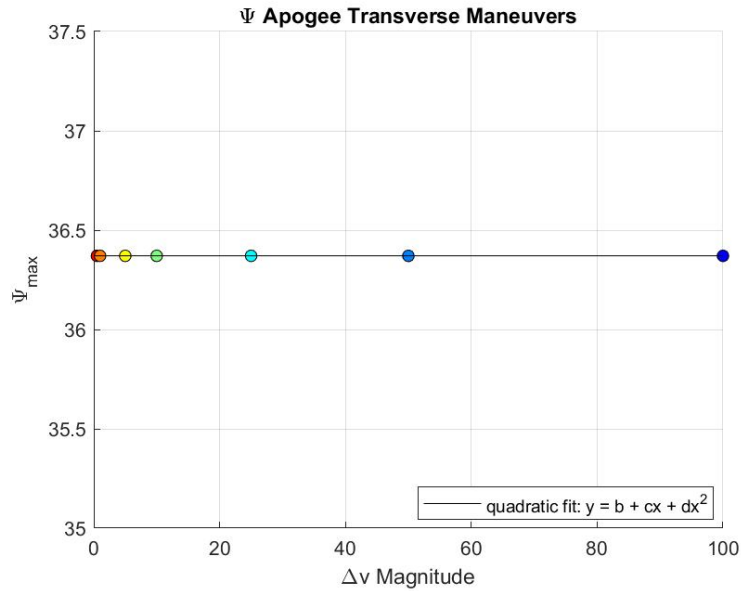


Figure E.16: Variation of Ψ (Ψ_{\max}) with transverse apogee maneuvers of varying Δv (m/s) for the first Orbital Case with $t_{man} = 10$ seconds.

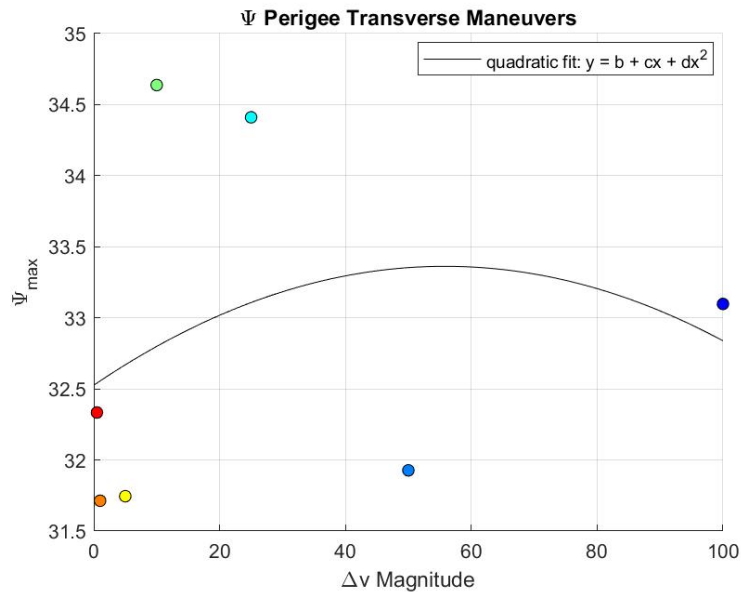


Figure E.17: Variation of Ψ (Ψ_{\max}) with transverse perigee maneuvers of varying Δv (m/s) for the first Orbital Case with $t_{man} = 10$ seconds.

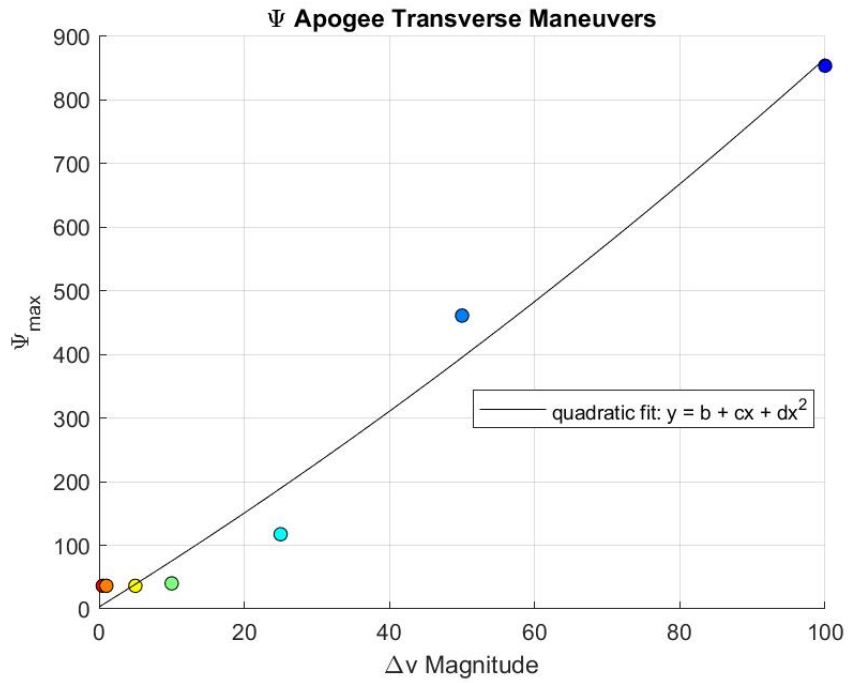


Figure E.18: Variation of Ψ (Ψ_{\max}) with transverse apogee maneuvers of varying Δv (m/s) for the first Orbital Case with $t_{maneuver} = 1000$ seconds.

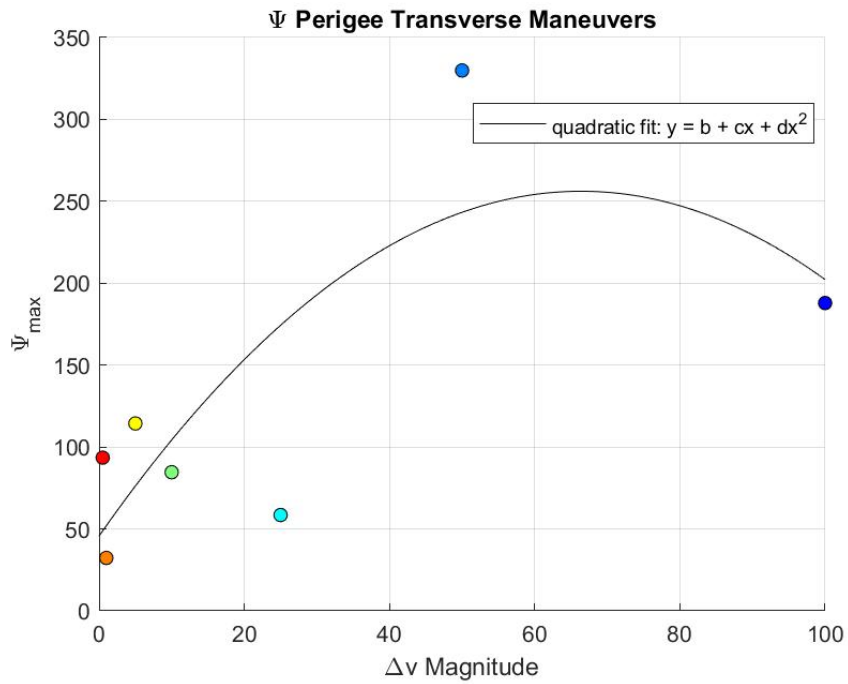


Figure E.19: Variation of Ψ (Ψ_{\max}) with transverse perigee maneuvers of varying Δv (m/s) for the first Orbital Case with $t_{maneuver} = 1000$ seconds.

E.6 Small-Scale Δv 's

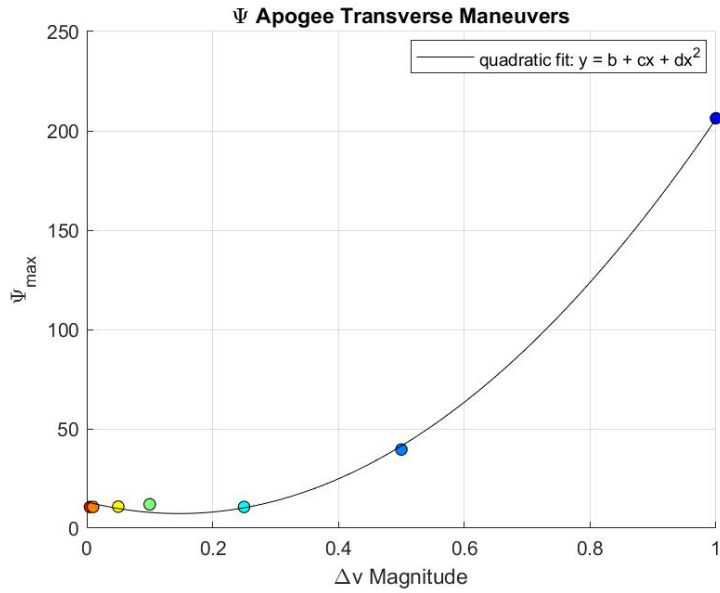


Figure E.20: Variation of Ψ (Ψ_{\max}) with transverse apogee maneuvers of varying Δv in the cm/s scale for the first Orbital Case with $\Psi_{th} = 10$ and $\eta_{th} = 0.1$.

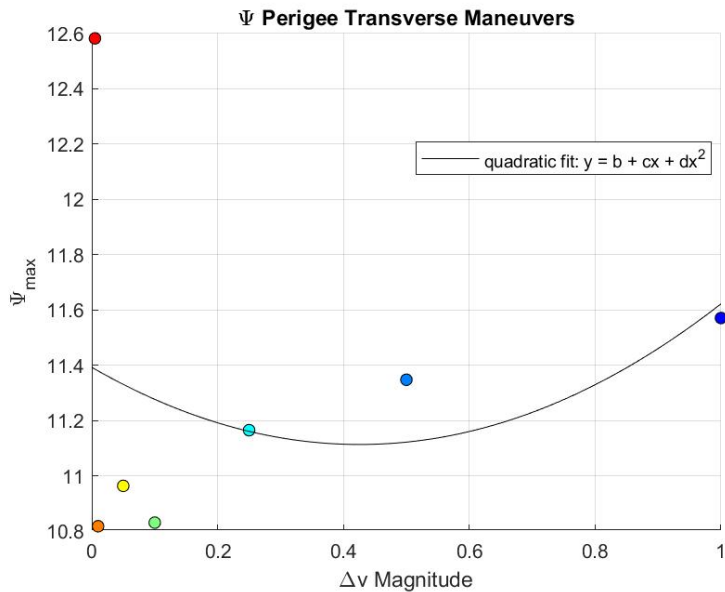


Figure E.21: Variation of Ψ (Ψ_{\max}) with transverse perigee maneuvers of varying Δv in the cm/s scale for the first Orbital Case with $\Psi_{th} = 10$ and $\eta_{th} = 0.1$.

APPENDIX F: MANEUVER DETECTION TIME

The following plots showcase the timing of the detection by K over the simulation time for different Δv 's in both magnitude and direction. The onset and completion of the maneuver are indicated by the vertical dashed lines, and labelled, respectively. These plots are for the same orbital Case 1 as in Sections 4.2.1 and 4.2.2. Apogee Maneuvers are generally accurate with very close times to the maneuvering onset, within the maneuvering duration, other than few select cases. However, at perigee, detection often occurs much earlier, with an average of almost 400 seconds earlier. The reason is unclear, though this fact may explain some of the variances or inconsistencies observed through analyses of the results in Chapter 4.

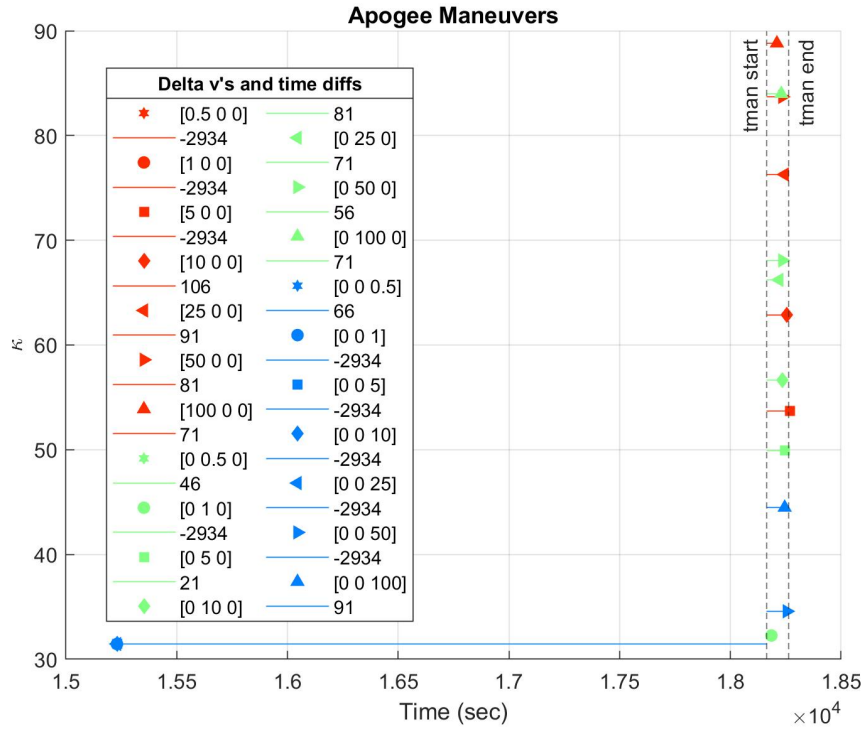


Figure F.1: Detection timing of $K (\kappa)$ for orbital Case 1 apogee maneuver Δv (m/s).

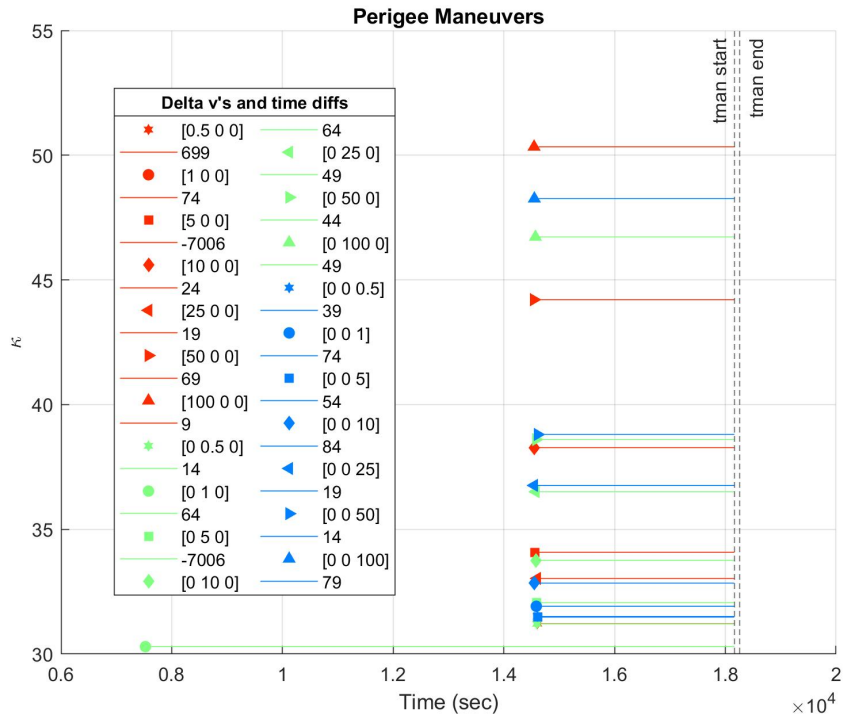


Figure F.2: Detection timing of $K (\kappa)$ for orbital Case 1 perigee maneuver Δv (m/s).

REFERENCES

- [1] John A Kennewell and Ba-Ngu Vo. An overview of space situational awareness. In *Proceedings of the 16th International Conference on Information Fusion*, pages 1029–1036. IEEE, 2013.
- [2] Union of Concerned Scientists (UCS), Dec 2005 [Updated: Apr. 1, 2020]. <https://www.ucsusa.org/resources/satellite-database#.WblhVtiQyUl>.
- [3] The Industrial College of the Armed Forces. Space industry. Technical report, National Defense University, Fort McNair, 2011.
- [4] Christopher J. Castelli. Closer commercial ties urged: DOD sees space as increasingly congested, contested, competitive. *Inside the Air Force*, 21(11):10–12, 2010.
- [5] Roger G. Harrison. Unpacking the three C’s: Congested, competitive, and contested space. *Astropolitics*, 11(3):123–131, 2013.
- [6] NASA Orbital Debris Program Office. *Orbital Debris Quarterly News*, 24(3), Aug 2020. <https://orbitaldebris.jsc.nasa.gov/quarterly-news/pdfs/odqnv24i3.pdf>.
- [7] Canadian Space Agency. Satellites in our everyday lives, Jan 2020. <https://www.asc-csa.gc.ca/eng/satellites/everyday-lives/default.asp>.
- [8] Canadian Space Agency. 10 ways that satellites helped you today, Feb 2018. <https://www.asc-csa.gc.ca/eng/satellites/everyday-lives/10-ways-that-satellites-helped.asp>.
- [9] Ed Kyle. Space Launch Report Log by Decade, Dec 2019 [Updated: Aug. 18 2020]. <https://www.spacelaunchreport.com/logdec.html#1990s>.
- [10] NASA Orbital Debris Program Office. *Orbital Debris Quarterly News*, 24(1), Feb 2020. <https://orbitaldebris.jsc.nasa.gov/quarterly-news/pdfs/odqnv24i1.pdf>.
- [11] ESA Space Debris Office. ESA’s Annual Space Environment Report. Technical report, July 2019. https://www.sdo.esoc.esa.int/environment_report/Space_Environment_Report_latest.pdf.

- [12] Tate Ryan-Mosley, Erin Winick, and Konstantin Kakaesarchive. The number of satellites orbiting Earth could quintuple in the next decade, April 2020. <https://www.technologyreview.com/2019/06/26/755/satellite-constellations-orbiting-earth-quintuple/>.
- [13] United Nations (UN). Technical Report on Space Debris. Technical report, United Nations Publication, New York, 1999.
- [14] European Space Operations Centre (ESOC). ESA's Annual Space Environment Report. Technical report, Darmstadt, Germany, 2018.
- [15] D. J. Kessler and B. Cour-Palais. Collision frequency of artificial satellites: The creation of a debris belt. *Journal of Geophysics Research*, 83:2637–2646, 1978.
- [16] Donald J. Kessler. Collisional cascading: The limits of population growth in low earth orbit. *Advances in Space Research*, 11(12):63 – 66, 1991.
- [17] Brandon A. Jones, Daniel S. Bryant, Ba-Tuong Vo, and Ba-Ngu Vo. Challenges of multi-target tracking for space situational awareness. In *18th International Conference on Information Fusion*, 2015.
- [18] European Space Agency (ESA). Space debris by the numbers, [Online: 2020; Accessed: January 2018]. Report by European Space Operations Centre (ESOC), https://www.esa.int/Our_Activities/Operations/Space_Debris/Space_debris_by_the_numbers.
- [19] Edward T Ackerman. Us military, commercial, and international cooperation for improved space situational awareness. Technical report, Air War College Air University Maxwell AFB United States, 2010.
- [20] Mark A Baird. Maintaining space situational awareness and taking it to the next level. Technical report, Air and Space Power Journal, Maxwell Air Force Base (AFB), AL, 2013.
- [21] Tom Kelecy and Moriba Jah. Detection and orbit determination of a satellite executing low thrust maneuvers. *Acta Astronautica*, 66(5-6):798–809, 2010.
- [22] National Research Council et al. *Continuing Kepler's Quest: Assessing Air Force Space Command's Astrodynamics Standards*. National Academies Press, 2012.
- [23] N. Bobrinsky and L. D. Monte. The Space Situational Awareness Program of the European Space Agency. *Cosmic Research*, 48(5):392–398, January 2010.

- [24] P. Maskell and L. Oram. Sapphire: Canada's answer to space-based surveillance of orbital objects. In *Advanced Maui Optical and Space Surveillance Conference, Maui, Hawaii*. 2008.
- [25] B. Weeden. Space Situational Awareness Fact Sheet; Promoting Cooperative Solutions for Space sustainability, [Online: 2017; Accessed: January 2018]. https://swfound.org/media/205874/swf_ssa_fact_sheet.pdf.
- [26] V Abbasi, M Doyon, R Babiker, and D Golla. Advanced space situational awareness through automated conjunction risk analysis system (crams).
- [27] National Aeronautics and Space Administration. U. S. National Space Policy. Technical report, 2006.
- [28] Japan Aerospace Exploration Agency (JAXA). Space Situational Awareness (SSA) system, [Online: 2003; Accessed: January 2018]. <http://global.jaxa.jp/projects/ssa/index.html>.
- [29] European Space Agency (ESA). About SSA, [Online: January 2018]. https://m.esa.int/Our_Activities/Operations/Space_Situational_Awareness/About_SSA.
- [30] Marcus J Holzinger, K Kim Luu, Chris Sabol, and Keric Hill. Uncorrelated-track classification, characterization, and prioritization using admissible regions and bayesian inference. *Journal of Guidance, Control, and Dynamics*, 39(11):2469–2484, 2016.
- [31] J. Stauch, T. Bessell, M. Rutten, J. Baldwin, M. Jah, and K. Hill. Joint probabilistic data association and smoothing applied to multiple space object tracking. *Journal of Guidance, Control, and Dynamics*, 41(1):19–33, 2018.
- [32] K. T. Alfriend. Covariance based track association. Technical report, Texas AM University, College Station, 2016.
- [33] C. Sabol, K. Hill, K. Alfriend, and T. Sukut. Nonlinear effects in the correlation of tracks and covariance propagation. *Acta Astronautica*, 84:69–80, 2013.
- [34] Prasanta Chandra Mahalanobis. On the generalized distance in statistics. National Institute of Science of India, 1936.
- [35] D. J. Scheeres, K. T. Alfriend, and C. Freuh. Modeling observability and change detection in space situational awareness final. Technical report, Defense Technical Information Center, The Regents of the University of Colorado, 2018.

- [36] Hyun Chul Ko. *Representation of Unknown and Unmodeled Space Events for Satellites: Characteristics and Applications*. PhD thesis, University of Colorado at Boulder, 2015.
- [37] Jennifer S Hudson and Daniel J Scheeres. Reduction of low-thrust continuous controls for trajectory dynamics. *Journal of guidance, control, and dynamics*, 32(3):780–787, 2009.
- [38] Jennifer S Hudson and Daniel J Scheeres. Orbital targeting using reduced eccentric anomaly low-thrust coefficients. *Journal of guidance, control, and dynamics*, 34(3):820–831, 2011.
- [39] B. Jia, E. Blasch, K. D. Pham, D. Shen, Z. Wang, X. Tian, and G. Chen. Space Object Tracking and Maneuver Detection via Interacting Multiple Model Cubature Kalman Filters. pages 1–8. IEEE Aerospace Conference, 2015.
- [40] B. Jia, K. D. Pham, E. Blasch, D. Shen, Z. Wang, and G. Chen. Cooperative space object tracking using consensus-based filters. pages 1–8. 17th International Conference on Information Fusion (FUSION), July 2014.
- [41] Gary M Goff, Jonathan T Black, and Joseph A Beck. Tracking maneuvering spacecraft with filter-through approaches using interacting multiple models. *Acta Astronautica*, 114:152–163, 2015.
- [42] Sangjin Lee and Inseok Hwang. Interacting multiple model estimation for spacecraft maneuver detection and characterization. In *AIAA Guidance, Navigation, and Control Conference*, page 1333, 2015.
- [43] M. Holzinger and D. Scheeres. Object correlation and maneuver detection using optimal control performance metrics. In *Advanced Maui Optical and Space Surveillance Technologies Conference*, Maui, 2010.
- [44] Daniel P Lubey and Daniel J Scheeres. Towards real-time maneuver detection: Automatic state and dynamics estimation with the adaptive optimal control based estimator. *amos*, page 16, 2015.
- [45] Marcus J Holzinger, Daniel J Scheeres, and Kyle T Alfriend. Object correlation, maneuver detection, and characterization using control distance metrics. *Journal of Guidance, Control, and Dynamics*, 35(4):1312–1325, 2012.
- [46] Stijn Lemmens and Holger Krag. Two-line-elements-based maneuver detection methods for satellites in low earth orbit. *Journal of Guidance, Control, and Dynamics*, 37(3):860–868, 2014.

- [47] Russell P Patera. Space event detection method. *Journal of Spacecraft and Rockets*, 45(3):554–559, 2008.
- [48] Noelia Sánchez-Ortiz and Holger Krag. Required accuracy for a reliable space objects collision avoidance assessment within the european space situational awareness system. In *Proceedings of the European Space Surveillance Conference*, 2011.
- [49] K. J. DeMars, I. I. Hussein, C. Frueh, M. K. Jah, and R. S. Erwin. Multiple-object space surveillance tracking using finite-set statistics. *Journal of Guidance, Control, and Dynamics*, 38(9):1741–1756, 2015.
- [50] E. Delande, C. Frueh, J. Franco, J. Houssineau, and D. Clark. Novel multi-object filtering approach for space situational awareness. *Journal of Guidance, Control, and Dynamics*, 41(1):59–73, 2018.
- [51] N. Singh, J. T. Horwood, J. M. Aristoff, A. B. Poore, C. Shea, and M. K. Jah. Multiple hypothesis tracking (MHT) for space surveillance: Results and simulation studies. In *Advanced Maui Optical and Space Surveillance Technologies Conferences*, 2013.
- [52] S. Olivier, K. Cook, B. Fasenfest, D. Jefferson, M. Jiang, J. Leek, J. Levatin, S. Nikolaev, A. Pertica, D. Phillion, K. Springer, and W. D. Vries. High-performance computer modeling of the Cosmos-Iridium collision. Technical report, Lawrence Livermore National Lab, 2009.
- [53] David A. Vallado. *Fundamentals of Astrodynamics and Applications*. Space Technology Library, USA, 2007.
- [54] Howard D Curtis. *Orbital mechanics for engineering students*. Butterworth-Heinemann, 2014. 3rd ed.
- [55] Robert L Williams, Douglas A Lawrence, et al. *Linear State-Space Control Systems*. John Wiley & Sons, 2007.
- [56] Hyun Chul Ko. Representation of unknown and unmodeled space events for satellites: Characteristics and applications. 2015.
- [57] Mohinder S Grewal and Angus P Andrews. *Kalman filtering: Theory and Practice with MATLAB*. John Wiley & Sons, 2014.
- [58] Orlando X Diaz. Analysis and comparison of extended and unscented kalman filtering methods for spacecraft attitude determination. Technical report, Naval Postgraduate School, Monterey, CA, 2010.

- [59] S. J. Julier and J. K. Uhlmann. Unscented filtering and nonlinear estimation. *Proceedings of the IEEE*, 92(3):401–422, 2004.
- [60] I. Arasaratnam and S. Haykin. Cubature kalman filters. *IEEE Transactions on Automatic Control*, 54(6):1254–1269, 2009.
- [61] Steve Ulrich. Aero 3240 orbital mechanics. Course Notes, September 2015. Carleton University.
- [62] Wiley J Larson and James Richard Wertz. *Space mission analysis and design*. 1992.